Slow and Stored Light in Atomic Vapor Cells

A thesis presented
by

Mason Joseph Klein

to
The Department of Physics
in partial fulfillment of the requirements
for the degree of
Doctor of Philosophy
in the subject of

Physics

Harvard University
Cambridge, Massachusetts
May 2009

Thesis advisor

Ronald L. Walsworth

Author

Mason Joseph Klein

Slow and Stored Light in Atomic Vapor Cells

Abstract

This thesis describes experimental investigations of electromagnetically-induced transparency (EIT), slow, and stored light in warm atomic Rb vapor, employing a variety of vapor cells with the aim of both better understanding and optimizing slow and stored light, and looking ahead towards their potential applications in optical communication and quantum information.

We first develop a practical tool for the study of EIT-based slow light, showing how slow light pulse delays can be accurately predicted from static transmission spectra, not only theoretically for ideal cases, but for real experimental systems, and using only directly measured linewidth and off-resonant transmission.

Next we explore stored light in buffer gas cells at high optical depths, developing techniques to mitigate detrimental high-optical depth effects such as radiation trapping. We also compare the effects of different buffer gases on EIT lineshapes.

We then turn to the unique behavior of EIT and slow light in paraffin-coated vapor cells. These cells allow long coherence lifetimes, supporting large delays for slow light pulses. Stored light in coated cells with long storage times is demonstrated, as is a technique that allows storing of high-bandwidth pulses over long time scales. This includes the first reported measurements of hyperfine EIT and slow light in coated vapor cells, utilizing a specialized cell geometry.

Finally we present a novel application based on our understanding of coated cell physics: the "slow light beamsplitter," where coherence is written into the atoms via EIT,

and can be read out at another location, utilizing the volume-filling coherence unique to EIT in coated cells. The splitting of a pulse into two channels is shown to be phase coherent.

Overall, this set of experiments demonstrates both the potential and limitations of alkali vapor cells for slow and stored light applications, by studying relevant decoherence mechanisms along with ways to reduce their effects, and by introducing novel tools and techniques for use in classical communications and quantum optics applications.

Contents

List of Figures

Papers and Publications

1. *EIT in paraffin-coated vapor cells*
   M. Klein, M. Hohensee, D. F. Phillips, and R. L. Walsworth, submitted to Phys. Rev. A (2009).

2. *Slow light in narrow paraffin-coated vapor cells*
   M. Klein, M. Hohensee, A. Nemiroski, Y. Xiao, D. F. Phillips, and R. L. Walsworth, submitted to Appl. Phys. Lett. (2009).

3. *Slow-light dynamics from electromagnetically-induced-transparency spectra*
   M. Klein, M. Hohensee, Y. Xiao, R. Kalra, D. F. Phillips, and R. L. Walsworth, accepted in Phys. Rev. A (2009).

4. *Slow light and EIT under realistic (imperfect) conditions*
   M. Klein, Y. Xiao, M. Hohensee, D. F. Phillips, and R. L. Walsworth, Proc. SPIE (2009).

5. *Slow light beamsplitter*
   Y. Xiao, M. Klein, M. Hohensee, L. Jiang, D. F. Phillips, M. D. Lukin, and R. L. Walsworth, Phys. Rev. Lett. **101**, 043601 (2008).

6. *Optimizing slow and stored light for multidisciplinary applications*
   M. Klein, Y. Xiao, A. V. Gorshkov, M. Hohensee, C. D. Leung, M. R. Browning, D. F. Phillips, I. Novikova, and R. L. Walsworth, Proc. SPIE **6904**, 69040C (2008).

7. *Optimization of slow and stored light in atomic vapor*
   I. Novikova, A. V. Gorshkov, D. F. Phillips, Y. Xiao, M. Klein, and R. L. Walsworth, Proc. SPIE **6482**, 64820M (2007).

8. *Slow light in paraffin-coated Rb vapour cells*
   M. Klein, I. Novikova, D. F. Phillips, and R. L. Walsworth, Journ. Mod. Optics **53**, 2583 (2006).

9. *Interstitial gas and density-segregation of vertically-vibrated granular media*
   M. Klein, L. L. Tsai, M. S. Rosen, T. Pavlin, D. Candela, and R. L. Walsworth, Phys. Rev. E **74**, 010301(R) (2006).

10. *Optimizing stored light efficiency in vapor cells*
    I. Novikova, M. Klein, D. F. Phillips, and R. L. Walsworth, Proc. SPIE **5735**, 87 (2005).

Acknowledgments

This work is very much a collaborative effort, and I am indebted to many people for their assistance and encouragement throughout my time in graduate school. First I would like to thank my advisor, Ron Walsworth, for his support and guidance in my work, his insight into physical problems, and his enthusiasm for scientific work. I'm grateful to have inhabited his lab, and will miss it.

I have attempted to learn from and emulate several scientists senior to me. I would like to thank David Phillips for his time, patience, and work on all my projects, and for teaching me how to do science better and communicate it effectively; Irina Novikova for her assistance with my earlier slow light work, and showing me my way around an optics table; and Matt Rosen for literally making me get my hands dirty the first day I showed up, and his valuable technical advice throughout my time in the lab.

I worked directly with a number of other graduate students and postdocs on a variety of projects, and would like to thank them as well. My theoretical counterpart Michael Hohensee explained things to me on a continual basis, and was full of ideas to try out experimentally, some of which I actually did try, and most of those turned into results in this thesis. Yanhong Xiao and I worked together on several slow light projects; I thought we complemented each other well, and it has been a pleasure working with her. Leo Tsai and I completed the vibrated sand experiment using only three lab notebooks. Leo was great to work with, and a good friend inside and outside the lab. Alex Glenday was a constantly helpful presence in the lab, and always generous with his time and knowledge. Rita Kalra joined the group near the end of my time here, and I have enjoyed working with her as well. I also collaborated with students outside the Walsworth group, especially Alex Nemiroski on the miniature coated cell construction, and Alexey Gorshkov on stored light efficiency calculations.

Several undergraduates also contributed to my slow light work, in particular Cleo

Leung and Mark Browning, who worked on radiation trapping measurements, and also Ong Pholchai, Elizabeth Goldschmidt, and Chris Smallwood.

I would also like to thank Kevin Bennett at the CfA machine shop for sharing his advice, time, and tools on numerous occasions when I machined components for my experiments.

I would never have gotten here without those who have fostered my interest in science as I grew up: from my dad who built a remote-controlled car with me (even if my main job was to paint it) and liked to talk about how things work; to my high school science teacher Clarence Snapper, who knew when and when not (usually not) to answer my questions; to my college mentor Matt Walhout, who was both a strong role model and introduced me to the excitement of physics research.

My friends in graduate school all have helped make this whole shared experience better, and I am very grateful for all of you. I also want to thank my family for their support, especially my parents and sisters. Mom, Dad, Madeline, and Tessa: you have been nothing but loving and encouraging to me throughout my life, and I love you all very much.

And finally, of course, Rebecca. What can I say? You make everything matter so much more, and I wouldn't have wanted to do it without you.

Chapter 1

Introduction

1.1 Motivation

The slowing and storing of optical signals and information is an exciting area of research and of great interest. Photonics and optical communications benefit from slow light for use in controllable delay lines [1]. The storing and manipulating of quantum states forms the basis of quantum information applications such as quantum repeaters and long distance quantum communication [2, 3]. Photons are robust carriers of information, and systems using light and atoms have the potential to realize stable and efficient transport and manipulation. Indeed, many proof-of-principle experimental demonstrations have been completed, showing the reversible storage of single-photon states [4, 5, 6], single photon EIT [7], and components of quantum repeaters [8, 9, 10].

The physical foundation of many experiments that slow and store optical signals is electromagnetically-induced transparency (EIT) [11, 12, 13, 14, 3, 15]. EIT is a two-optical field effect where a "control" field renders an otherwise opaque medium transparent to a second "signal" field on atomic resonance. This allows the signal field to propagate with greatly reduced absorption but while experiencing other strong resonant effects.

Steep resonant dispersion that is a consequence of EIT allows signal field pulses to propagate with reduced group velocity: slow light [14, 1]. This was realized experimentally in both cold [16] and warm [17, 18] atomic systems. It can be shown that the delay of a slow light pulse scales with the applied control field intensity, and thus bringing the control field to zero while the pulse propagates in the medium brings the group velocity to zero and "stops" the light pulse [19, 20]. Photons are not literally stopped, but the phase information and shape of the pulse is encoded into the atomic medium; since it does this by coherently altering the quantum states of the atoms (into the so-called "dark state"), the process is reversible and the pulse can be restarted when the control field turns back on. This was also realized experimentally [21, 22], and it was shown that the stored light process preserves the phase coherence of the input pulse [23]. Recent work has seen storage times of up to 1 second using EIT in a solid state system [24].

In real physical systems, the storage and retrieval process is not 100% efficient, which is a continuing challenge in photonics and quantum optics applications of stored light. The EIT-based slow and stored light experiments in this thesis were performed in warm rubidium vapor cells. Vapor cells have been used in many types of experiments, including atomic clocks [25, 26], and magnetometers [27, 28]. The merits of vapor cells as candidates for high efficiency, long-time-scale slow and stored light have been debated [29, 30], and it is uncertain whether coherence loss mechanisms in such cells will prevent their optimal use in future applications. Much of the present work involves examining this question.

Alkali vapor cells are in some ways ideal systems for exploring slow and stored light potential and limitations. Alkali atoms, with only the state of a single electron to be concerned with, closely approximate the ideal three-level EIT model, and can thus be modeled theoretically. Predictions are readily testable due to the compactness and simplicity of vapor cell apparatuses, which operate near room temperature and require relatively few

optical components. Vapor cells can also be fabricated in the laboratory, and their properties (atom-confining buffer gas and pressure, cell geometry, cell temperature, etc.) can be adjusted to investigate the dependence of slow and stored light on many parameters.

In many warm vapor cell systems, the lifetime of atomic spin states (which carry the photonic information during light storage) is limited by movement of atoms out of the presence of the input light fields and subsequent loss of coherence due to cell wall collisions, which thermalize internal atomic states, destroying spin coherence. One approach is to employ cells with anti-relaxation coating on their interior surfaces. Coated cells have been used for decades [31, 32, 33], and can support long coherence lifetimes, as atoms colliding with the coating maintain their quantum states for many wall collisions; lifetimes of up to 1 second have been observed in such cells [34, 35]. For slow and stored light applications, coated cells hold the promise of long pulse delays [18] and storage times.

The remainder of this chapter provides an introduction to EIT, slow light, and stored light. Then we discuss departures from ideal three-level EIT behavior, and list various decoherence mechanisms present in vapor cell systems.

1.2 Basics of EIT

In this section we review electromagnetically-induced transparency (EIT) in a three-level Λ-configuration. We draw from more comprehensive treatments in [36, 15, 3, 13].

The effect of EIT is to eliminate the absorption of a radiation field in an atomic medium despite the field being on resonance with an atomic transition. The interaction $U = -\vec{d} \cdot \vec{E}$ between a dipole moment and a classical electric field drives transitions between energy levels on resonance.

First considering a simple two-level atom (Figure 1.1), we can write the Hamilto-

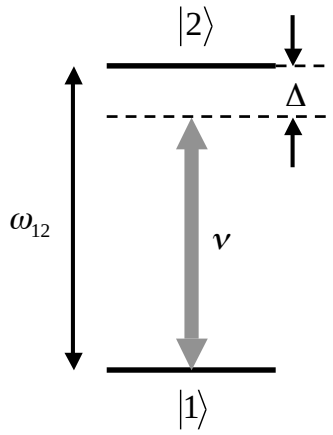

Figure 1.1: Simple two level atom with a single applied light field. The frequency separation of the levels is ω_{12} and the applied field has frequency ν (also an angular frequency, not always standard). The light field is detuned from resonance by an amount $-\Delta$.

nian

$$H = \hbar\omega_{12}|2\rangle\langle 2| - [|1\rangle\langle 2|\mu_{12} + c.c.]\left[Ee^{-i\nu t} + c.c.\right], \tag{1.1}$$

where in the second term we have the dipole operator ($\mu_{12} = \langle 1|\hat{d}|2\rangle$ is the dipole matrix element and gives the strength of the coupling between states) and the single mode EM field (in the dipole approximation where the field does not vary spatially over the atom's extent). The general time-dependent quantum state of such a system is

$$|\psi\rangle = c_1(t)|1\rangle + c_2(t)|2\rangle, \tag{1.2}$$

and using the Schrodinger equation one can write coupled equations that describe the time evolution of the system:

$$\dot{\tilde{c}}_2 = i\Delta\tilde{c}_2 + i\Omega c_1, \tag{1.3}$$

$$\dot{c}_1 = i\Delta\tilde{c}_2 + i\Omega^\star\tilde{c}_1, \tag{1.4}$$

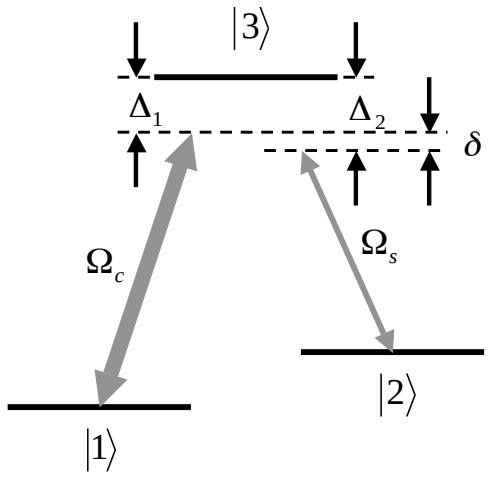

Figure 1.2: Three-level Λ-system used to demonstrate EIT. Two light fields are applied to the transitions, each detuned from resonance (Δ_1 and Δ_2), and with respect to the two-photon transition (the two-photon detuning $\delta = \Delta_1 - \Delta_2$).

or equilvalently as an effective Hamiltonian

$$H_{eff} = -\hbar \begin{bmatrix} 0 & \Omega^{\star}(t) \\ \Omega(t) & \Delta \end{bmatrix}. \tag{1.5}$$

This involved switching to a rotating frame $c_2 = \tilde{c}_2 e^{-i\nu t}$, and using the rotating wave approximation; this eliminates terms like $e^{+2i\nu t}$, which oscillate much faster than the populations, which follow the Rabi frequency $\Omega = \mu E/h$ (a measure of the strength of coupling to the light field) like

$$|c_2|^2 = \frac{1}{2}\left[1 + \cos\left(\Omega t\right)\right]. \tag{1.6}$$

EIT is a two-optical-field phenomenon, so we turn to the three-level Λ-system shown in Figure 1.2, where the application of two EM fields can be used to transfer or trap atoms into superpositions of the two ground states, whilst avoiding populating the excited state. The two applied light fields are denoted by their Rabi frequencies Ω_c (control field) and Ω_s (signal field). Following the same steps as for the two-level system, and following

the style of [15], we can write

$$H_{eff} = -\hbar \begin{bmatrix} 0 & 0 & \Omega_s^\star(t) \\ 0 & \delta & \Omega_c^\star(t) \\ \Omega_s(t) & \Omega_c(t) & \Delta_1 \end{bmatrix}. \tag{1.7}$$

If we for now assume the two-photon detuning, δ, is zero, then the time-dependent eigenstates and eigenvalues of the effective Hamiltonian are

$$|a^+\rangle = \sin\theta\sin\phi|1\rangle + \cos\theta\sin\phi|2\rangle + \cos\phi|3\rangle, \tag{1.8}$$
$$\text{with} \quad \hbar\omega^+ = \frac{1}{2}\hbar\left[\Delta + \sqrt{\Delta^2 + \Omega_s^2 + \Omega_c^2}\right];$$
$$|a^0\rangle = \cos\theta|1\rangle - \sin\theta|2\rangle, \tag{1.9}$$
$$\text{with} \quad \hbar\omega^0 = 0;$$
$$|a^-\rangle = \sin\theta\cos\phi|1\rangle + \cos\theta\cos\phi|2\rangle - \sin\phi|3\rangle, \tag{1.10}$$
$$\text{with} \quad \hbar\omega^- = \frac{1}{2}\hbar\left[\Delta - \sqrt{\Delta^2 + \Omega_s^2 + \Omega_c^2}\right],$$

where $\tan\theta = \Omega_s/\Omega_c$. Consider the following scenario, where the atom begins in state $|1\rangle$. Turning on the control field Ω_c first, states $|2\rangle$ and $|3\rangle$ are coupled and the eigenstates $|a^+\rangle$ and $|a^-\rangle$ become superpositions of $|2\rangle$ and $|3\rangle$ with energies split by $\hbar\Omega_c$ (these are ac Stark shifts). The atom is not coupled to the radiation and stays in $|a^0\rangle = |1\rangle$. Next turn on Ω_s, which would be absorbed without the preparation of Ω_c, but here the excited state (which is $|3\rangle = \cos\phi|a^+\rangle - \sin\phi|a^-\rangle$) has been split and the components of the $|1\rangle \rightarrow |3\rangle$ transition are out of phase and cancel, meaning there is no absorption. This means the atom does not gain energy and stays in the state with energy $\hbar\omega^0$, which is now a superposition of states $|1\rangle$ and $|2\rangle$. Turning off Ω_c will now similarly bring the atom into state $|2\rangle$. The population has coherently shifted from $|1\rangle$ to $|2\rangle$ with no absorption. This works as long as the atom can adiabatically follow the applied fields.

Writing $|a^0\rangle$ with Rabi frequencies, we have

$$|a^0\rangle = |D\rangle = \frac{\Omega_c|1\rangle - \Omega_s|2\rangle}{\sqrt{\Omega_c^2 + \Omega_s^2}}, \tag{1.11}$$

the state the atom follows in the presence of the fields. Returning to a non-rotating frame, we examine the coupling between $|D\rangle$ and the excited state. It turns out that $\langle 3|H_{int}|D\rangle$ is proportional to $\exp(i\omega_{13}t + iE_1t/h) - \exp(i\omega_{23}t + iE_2t/h)$ so if $\hbar\omega_{23} - \hbar\omega_{13} = E_2 - E_1$ (that is, two-photon resonance), then there is in fact *zero* probability of photon absorption. If both fields are applied to a medium, and one is swept across this resonance, the medium fluoresces due to absorption and spontaneous emission except when $\delta \approx 0$, where the medium becomes dark (ceases to fluoresce). Thus $|D\rangle$ is termed the "dark state." One can in fact write the effective interaction Hamiltonian as $H_{eff} = -|B\rangle\langle 3| - |3\rangle\langle B|$, where $|B\rangle$ is the "bright state" orthogonal to $|D\rangle$, and the dark state does not interact with the applied fields and the system is pumped into the superposition $|D\rangle$ (see Figure 1.3). Coherence in one basis becomes population transfer in another.

The coherent transfer of atoms into the non-absorbing, but resonant, dark state is the essence of EIT. If we follow the above scenario but without turning off Ω_c, the atom is trapped in the dark state while Ω_s is applied; Ω_s feels no effect of the medium and is transmitted when there would otherwise be substantial resonant absorption. This forms the basis of "slow light" as well, as one can take advantage of large resonant dispersion without the usual accompanying absorption, as described in the next section.

1.3 Slow light

The phenomenon of "slow light" is a direct consequence of EIT. When we shape a pulse with the field Ω_s, it travels without absorption on resonance, and with a reduced group velocity due to large dispersion. Drawing from the comprehensive review in [1], we begin

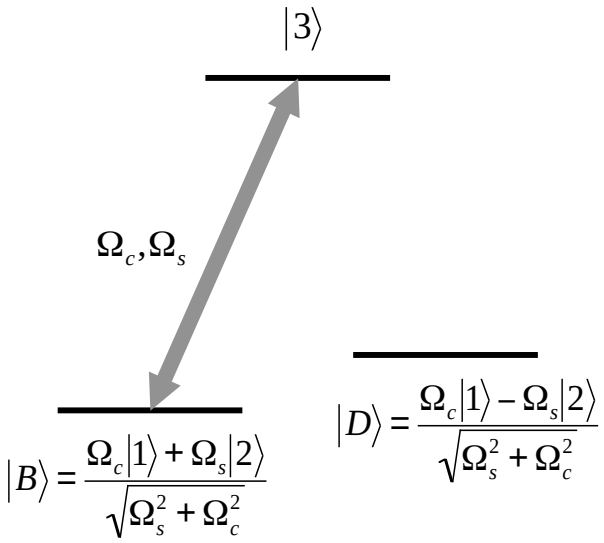

Figure 1.3: Three-level Λ-system redrawn in the basis of dark ($|D\rangle$) and bright ($|B\rangle$) states. The dark state is decoupled from the input light fields.

with a general pulse, which has some spread in frequency, each Fourier component adding in phase at the center of the pulse. If the pulse is to stay intact (that is, for its group velocity to be meaningful) the phase of each traveling wave field, $\phi = kz - \omega t = (n\omega/c)\, z - \omega t$, should be the same for all frequencies:

$$\frac{d\phi}{d\omega} = \frac{dn}{d\omega}\frac{\omega z}{c} + \frac{nz}{c} - t = 0 \rightarrow z = \left[\frac{c}{n + \omega(dn/d\omega)}\right] t, \tag{1.12}$$

where the term in square brackets is the group velocity of the pulse,

$$v_g = \frac{c}{n + \omega(dn/d\omega)}, \tag{1.13}$$

which scales like $\sim 1/\,(dn/d\omega)$ for large dispersion.

Now we connect the dark state formation in the three-level atomic system to the large $dn/d\omega$ that leads to slow light. The linear susceptibility (which relates to n by $n \sim 1 + \chi/2$) of the $|1\rangle \rightarrow |3\rangle$ transition that Ω_s couples is related to the coherence between those

states by

$$\chi_1 = \frac{N}{V}\frac{|\mu_{13}^2|}{\hbar\epsilon_0}\frac{\rho_{13}}{\Omega_s} = \frac{N}{V}\frac{6\gamma_{13}\pi c^3}{\omega_{13}^2}\frac{\rho_{13}}{\Omega_s}, \tag{1.14}$$

where γ_{13} is the decay rate from the excited state. One can write the effective three-level Hamiltonian from the previous section (Eq. 1.7), this time including decay rates, as

$$H_{eff} = -\hbar\begin{bmatrix} 0 & 0 & \Omega_s^\star(t) \\ 0 & i\Gamma_{12} & \Omega_c^\star(t) \\ \Omega_s(t) & \Omega_c(t) & i\Gamma_{13} \end{bmatrix}, \tag{1.15}$$

where $\Gamma_{12} = (\gamma_{12}/2) - i\delta$ and $\Gamma_{13} = (\gamma_{13}/2) - i\Delta_1$. The quantity γ_{12} is the ground state decoherence rate, which arises from many sources in a real experiment, as discussed in Section 1.5). If we assume Ω_s is weak compared to Ω_c and that atoms begin in state $|1\rangle$, they will generally not leave (in the dressed state picture, the mixing angle ϕ is small), so the coefficient $c_1 \approx 1$, and we can solve the differential equations and end up with

$$\chi_1 \propto \frac{\rho_{13}}{\Omega_s} = \frac{c_1^\star c_3}{\Omega_s} \approx \frac{c_3}{\Omega_s} = i\frac{\Gamma_{12}}{\Gamma_{12}\Gamma_{13} + \Omega_c^2}. \tag{1.16}$$

This is the susceptibility, and we note in particular how it depends on the frequency of the applied signal field. The imaginary part describes absorption, and again we find EIT, where on one- and two-photon resonance $\mathrm{Im}\left[\chi_1\right] \sim \gamma_{12}/\left(\gamma_{13}\gamma_{12} + \Omega_c^2\right)$, which is zero (the medium is perfectly transparent) as γ_{12} approaches zero. For δ not zero, but still small, $Im\left[\chi_1\right]$ takes a Lorentzian form like $\mathrm{Im}\left[\chi_1\right] \sim 1 - f/\left(1 + \delta^2/\gamma_{EIT}^2\right)$, where the width γ_{EIT} is

$$\gamma_{EIT} = \gamma_{12} + \frac{\Omega_c^2}{\gamma_{13}}, \Omega_c \ll \gamma_{13} \tag{1.17}$$

$$\gamma_{EIT} = \gamma_{12} + |\Omega_c|, \Omega_c \gg \gamma_{13} \tag{1.18}$$

So we can think of EIT as a transparency window for frequencies near resonance to travel through. The width of the window is determined by both the ground state decoherence rate and by the intensity of the Ω_c field (as is the "depth," f). Signal field (Ω_s) pulses

traveling through a medium with atoms prepared in the dark state must have bandwidths narrower than the window to avoid heavy loss from absorption.

The real part of the susceptibility χ_1 is (for $\Delta = 0$ and δ small) $\mathrm{Re}\left[\chi_1\right] \sim \delta/\left(\gamma_{13}\gamma_{12} + \Omega_c^2\right)$, which is zero on resonance (*i.e.*,$n = 1$), but dispersion $dn/d\delta$ is large, corresponding to a small group velocity scaling like

$$v_g \sim \frac{|\Omega_c|^2 + \gamma_{13}\gamma_{12}}{N}. \tag{1.19}$$

This is slow light. We note several features of this expression. Decreasing the intensity of the Ω_c field (but maintaining $\Omega_s < \Omega_c$, an earlier assumption used to find χ_1) reduces v_g, which we will use shortly to "store" a light pulse; decoherence rates are a hindrance to realizing ideal slow and stored light; a larger usable atomic density helps the process as well.

1.4 Stored light

"Stored light" may be achieved by taking advantage of "dynamic EIT" to transfer the quantum state of light in what has been called the signal field (Ω_s) into the ground state coherence of a large ensemble of atoms. To establish this picture, we will treat the field coupling states $|1\rangle$ and $|3\rangle$ (see Figure 1.2) as quantum mechanical. The interaction Hamiltonian then looks like

$$H_{int} = \hbar g \sum_{i=1}^{N} \hat{a}|3\rangle_i\langle 1|_i - \hbar\Omega_c(t)e^{-i\nu t}\sum_{i=1}^{N}\hat{a}|3\rangle_i\langle 2|_i + c.c., \tag{1.20}$$

where $\hat{a}$ is the photon annihilation operator, g the single-photon Rabi frequency, the summations are over all the atoms from i to N, and $|3\rangle_i\langle 2|$ can also be written like σ_{32}^i. Suppose all atoms begin in state $|1\rangle$, then the system can have atomic states like $|\mathbf{1}\rangle = |1_1, 1_2, \ldots, 1_N\rangle$, where all the atoms are in $|1\rangle$, as well as $|\mathbf{2}\rangle$, a symmetric superposition of states where one

atom is in $|2\rangle$, and the rest are in $|1\rangle$ (then $|\mathbf{2}\ \mathbf{2}\rangle$ where two atoms are in $|2\rangle$, and so on). The eigenstate of H_{int} with zero eigenvalue is (for one photon)

$$|D\rangle = \cos\theta|\mathbf{1}\rangle \otimes |1\rangle - \sin\theta|\mathbf{2}\rangle \otimes |0\rangle, \tag{1.21}$$

which is analogous to the dark state derived for classical field EIT earlier, where the mixing angle between ground states is given by $\tan^2\theta = g^2N/\Omega_c^2$. The inclusion of atomic density N is a new addition, as the ensemble of atoms enhances the process of coherence transfer. The dark state also has a general form for a larger number of photons n. As before, $\theta(t)$ can be adjusted by varying the $\Omega_c(t)$ intensity, transferring atoms from $|\mathbf{1}\rangle$ into various superpositions of $|\mathbf{2}\rangle$, $|\mathbf{2}\ \mathbf{2}\rangle$, etc. Another perspective is that the state of the quantized field is mapped into the atomic ground state coherence; rotating θ from 0 to $\pi/2$, the dark state $|D\rangle$ changes from $|\mathbf{1}\rangle \otimes |n\rangle$ into $|\mathbf{2}\ \mathbf{2}\ \mathbf{2}\ \mathbf{2}\ldots\rangle \otimes |0\rangle$. If rotating the mixing angle does this to Fock states of the field $|n\rangle$, it should do the equivalent operation to mixed states described by a density matrix, like

$$\sum_{m,n} \rho_{m,n}|m\rangle\langle n| \otimes |\vec{1}\rangle\langle\vec{1}| \rightarrow |0\rangle\langle 0| \otimes \sum_{m,n} \rho_{m,n}|\vec{2}^m\rangle\langle\vec{2}^n|. \tag{1.22}$$

In this quantized field picture, states of the light field are transferred to states of the atoms (density matrix elements are the same). This was done by varying the dark state using θ, this time with $|D\rangle$ of a whole ensemble. Treating the field as multi-mode (but still quantized) we can make a more direct connection to the slow light described earlier. The interaction Hamiltonian takes a similar form as above,

$$H_{int} = -\mu_{13}\sum_{i=1}^{N} \hat{E}^+(z_i)\sigma_{13}^i - \hbar\sum_{i=1}^{N} \Omega_c(z_i,t)\sigma_{23}^i e^{ikz_i - i\nu t} + c.c., \tag{1.23}$$

where the first series describes the quantized fields interacting with the $|1\rangle \rightarrow |3\rangle$ transition, and the second series the classical field Ω_c interacting with the $|2\rangle \rightarrow |3\rangle$ transition. As before we sum over the atoms in the ensemble, taking their positions into account. The

electric field operator $\hat{E}$ includes a slowly varying envelope $\mathcal{E}(z,t)$ that describes the shape of a pulse we send:

$$\hat{E}^{+} = \sqrt{\frac{\hbar\nu_s}{2\epsilon_0 V}}\mathcal{E}(z,t)e^{i\left(\frac{vz}{c}-ct\right)}. \tag{1.24}$$

If the envelopes change little over the scale of the atoms, the summations in the Hamiltonian become integrals, and one can use the Heisenberg operator picture (with the field operator $\hat{\mathcal{E}}$ and the transition operators $\hat{\sigma}_{ab}$ and where $d\hat{A}/dt = (i/\hbar)[H_{int}, \hat{A}]$ for some operator $\hat{A}$) to find a set of differential equations that give the time and space evolution of $\mathcal{E}$, σ_{11}, σ_{22}, σ_{33}, σ_{12}, σ_{13}, and σ_{23}. If we assume small $\mathcal{E}$, compared to the field Ω_c, and treat $\mathcal{E}$ as a perturbation, then most of the population stays in $|1\rangle$ and there is minimal interaction with the excited state $|3\rangle$, and we arrive at a pair of coupled equations for $\mathcal{E}$ and σ_{23}:

$$\left(\frac{\partial}{\partial t} + c\frac{\partial}{\partial z}\right)\mathcal{E}(z,t) \approx \frac{gN}{\Omega_c}\frac{\partial}{\partial t}\sigma_{12} \tag{1.25}$$

$$\sigma_{12} = -\frac{g}{\Omega_c}\mathcal{E}(z,t) - \left(\text{terms} \sim \frac{\partial}{\partial t}\frac{1}{\Omega_c} \text{ and } \frac{\partial^2}{\partial t^2}\sigma_{12}\right). \tag{1.26}$$

The first equation resembles the wave equation for the quantized field operator. If we then assume Ω_c changes slowly, the time derivative terms vanish and we combine the equations to find

$$\left(\frac{\partial}{\partial t} + c\frac{\partial}{\partial z}\right)\mathcal{E}(z,t) = \frac{g^2N}{\Omega_c}\frac{\partial}{\partial t}\left(\frac{\mathcal{E}(z,t)}{\Omega_c}\right). \tag{1.27}$$

Then if the field Ω_c stays fixed in time, we arrive at

$$\frac{\partial}{\partial t}\mathcal{E}(z,t) \approx \frac{c}{1+(g^2N/\Omega_c^2)}\frac{\partial}{\partial z}\mathcal{E}(z,t) = v_g\frac{\partial}{\partial z}\mathcal{E}(z,t) \tag{1.28}$$

and recover slow light, where the field envelope maintains its temporal shape and propagates slowly through the medium. Note that the group velocity scale inversely with g^2N, which is related to the optical depth of the system by $d_0 = g^2NL/\gamma c$, where L is the length of the medium.

We are still not able to write the state of the field (or pulse) to the atomic ensemble in the long-term, since the group velocity will carry information out the atomic medium. Relaxing the condition that Ω_c is time-independent, we can achieve (in principle) a complete and reversal transfer to the medium.

By writing the field operators $\mathcal{E}$ and σ_{12} in a new basis,

$$\Psi = \cos\theta(t)\mathcal{E}(z,t) - \sin\theta(t)\sqrt{N}\sigma_{12}(z,t), \tag{1.29}$$

$$\Phi = \sin\theta(t)\mathcal{E}(z,t) + \cos\theta(t)\sqrt{N}\sigma_{12}(z,t), \tag{1.30}$$

where $\tan^2\theta(t) = g^2N/\Omega_c^2(t)$, we can better understand the "dyamic EIT" that results from changing the strong field Ω_c. Studying the modes of the new field Ψ, provided that there are many more atoms than photons (so $\sigma_{11} \gg \sigma_{22}$ for most atoms), the modes have commutation relations like bosons, so we think of them as the equivalent of photons for the new field, and are called "dark state polaritons" (DSP). The equivalent of Fock states for the polaritons,

$$|n_k\rangle = \frac{1}{\sqrt{n!}}\left(\hat{\psi}_k^+\right)^n\left(|0\rangle \otimes |\vec{1}\rangle\right), \tag{1.31}$$

where the modes ψ_k come from Ψ being a sum of plane waves $\psi_k e^{ikz}$, are all dark states and $H_{int}|n_k\rangle = 0$, just like the dark states $|D\rangle$ that we originally discussed. Like before, we can vary $\theta(t)$ by varying the strong control field, this time the polaritons transfer coherently between being states of the quantized field and coherent superpositions of the atomic ground states. Equivalent to the above steps involving $\mathcal{E}$ and σ_{23}, we can find a coupled pair of differential equations describing how Ψ and Φ evolve. Then making the same assumptions about a small and slowly changing $\Omega_c(t)$, we find an equation of motion for Ψ of the same form as we did for $\mathcal{E}$:

$$\left[\frac{\partial}{\partial t} + c\cos^2\theta(t)\frac{\partial}{\partial z}\right]\Psi(z,t) = 0. \tag{1.32}$$

This is a shape-preserving wave equation, so we find the DSP field to be analogous to the light field, but where we change $\Omega_c(t)$ in time. This brings us "stopped light," as the group

velocity of the DSP is $c\cos^2\theta$. For very large Ω_c, we have $v_g = c$, and the polariton is entirely photonic. The consequence of slow light ($v_g < c$) is that atoms pick up ground state coherence from the state of the field carrying the pulse. If θ varies from 0 to $\pi/2$, the polariton is converted to entirely an atomic transition operator and the group velocity goes to zero as Ω_c is turned off. The process here is also reversible, since the polariton transfer is not based on dissipation (the excited state $|3\rangle$ is never entered by any atoms). That is, turning Ω_c back on, the original photonic field will exit the medium; thus a pulse has been slowed, stopped, and re-accelerated.

This is very much an idealized situation described here. We have generally ignored decoherence mechanisms, and assumed stationary atoms. In the next section we will discuss limitations and experimental implementation of the effect.

1.5 Nonideal behavior

We now move on from the idealized scenario of EIT, slow, and stored light. In discussing the idea of an EIT "window," and a pulse bandwidth to fit inside it, a ground state decoherence rate γ_{12} was introduced. There are numerous mechanisms that affect this rate and determine the shape of an absorption/transmission spectrum. Also mentioned earlier was the spontaneous decay rate from the excited state (γ_{13}). More mechanisms become apparent when we consider atoms to move around in an enclosed chamber, more closely matching experimental conditions in a vapor cell.

In the preceding sections our introduction of EIT treated a single atom. To understand effects of decoherence mechanisms requires statistics of a set of atoms, so here we use the density matrix approach. Beginning with the effective Hamiltonian for a general

three-level system (Eq. 1.7), we write density matrix elements with

$$i\hbar\frac{d\rho}{dt} = [H_{eff}, \rho] + R\rho, \tag{1.33}$$

where R is the relaxation operator and its term contains information about how level populations (diagonal elements) and coherences (off-diagonal elements) evolve due to effects not related to the atom-field coupling of H_{eff}. Broadly speaking, R includes the transfer of population from one state to another (including to states outside the system) and the loss of phase coherence between states. Ignoring R momentarily, in our three-level Λ system with no decay the rate equations for ρ are [13]:

$$\dot{\rho}_{11} = i\rho_{31}\Omega_s^\star - i\rho_{13}\Omega_s, \tag{1.34}$$

$$\dot{\rho}_{22} = i\rho_{32}\Omega_c^\star - i\rho_{23}\Omega_c, \tag{1.35}$$

$$\dot{\rho}_{33} = i\rho_{23}\Omega_c - i\rho_{32}\Omega_c^\star + i\rho_{13}\Omega_s - i\rho_{31}\Omega_s^\star, \tag{1.36}$$

$$\dot{\rho}_{12} = i\rho_{32}\Omega_s^\star - i\rho_{13}\Omega_c + i\delta\rho_{12}, \tag{1.37}$$

$$\dot{\rho}_{13} = i(\rho_{33} - \rho_{11})\Omega_c + i\rho_{21}\Omega_s - i(\Delta_1 - \delta)\rho_{13}, \tag{1.38}$$

$$\dot{\rho}_{23} = i(\rho_{33} - \rho_{22})\Omega_s + i\rho_{12}\Omega_c - i(\Delta_2 - \delta)\rho_{23}. \tag{1.39}$$

Note that $\rho_{ab} = \rho_{ba}^\star$. The couplings between the various elements make sense upon inspection. Populations depend solely on the fields coupling ground to excited states (the coherences); coherences depend on these same fields and on the relative population levels between the states they couple; the ground state coherence, which we are most concerned with, depends strongly on δ because establishing this coherence is a two-photon process. Each of these populations and coherences will change as a result of incoherent transfer of atomic states. By incoherent we mean that dissipative mechanisms such as spontaneous emission happen at unpredictable times so any superposition between the states will not evolve with a known phase; for example, the "dark state" that scaled like $\Omega_c|1\rangle - \Omega_s|2\rangle$

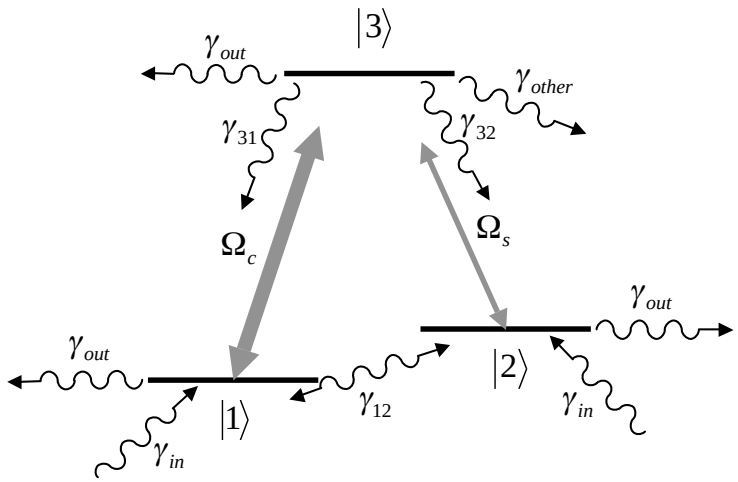

Figure 1.4: Three-level Λ-system with various decoherence rates illustrated. Specific mechanisms for coherence loss are discussed in the text.

would acquire "bright state" components of $\Omega_c|1\rangle + \Omega_s|2\rangle$ as the states evolved out of phase.

Figure 1.4 is an illustration of the various decays that can occur. This includes decay to energy levels outside the system, and the fact that atoms may leave the system and be replaced (either by new atoms, or by decohered versions of the original atom, which is indistinguishable). Including these decay mechanisms in the density matrix treatment yields a more general version of the evolution of the coherence between the ground state energy levels,

$$\dot{\rho}_{12} = i\rho_{32}\Omega_s^\star - i\rho_{13}\Omega_c - i\Gamma_{12}\rho_{12}. \tag{1.40}$$

The variable Γ_{12} incorporates both two-photon detuning δ and the decay rates to give the equivalent of a more generalized detuning. This was used in Section 1.3 when introducing slow light, and the γ_{12} rate given there could include a number of decoherence mechanisms, which we list and summarize below.

The experimental system used throughout this work is a Rb vapor cell. The geometry is as follows: a 2-d Gaussian beam enters a cylindrical vapor cell along its central axis.

The Rb is warm, and atoms are free to move in the cell. Thus, the decay rates γ_{out} and γ_{in} represent atoms leaving and entering the presence of the applied radiation fields. Atoms optically pumped into the dark state may leave the system, effectively a coherence loss rate. Similarly, unpolarized atoms can enter the beam, readily absorbing light and reducing EIT transmission. Unconfined atoms then have a coherence lifetime approximately equal to the time of flight of an atom through the laser beam (in anti-relaxation-coated cells, used in Chapters 5, 6 and 7, atoms may return to the beam with coherence intact).

Buffer gas is typically used to confine atoms inside the laser beam. Repeated collisions of the atoms used for EIT with buffer gas atoms slows their travel time through the beam. The coherence lifetime is then determined by the diffusion rate rather than the ballistic time of flight. Collisions with buffer gas atoms can also disrupt the dark state by introducing dephasing during collisions; thus the ground state decoherence rate cannot be made arbitrarily small by adding more buffer gas, as a high rate of dephasing collisions will broaden EIT linewidths. Collisions between the atoms used for EIT can also occur, although in practice much more rarely since densities are typically orders of magnitude less than for buffer gas atoms; spin-exchange collisions that destroy atomic coherence can become significant at high temperature, however.

Magnetic field gradients in the cell volume can also affect coherence for a system of atoms in the dark state. Magnetic fields shift energy levels via the Zeeman effect, introducing a two-photon detuning to EIT. The detuning affects the phase between states $|1\rangle$ and $|2\rangle$ in the dark state. If this phase varies spatially in the cell, then the dark state itself varies throughout the cell volume. This leads to absorption of the applied fields. A similar issue arises for EIT in the hyperfine configuration, where the control and signal fields have different frequencies. In this case the phase between the fields is the source of the effect; the relative phase between signal and control fields is also the phase between the two ground state

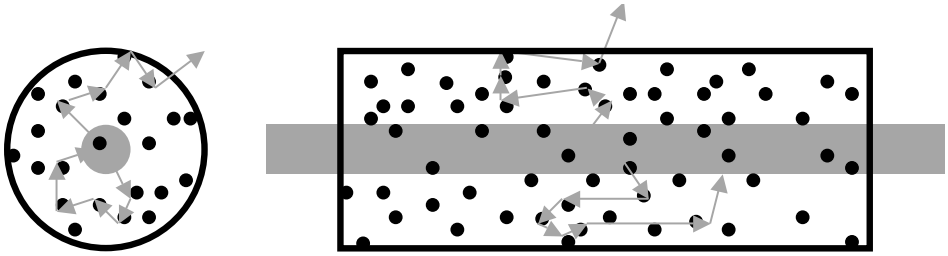

Figure 1.5: Schematic illustration of radiation trapping in a vapor cell. Absorbed photons are spontaneously emitted in all directions, and can be reabsorbed by atoms in the dark state. Atomic coherence is destroyed, possibly, a number of times before the emitted and re-emitted photon escapes the cell

components of the dark state superposition, and thus the dark state varies along the length of the cell. If atoms are not confined to a position much less than the hyperfine wavelength (either by buffer gas, or constrained using the cell geometry in a buffer-gas-free coated cell), then they will travel through regions where their dark state becomes the bright state, destroying their EIT coherence.

Radiation trapping [37, 38, 39, 40] in vapor cells is another effect that acts as an incoherent pumping mechanism. The effect is illustrated in Figure 1.5. Given the mechanisms described above illustrating the non-ideal nature of EIT, there will inevitably be absorption of incoming light. Excited state atoms will spontaneously emit photons into 4π. Such photons that are not emitted along the incoming field propagation direction can be re-absorbed by atoms that are in the dark state, which as a result lose their coherence. Depending on the transverse optical depth of the system, these absorption and re-emission events can happen multiple times before the atom leaves the system. Thus in systems with high optical depth, radiation trapping adds to the effective ground state decoherence rate. Its effect in our Rb vapor cell experiments, and efforts to mitigate the effect, are described in Chapters 4 and 5.

Finally, Figure 1.4 also introduced a decay term γ_{other}, whereby atoms in the

excited state that have absorbed photons can decay into states outside the simplified three-level Λ-system. Depending on the details of the energy level diagrams, such states can be "trapped" states that are inaccessible to the input light fields (See Section 2.3 in the next chapter). Rather than decay to one of the two ground states of the Λ-system, where such atoms could be re-pumped into the dark state, trapped state atoms cease to participate in EIT and limit the amount of coherence that can be established in the system. It turns out that experimental data is much better fit to a four-level model that includes a trapped state (as given in [41], for example) than to the simple three-level version, as we will see in Chapters 3 and 5.

1.6 Overview

This thesis presents a series of experiments aimed at optimizing slow and stored light in vapor cells and better understanding their limitations. The two primary aspects of this work are the role of optical depth in slow light performance, and an exploration of paraffin-coated vapor cells and the long-time-scale slow and stored light. Chapter 2 provides a detailed account of how we make measurements of the EIT, slow, and stored light described in this chapter, using ^{87}Rb vapor cells. It also includes experiments in the simplest type of vapor cell, a "vacuum" cell with no wall coating or buffer gas, which illustrate the need for a more developed understanding of the role of optical depth in vapor cells.

Chapter 3 develops a quantitative connection between slow light and EIT, starting with the simple three-level EIT model from Section 1.2, but cast in terms of directly measurable experimental parameters. This provides a practical, useful tool for predicting slow light behavior from simple EIT spectra; and because the prediction is based on measured EIT, it can take into account unanticipated decoherence effects not included in the three-level EIT

model itself. Chapter 4 continues the study of optical depth and stored light, working in buffer-gas-filled Rb vapor cells and investigating radiation trapping and the role of buffer gas and cell geometry on stored light performance.

The next three chapters present EIT, slow, and stored light in paraffin-coated vapor cells. The coating preserves coherence during collisions between atoms and the cell walls, allowing EIT-based experiments to operate on long time scales. Chapter 5 describes how EIT operates in coated cells, and how its lineshape is characterized by a dual structure, with a broad feature based on transit time, and a narrow feature based on time spent in the dark. Chapter 6 follows with a treatment of slow and stored light propagating through such EIT lineshapes. Slow light can be achieved with either time scale. Long storage times are observed in the coated cell, and a promising technique of using high-bandwidth slow light pulses using the broad EIT structure, while storing the light for long times supported by the wall coating, is investigated. Finally, Chapter 7 introduces a novel application of slow light in coated cells: the slow light beamsplitter, which divides input signal field light into spatially separated outputs. Thus coherence is established in one location, and quickly transported to another. The process is demonstrated to be phase coherent and may be beneficial in classical communication or quantum applications.

Chapter 2

Apparatus

There are many systems with which one can study slow and stored light and their applications. The remainder of this thesis describes work in warm rubidium vapor cells. This type of experiment provides a number of advantages, apart from the degree of slowing or storage quality obtained. One is that the physics of alkali atoms is more accessible and easier to model than more complicated systems such as molecules and solids; the three-level EIT Λ-system used in Chapter 1 captures a great deal of the behavior of a real alkali vapor.

Another advantage is the simplicity of the experimental setup surrounding the vapor cell. Relatively few optical components are required, even for a configuration that can easily switch between Zeeman and hyperfine transition experiments. Although construction of specialized blown-air ovens was needed, the experiments operate near room temperature and require little maintenance. This will be described in the first several sections of the present chapter.

Finally, the ability to construct our own vapor cells provides flexibility in investigating their potential as slow and stored light systems. Cells of various geometries, wall-coatings, buffer gases, and isotopical enrichment are employed throughout this work. Con-

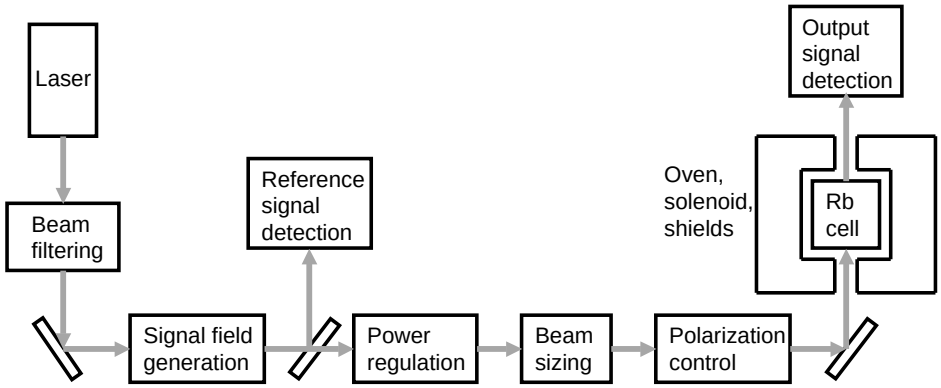

Figure 2.1: Schematic flow-chart style representation of the apparatus used throughout this work for EIT, slow, and stored light experiments.

struction methods are described in Appendix A.

What follows is a step-by-step description of the experimental apparatus, first discussing the optics used to generate the input light and detect the output light, then the specialized oven and magnetic shielding surrounding the vapor cell, then the Rb vapor cell itself. Lastly a short series of experiments using a Rb "vacuum cell" (*i.e.*, a cell with Rb metal and vapor, but no buffer gas or wall coating) is introduced. With vacuum cells being the simplest vapor cell, this serves as a convenient way to both introduce the slow and stored light quantities we typically measure, and to highlight the reasons we choose to use other cells with buffer gas or anti-relaxation wall coating. It also yields interesting results related to the role of Rb temperature (density), pointing ahead to the work in Chapters 3 and 4 where we explore the limitations of using high optical depth to improve slow and stored light performance.

2.1 Laser and optical components

The general schematic of the experimental apparatus used throughout the thesis is shown in Figure 2.1. Rather than listing specific components, this follows the path of the laser beam in flow-chart style through stages described by their function. Each is described below.

2.1.1 Laser and filtering

All experiments use external-cavity diode lasers operating at a wavelength of $\lambda = 795$ nm, which matches the D_1 transition resonance in ^{87}Rb, with the specific energy level transitions varying with the experiment. Lasers include a laser with a tapered amplifier (Toptica TA100 system) for high laser power uses, and New Focus Vortex lasers, which lower output power capability but a wide tuning range. The lasers have narrow bandwidths on the order of a few MHz. Since the Doppler linewidth for atoms in warm Rb vapor is typically ~ 500 MHz, we usually do not consider the laser linewidth.

The outgoing laser beam is then sent through a filter to clean its spatial mode, and the beam acquires a Gaussian profile (TEM_{00} mode). This is accomplished either with a spatial pinhole filter or by coupling into a single-mode optical fiber. In the spatial pinhole case, light is focused with a short-focal-length lens through a 25 μm pinhole and collimated on the other side. This reduces the output power by approximately 20%.

In the optical fiber case, a pair of fiber couplers on heavy mounts are placed after the laser, with light focused into a coiled single-mode fiber of length 2 m. The ends of the fiber are cleaved at an angle to avoid etaloning in the fiber. The fiber method cuts the usable laser power by $\sim 50\%$, but the filtering is improved, as measured on a beam profiler.

It should be noted that for either filtering method, the filter is covered with a box, in part to block scattered light for safety purposes, but also to reduce mechanical vibration

from air flow and temperature fluctuations, which can lead to output power and direction fluctuations in the laser beam.

2.1.2 Signal field generation

As described in Chapter 1, EIT is a two-optical-field phenomenon, requiring two input fields from our optical setup. They can be generated by either polarization-rotating or frequency-modulating a single input laser beam.

For slow light experiments based on Zeeman EIT (Chapters 5, 6, and 7), the ground state levels are degenerate in energy, but control and signal fields can interrogate different optical transitions if they have orthogonal polarization. A Pockels cell can accomplish this by rotating the polarization of its input light. A high-powered driver applies a strong electric field across a crystal, which changes the refractive index in one direction, and the device acts as a voltage-controlled wave plate. The strong control field enters and it's polarization is rotated by a small amount, and the orthogonal component becomes the signal field. The two fields propagate together as the same beam. A signal field pulse can be generated by varying the rotation angle as a function of time in the desired shape.

Using a Pockels cell for Zeeman EIT experiments can be disadvantageous for several reasons. First, since the signal field is generated by rotating the control field, any signal field comes at the expense of the control field. So a pulse generated in the signal field results in an anti-pulse in the control field. Time dependence in this field complicates the straightforward treatment of EIT from Chapter 1. Second, in practice Pockels cell drivers have difficulty forming either very long or very short pulses, the former due to power output limitations and the latter due to speed performance. Long and short time scales are both of great interest in EIT-based applications (long storage times of quantum information, and short time scale / high-bandwidth optical communications, for example), so a more flexible

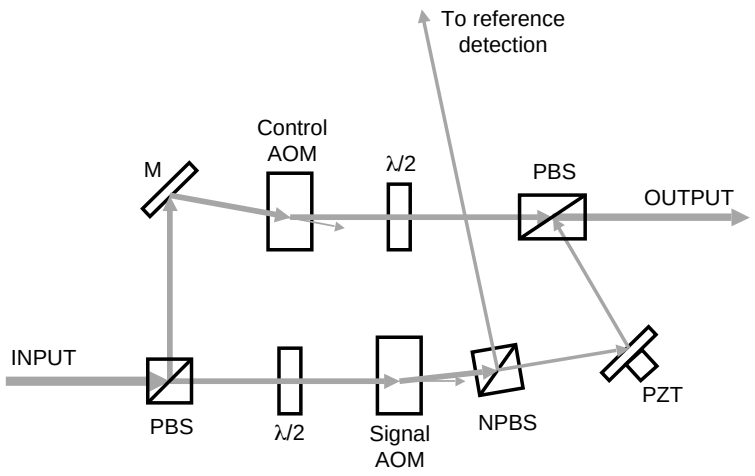

Figure 2.2: Schematic of a dual-AOM setup that allows for independent variation of control and signal field powers before recombining the fields into a single beam at the output.

arrangement is often preferred.

An alternative to the Pockels cell for Zeeman EIT experiments is a split beam, dual acousto-optic modulator (AOM) setup, schematically shown in Figure 2.2. Input light is divided by a polarizing beamsplitter (PBS) cube, and vertically polarized light in each path then passes through an AOM. Laser light diffracts from acoustic standing waves induced in the AOM's crystal. The frequency of the output light in the n^{th} diffraction order is shifted by nf, with f the driving frequency. The power in each mode is controlled by the relative beam/crystal orientation and driving voltage, with typically as much as 70 or 80% of the input power available for the $n = \pm 1$ order at the output. In our configuration, the frequency of light in both beams is downshifted by 80 MHz and the -1 beam is used from each.

The split-beam configuration allows independent variation of the control and signal field powers. Pulses can be generated in the signal field by sending a Gaussian (our typical slow light pulse shape) voltage profile to the AOM driver, and the AOM essentially acts

as a fast variable switch. The response time is sufficiently fast for short temporal (high bandwidth) slow light pulses, and has no trouble generating long time scale pulses.

Half the signal field light is picked off with a non-polarizing beamsplitter (NPBS) cube and used as a reference (see below). The control beam and remaining signal field beam are recombined at a high-exinction-ratio Glan-Thompson polarizer and travel together at the output. Any small polarization defects accrued should be filtered out by the polarizer. Having traveled nearly identical path lengths while encountering only flat surfaces, the beams remain essentially the same size and we can consider a single beam with orthogonally-polarized control and signal fields present.

The setup in Figure 2.2 resembles an interferometer, and indeed will include interference effects when light traveling the two separate paths is out of phase. The mirror in the signal field path is attached to a piezo-electric transducer (PZT), and can be moved slightly to vary the signal field path length by the optical wavelength (795 nm) or more, and can thus be tuned such that the control and signal fields are in phase. It should also be noted that the dual-AOM setup is enclosed in a box to ensure mechanical and temperature stability in the AOM interferometer.

For slow light experiments based on hyperfine EIT (Chapters 3, 4, and parts of Chapter 5), the two lower energy levels are the $F = 1$ and $F = 2$ hyperfine levels, which are separated by 6.835 GHz. Control and signal fields need frequencies that differ by this amount to achieve two-photon resonance and operate under EIT conditions.

This is accomplished using an electro-opitc modulator (EOM). Light into the EOM is frequency-modulated and acquires sidebands at $\pm$ the EOM's driving frequency from the input carrier frequency. So if the input (conrol field) is tuned to one optical transition, driving the EOM at 6.835 GHz produces a sideband (signal field) of higher frequency at the other optical transition, and an additional sideband of lower frequency far off resonance.

The off-resonant sideband can be used as a reference to calibrate the maximum signal field level.

Changes in the two-photon detuning from EIT and pulse shape can both be controlled via the EOM. Sweeping the EOM's driving synthesizer across the hyperfine transition frequency scans across EIT resonance, while the sideband amplitude can be controlled by varying the synthesizer output power. As with the AOM system described above, Gaussian pulses can be shaped in sideband amplitude to generate the desired pulse.

2.1.3 Power regulation

An AOM, described above, can be used to control the laser power, from nearly zero power up to $\sim 80\%$ of the input power, since only the -1 order beam is sent to the vapor cell afterwards. The dual-AOM configuration for Zeeman EIT experiments already includes the power regulation stage, as the voltage from the control field's driver can be varied to change the output power, and similarly for the peak voltage of signal field pulses. For the Pockels cell Zeeman EIT configuration and the EOM hyperfine EIT configuration, an AOM is placed after the signal field generation stage to vary the laser power. In experiments with a second beam (third light field) entering the system (the repumper field in Chapter 6 and the second control field in Chapter 7), an additional AOM is used to regulate its power.

Apart from controlling overall power for EIT and slow light experiments (whose results are normally quite sensitive to laser intensity), the AOM plays an important role in stored light experiments by rapidly turning off the control field while the slowed pulse travels through the atomic medium (Section 1.4). The speed of the shut-off is fast ($\lesssim 100$ ns) compared to the pulse width, but still slow enough to stay in the adiabatic limit (Section 1.2).

2.1.4 Beam size and polarization control

After the signal field has been generated, and both control and signal fields travel in a single beam with the appropriate power level, the beam size is determined by lenses in a telescope configuration (or a pair of telescopes), with collimated light of the desired size at the output.

The beam remains Gaussian in all experiments in this work, with the exception of the "flat-top" beam used in Chapter 3. There, the beam is expanded with a short focal length lens and collimated at a size of ~ 20 mm in diameter, then sent through a smaller iris. This diminishes available power, but generates a beam with an approximately uniform intensity (a power vs. radial position graph is flat, then falls to zero at a well-defined edge). This becomes necessary in the Chapter 3 work, which tests a prediction based on a Lorentzian EIT lineshape, which is not found using beams with transverse intensity gradients, particularly at high power [42, 43].

Light fields entering the Rb vapor cell are converted from linear to circular polarization using a quarter-wave plate ($\lambda/4$). For Zeeman experiments the control field is σ^+-polarized and the signal field is σ^--polarized, while in hyperfine experiments both fields have σ^+ polarization.

2.1.5 Reference and output signal field detection

Detection of the weaker signal field is the primary concern of the output optics; the strong control field serves to prepare the medium to have a certain effect on the signal field (transmission on resonance for EIT, slowing signal pulses for slow light), but is filtered out afterwards to observe our results. Also, the degree of the transmission or slowing in the output signal field must be observed relative to signal light that has not passed through the Rb cell, so an input reference is required.

Polarization separation of the output is used for Zeeman EIT experiments. A second $\lambda/4$-plate converts the control and signal fields back into orthogonal linear polarizations. Then, in the reverse operation of combining beams in the dual-AOM setup, a Glan-Thompson polarizer is used to separate the two fields, and the signal light is detected with an amplified photodetector.

Hyperfine EIT experiments use frequency separation, either in electronic signals or at the optical stage. In the electronic signal version, output light (control, signal, and off-resonant fields) is coupled into an optical fiber and sent to a fast photodetector, along with a small amount of the original control field (*i.e.*, before the EOM signal field generation or AOM power regulation) coupled into the same fiber. The additional control field is needed for beatnote detection in order to distinguish between the signal field (+1 EOM sideband) and the off-resonant reference field (−1 EOM sideband). The fast photodetector signal is then sent to a spectrum analyzer, where any of the three output fields from the Rb cell can be measured. Because the AOM shifted frequencies of the control, signal, and off-resonant fields by −80 MHz, the control field can be measured by looking at the beatnote electronic signal at 80 MHz; the signal field at 6.835 GHz + 80 MHz; and the off-resonant field at 6.835 GHz − 80 MHz. Disadvantages of this detection method include noise in the optical fiber (imperfect coupling of two beams, and mechanical vibrations), and the spectrum analyzer's inability to accurately show and record fast pulses when operating in zero span mode for beatnote detection.

A second method for hyperfine EIT signal field detection is to use an etalon at the output, set to transmit light near the signal field's frequency. The temperature-stabilized etalon device employed is shown in Figure 2.3. The etalon is a 5 mm thick disc of glass secured in the center of a cylindrical aluminum frame. It's free spectral range is 20 GHz and its finesse is 30. On each end is an anti-reflection coated window. A thermistor is

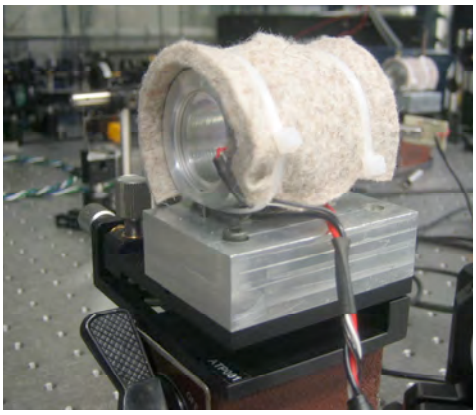

Figure 2.3: Temperature-stabilized etalon setup. The etalon filters the control field and the off-resonant sideband field, transmitting the signal field for detection in hyperfine EIT and slow light experiments.

inserted into a hole drilled into the edge of the cylinder, and the cylinder is surrounded by felt insulation. The etalon, windows, and cylinder sit atop a thermo-electric cooler (TEC), with an aluminum block acting as a reservoir underneath. This in turn sits on a 2-axis mount for adjusting the etalon's orientation with respect to the incoming laser beam. The temperature sensor and TEC run in a feedback loop using a PID temperature controller. The etalon thickness is set by its temperature, which determines the wavelengths that are allowed to propagate through it. The control field is extinguished by a factor of ~ 200.

The control or off-resonant sideband field could be detected with the etalon given the appropriate temperature setting, but this would require waiting for the temperature to re-stabilize. Another method is to take advantage of the etalon's free spectral range by instead tuning the central laser frequency below resonance. Tuning the laser ~ 5.4 GHz below its normal operating point means the off-resonant sideband is ~ 12.2 GHz below resonance, or ~ 20 GHz below the normal signal field frequency. This frequency difference of 20 GHz matches the free spectral range of the etalon, so the off-resonant field can be directly detected without adjusting the etalon. This field has the same power as the signal

field, but is sent through the Rb cell far off-resonance, and thus serves as a reference for the maximum possible EIT transmission level, or maximum stored light pulse area.

In both Zeeman and hyperfine types of experiments, a portion of the beam is picked off before the Rb cell. In the dual-AOM configuration this occurs directly in the signal field path, as shown in Figure 2.2, and that beam is sent to a photodetector. In the Pockels cell Zeeman configuration, a NPBS cube is placed after the Pockels cell, and the reflected beam is sent through a polarizer and into a photodetector, as a way to measure the input signal field. In pulse experiments, this provides a time reference for extracting pulse delay; in stored light experiments it provides the shape and (with proper calibration) the power of the input signal field pulse. In the EOM hyperfine configuration, the beam after the EOM is similarly picked off, and sent into a second temperature-stabilized etalon for the same purpose of isolating the input signal field.

With the input and output lasers and optics discussed, we turn to the part of the apparatus immediately surrounding the Rb vapor cell: the magnetic shields, solenoid, and specialized blown-air oven. Then we discuss the vapor cell itself (and again in more detail in Appendix A), before moving on to the short series of "vacuum cell" experiments at the end of the chapter.

2.2 Vapor cell ovens

In this section we describe the shielding, solenoid, and blown-air oven that houses the Rb vapor cells. Three layers of high-permeability magnetic shields surround the solenoid, oven and Rb cell. The shielding is made of "MuMetal," a nickel-iron alloy with a small amount of molybdenum added. Its high permeability allows its magnetic domains to align opposed to external magnetic fields (from the Earth's field, the steel optical table, nearby

electrical equipment, etc.), effectively screening these fields such that no net magnetic field exists inside the cylinders. The cylinders have holes in the center of their removable end caps, for optical access. When the shields are moved on the optical table, experience large temperature changes, or are otherwise mechanically disturbed, they must be "de-Gaussed" to reset the magnetic domains. This involves sending high electric current (~ 200 A) through a cable traveling through the inside shield layer, slowly ramping the current to zero.

Several sets of shields are used throughout this work, the size dictated by the shape and type of vapor cell used. The long, narrow cells used in the buffer gas experiments of Chapters 3 and 4 operate inside long shields (diameter 19 cm, length 41 cm); most coated cell experiments in the remaining chapters operate in larger shields (diameter 36 cm, length 43 cm) to provide a more homogeneous magnetic field environment to observe very narrow resonances.

Just inside the innermost magnetic shield layer is a solenoid. Apart from the primary zero order uniform field, the solenoid has separate end coils to more closely approximate an infinite solenoid, and to cancel magnetic field gradients that might remain despite the layers of shielding. In hyperfine EIT experiments, the solenoid is only used to zero the magnetic field seen by the Rb atoms, keeping Zeeman sublevels degenerate. In Zeeman EIT experiments, the a zero order magnetic field is used to shift the control and signal fields off two-photon resonance. Since the fields travel as a single beam with polarization their only difference, there is no way to directly change their relative frequency. Instead, applying a magnetic field to the Rb atoms shifts the ground state energy levels (by 700 kHz/G, if $\Delta m_F = 1$). Thus, to measure a Zeeman EIT line shape, the magnetic field is swept across zero while the output signal level is observed.

The Rb vapor cells are usually heated in order to raise the Rb density, increasing the amount of light-atom interaction. This must be done carefully to avoid introducing

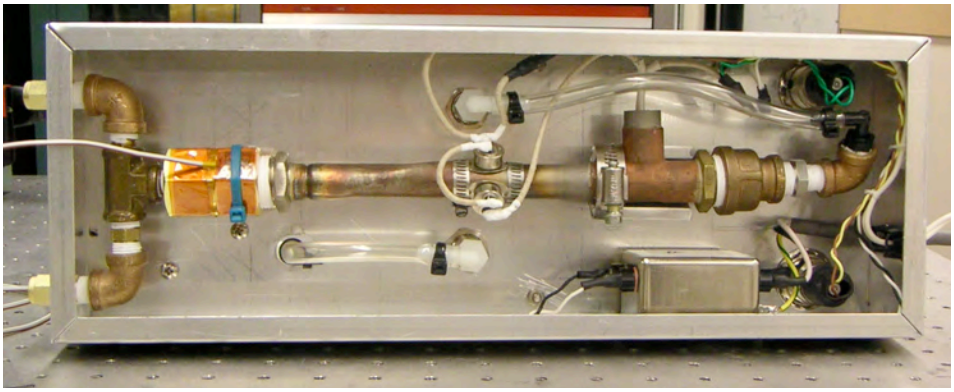

Figure 2.4: Heating device used to generate warm air, sent into the vapor cell ovens.

mechanical vibration, unwanted temperature gradients, or magnetic field gradients near the cell.

One method of heating vapor cells is to use resistive heaters. These must be placed outside the innermost magnetic shield layer, lest currents in the resistive wires introduce magnetic fields at the cell. Temperature changes to the shield layer can also affect its screening capability. Further, this places the heat source far from the cell, and for many cells it is necessary that the center be kept at a higher temperature than the outer Rb arm (see below). For these reasons, resistive heating is not used in the vapor cell experiments presented in this work. Another method is to use blown warm air on the cell, where the cell is in a sealed chamber with small holes for input and exhaust. This lacks precise control over how different parts of the cell are heated (although a conductive "cold finger" can thermally connect part of the cell to the cooler outside air temperature), and moving air surrounding the cell induces unwanted mechanical vibration. The direct blown-air method is also avoided.

We employ an indirect blown-air heating method in all vapor cell experiments. The air-heating device is shown in Figure 2.4, where room-temperature, compressed air from the

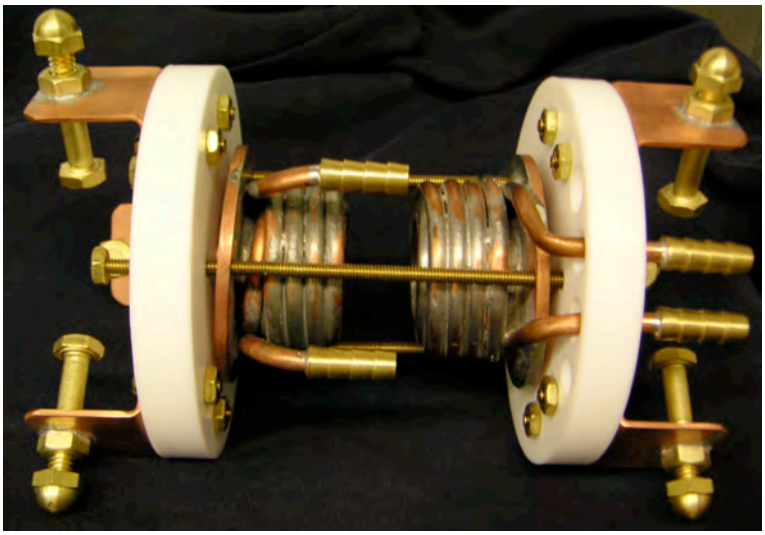

Figure 2.5: Early version of an indirect blown-air oven used to heat Rb vapor cells.

outside enters a pressure regulator and flow meter. It then passes through a copper pipe (from right to left in Figure 2.4) with the heating element, and finally forks at the output, where insulated silicone hoses carry the flowing air to the cell oven. The heater is controlled by a solid state relay, operating in a PID feedback loop using either the temperature sensor at the heater box output, or (more often) a temperature sensor attached directly to the Rb cell.

The oven itself is placed inside the magnetic shielding and houses the Rb vapor cell. Flowing warm air heats the oven, which in turn conductively heats the cell, avoiding the issues related to direct application of blown air on the cell. An early version of such an oven appears in Figure 2.5. Copper tubing carries the warm air, and is coiled in two pieces, which fit at each end of the cell, and each half is heated from one output of the heater box. In this configuration the middle of the cell is heated less than the ends. It is essential that the cell windows remain warmer than the rest of the cell, since solid Rb accumulates at the coldest locations; Rb metal on the cell windows would scatter incoming laser light. This

Figure 2.6: The cylindrical Nylatron oven used for heating Rb vapor cells. Note the Rb arm sticking out the bottom, done this way to maintain the Rb at a lower temperature in wall-coated cells.

oven is comprised of pieces made of materials that are nominally non-magnetic (copper, brass, teflon, and the solder), but in practice the oven introduced large field gradients in the cell, a result of thermoelectric currents generated due to heat flow between the different metals. As a result, this oven is only used for the vacuum cell results presented at the end of this chapter.

A different design also uses blown warm air, but no metal components. In addition to windows being kept at a higher temperature, a requirement for wall-coated vapor cells is that the Rb arm be the coldest part of the cell; solid Rb accumulating in a spot on the walls of the main cylinder nullifies the coherence-preserving effect of the coating at that spot. Thus the oven is composed of a solid plastic Nylatron (MoS_2-filled nylon) block or cylinder, with the Rb arm of the cell outside the heating source. A cylindrical version of the oven is shown in Figure 2.6, and a rectangular block version in Figure 2.7.

In both designs, the solid Nylatron section has four long holes for warm air to travel, placed around the center of the oven where the cell is located. Blown air in the silicone hoses couples to the oven with threaded nylon adapters, and enters the oven at two

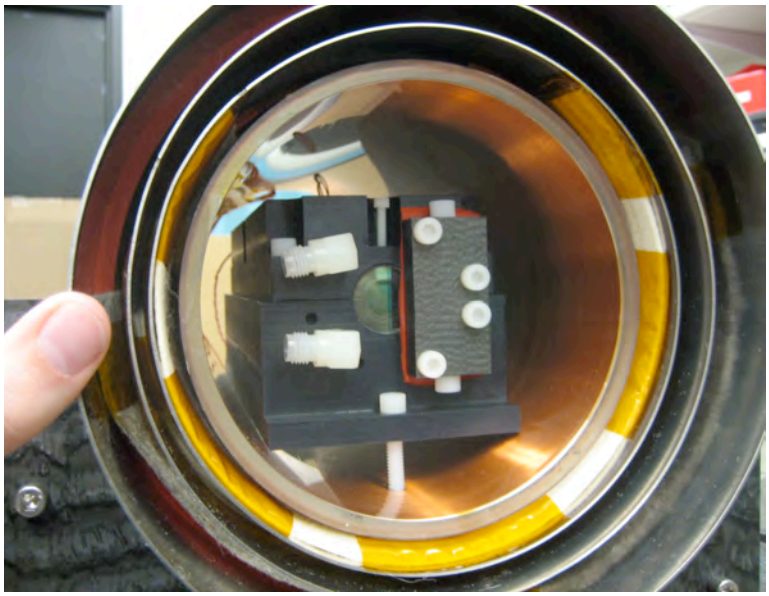

Figure 2.7: The Nylatron block oven used for heating Rb vapor cells. Shown (with end caps removed) in the MuMetal magnetic shields, with a solenoid formed around a polycarbonate cylinder inside the innermost layer.

holes on opposite sides of the cell. It then travels down the length of the oven, where it turns around and comes back through the other two holes, after which it leaves the system. The heated Nylatron conductively heats the cell walls, and anti-reflection coated windows are placed at the ends of the oven to impede surrounding air from cooling the cell windows. The Rb arm of the cell sticks outside the bulk Nylatron (as seen in Figure 2.6), and as a result is heated to a temperature several °C colder than the walls.

2.3 Rb cells and Rb

The Rb vapor cells used throughout this work are sealed cylindrical Pyrex chambers with a small amount of solid Rb inside (typically less than 10 mg). Vapor pressures are of order 10^{-7} to 10^{-5} Torr (number density 10^{10} to 10^{12} cm^{-3}), and this vapor serves as the atomic medium for EIT, slow, and stored light experiments. The cylindrical shape

allows optical access with minimal distortion. Details of cell construction are provided in Appendix A, but a brief summary of the types of cells used and their construction follows.

Buffer gas cells are the most straightforward. An empty cylindrical Pyrex cell (or multiple cells) begins attached to a system of tubing (also Pyrex), which includes an arm with a small container of solid Rb, and a port that connects to a vacuum pump, pressure sensor, and access to a container of the desired buffer gas. The system is pumped down to low pressure, then the Rb is "chased" (distilled) into the cell by heating a path from the solid Rb container to the cell; the Rb gas moves along the path, as it does not stick to the heated glass. Afterwards the path to the vacuum pump is closed with a valve, and buffer gas of the desired type and pressure is introduced. The completed cell is then "pulled off" the system by melting the glass tube next to the cell. Buffer gas cells are often purchased commercially.

Anti-relaxation wall coated cells involve more complicated steps. The walls are coated with tetracontane ($C_{40}H_{82}$), a derivative of paraffin. The initial setup is similar to that of buffer gas cell construction, with the addition of a valve just outside the cylindrical cell. Paraffin flakes are placed inside the system, either outside the cell or melted onto the end of a thin glass rod inserted into the cell. After evacuating the system with the vacuum pump, the valve near the cell is closed and the cell and glass tube between the valve and the cell are heated. Both are heated above the vaporization temperature of the paraffin (~ 200 °C), then after approximately 2 hours the system is cooled carefully down to room temperature. The cell walls must remain colder than the tube to ensure that the paraffin is deposited in the cell; and all parts of the cell must be at a uniform temperature to ensure the paraffin is not deposited at one cold spot. The end result is a cell with a uniformly thin layer of coating on its inside walls.

Rubidium is then distilled, as in the buffer gas case, except it is distilled not into

Figure 2.8: A paraffin-coated vapor cell. Length is 5 cm and diameter is 2.5 cm. Note the sidearm (pointing out of the page), branched out of the main cylindrical cell body, as a way to store Rb metal, keeping it from sticking to the coated walls.

the cylindrical cell, but into a sidearm located just outside it, as seen in the completed coated cell shown in Figure 2.8. Metal Rb should be kept out of the main cylinder. The cell is then pulled off the system and completed.

A final topic related to the cell making process is isotopical enrichment. All experiments in this work use ^{87}Rb, but natural abundance Rb is 72% ^{85}Rb. Thus it is preferred to use isotopically enriched ^{87}Rb, which results in higher density (optical depth) at a given temperature, and eliminates the possibility of collisions with ^{85}Rb atoms at high temperature. Commercial cells can be purchased with ^{87}Rb inside, but due to the high cost using bulk ^{87}Rb metal for homemade cells can be difficult. Instead, in place of the Rb metal in the cell making process described above, we can use a mixture of crushed enriched Rb salt (^{87}RbCl) and CaH_2. When heated, the two substances react, producing: ^{87}Rb metal, which is distilled into the cell as normal; H_2, which is pumped away by the vacuum pump; and CaCl , which remains behind as a powder.

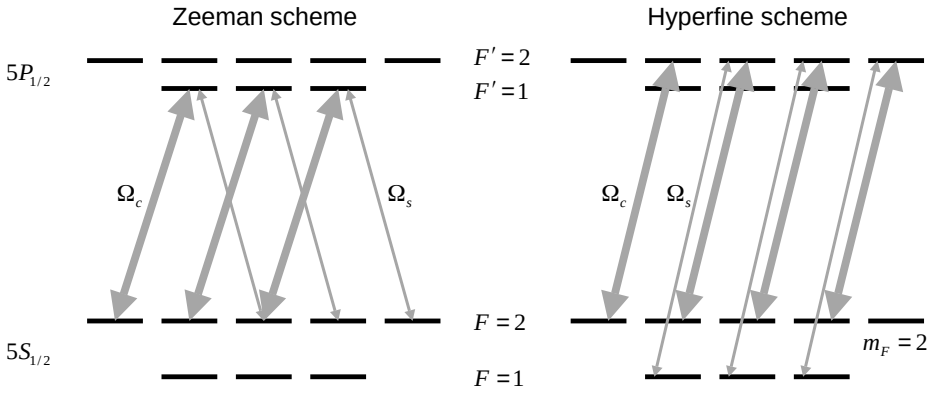

Figure 2.9: The full 16-level energy level diagram for the ^{87}Rb D_1 transition. The levels and applied light fields (control and signal) are shown for Zeeman EIT conditions on the left and hyperfine EIT conditions on the right.

As stated above the ^{87}Rb atomic vapor is the medium for EIT, slow, and stored light experiments. The relevant energy levels and applied light fields for the D_1 transition are shown in Figure 2.9. As noted above, the ground state hyperfine splitting is 6.835 GHz. The excited state splitting is 817 MHz, which is comparable to the Doppler linewidth; thus $F = 2 \rightarrow F' = 2$ transitions can occur in the Zeeman EIT configuration. This negatively affects EIT performance because the dark state for the $F = 2 \rightarrow F' = 1$ Λ-system is the bright state for the $F = 2 \rightarrow F' = 2$ Λ-system, resulting in absorption and loss of coherence. For the D_2 line, the excited states are less than a Doppler width apart, and this problem is more pronounced.

Also noticeable from these energy level diagrams is that some ground states are not accessible to the applied control and signal fields. This includes all three $F = 1$ states for Zeeman EIT, and the $|F = 2, m_F = 2\rangle$ state for hyperfine EIT. Atoms optically pumped into these states remain there, effectively reducing the optical depth of the system. This will be important throughout this work as we seek to optimize conditions for slow and stored light.

Figure 2.10: Natural abundance Rb vacuum cell (no buffer gas, uncoated walls). Length is 7.5 cm and diameter is 2.5 cm. Metallic Rb can be seen in the center. The cell is resting on J. Vanier and C. Audoin, *The Quantum Physics of Atomic Frequency Standards*, Institute of Physics Publishing (1989).

2.4 Vacuum cell EIT, slow, and stored light

The most straightforward system in which to introduce EIT, slow, and stored light experimental measurements is in a vacuum Rb cell, containing no buffer gas and with uncoated walls. Atomic motion is entirely ballistic rather than diffusive, and any experiment or measurement involving atomic coherence must be performed on the time scale of an atom crossing the laser beam once. This is because ground state coherence is lost in collisions with the uncoated cell walls. Except at very high temperatures, rubidium atoms rarely collide given their very low number density.

The experimental apparatus is the Pockels cell version of the Zeeman EIT configuration. The cell is housed inside the copper-tubing oven (Figure 2.5), and the cell itself is a natural abundance Rb vacuum cell, shown in Figure 2.10. Slow and stored light were studied for a range of temperatures, in particular how moving the system off one- and two-photon resonance affected the slow light delay and stored light efficiency. Earlier work [44] claimed that the readout area of a stored light pulse is a function of the quantity $\delta/gN^{1/2}$ (δ the two-photon detuning, g the single-photon Rabi frequency, and N the atomic density), which

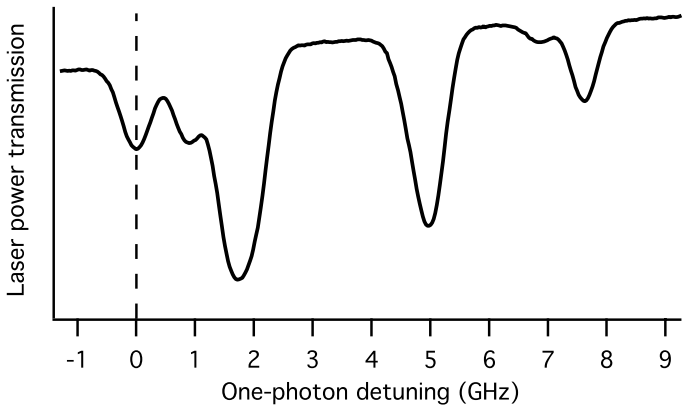

Figure 2.11: One-photon transmission spectrum using natural abundance Rb. The largest two dips in the center are ^{85}Rb resonances. Laser frequency is measured with respect to the lowest frequency transition, $F = 2 \rightarrow F' = 1$ in ^{87}Rb. The slight overall slope is due to feed-forward in the laser controller.

suggests that larger two-photon detunings could be tolerated in an optically thicker medium. In this section we will test this prediction, and use the slow and stored light measurements to illustrate the use of the apparatus described in the preceding sections.

The transmission spectrum for natural abundance Rb appears in Figure 2.11. The laser frequency is swept linearly across all the D_1 line resonances, using a reference cell not located in the magnetic shields. All four ^{87}Rb transition dips are visible, while both pairs of ^{85}Rb transitions (neither pair is resolvable) appear as two dips in the middle. For Zeeman EIT configuration measurements the laser is tuned to the lowest frequency resonance, $F = 2 \rightarrow F' = 1$.

EIT spectra are measured by monitoring the output signal field while sweeping the magnetic field across its zero value. Knowing the conversion for function generator voltage to solenoid current, current to magnetic field, and magnetic field to Zeeman frequency shift, the linewidth maybe be determined. The EIT spectrum is approximately Lorentzian in shape (not shown here, but shapes are shown throughout subsequent chapters) with a FWHM of

~ 100 kHz at the laser power used in slow and stored light measurements.

Reducing laser power narrows the EIT lineshape to a minimum of 30 kHz. This value is consistent with the coherence loss rate being dominated by the transit time of atoms through the beam. For the $d \approx 3$ mm diameter beam and a thermal Rb average speed of $v_{avg} \approx 300$ m/s, the average transit time for an atom across the beam is $T = 10$ μs. This implies a full width of the spectrum of $\gamma_{EIT} = 1/\pi T \approx 30$ kHz. Greater laser power would further broaden the EIT lineshape, allowing high-bandwidth signals to propagate, although any storage or other manipulation is limited to a 10 μs time scale. Later experiments in Chapter 6 allow us to use the high-bandwidth transit-time based EIT, but perform experiments over long time scales due to the presence of anti-relaxation coating on the cell walls.

Slow light pulses are generated by sending a time-varying voltage signal to the Pockels cell driver, rotating its output polarization in a Gaussian shape. The laser is put on one-photon resonance ($\Delta = 0$) and the magnetic field is set such that the probe is at the peak of the EIT resonance ($\delta = 0$). The pulse of width 2 μs propagates with reduced group velocity, and is measured in the signal field detection channel after the Rb vapor cell. A portion of the signal field light is picked off prior to the cell and is measured on a separate detector, and both pulses are displayed in Figure 2.12.

The input reference pulse is a distorted Gaussian shape (distorted due to the Pockels cell driver's speed limitations) of temporal width 1.9 μs, while the output pulse is somewhat broadened to a 2.2 μs width and is clearly time-delayed with respect to the reference. The pulses are shown normalized to be the same height to most clearly show the delay; in reality the output signal field peak level is reduced due to absorption. The large ground state decoherence rate (due to transit time) leads to reduced peak EIT transmission (physically this arises from atoms that were optically pumped into the dark state leaving the system

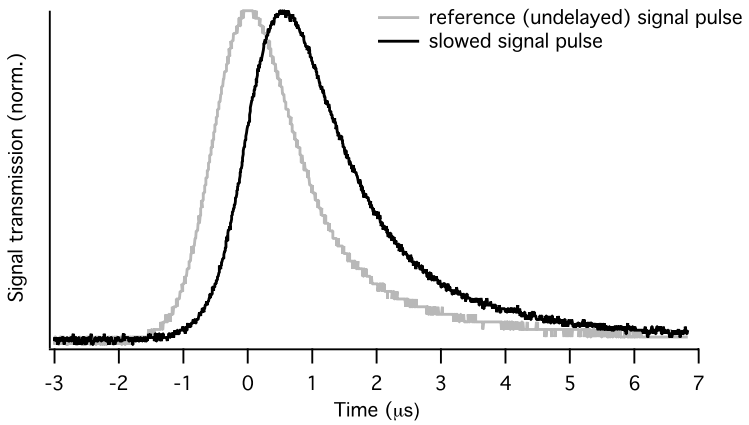

Figure 2.12: Slow light in a natural abundance Rb vacuum cell. Temperature is $T = 65$ °C. The pulse is delayed by 625 ns, and the fractional delay is 0.32. Time is measured from the center of the input reference pulse.

and being replaced with unpolarized atoms that absorb the signal field light). Despite the fairly high atomic density (10^{11}cm^{-3} at $T = 65$ °C), the effective optical depth is diminished due to atoms in the excited state decaying into the trapped $F = 1$ levels (see Chapter 3), limiting the amount of slow light delay.

Absolute slow light delay is defined as the difference between arrival times of the peaks of the input reference pulse and the output signal pulse. Here that value is 625 ns. Fractional slow light delay is defined as the absolute delay divided by the input pulse width, which here is 0.32. A term for this used in optical communications is the delay-bandwith product. A fractional delay of unity means the pulses are separated by the width of the input pulse. A fractional delay of 2 means almost complete temporal separation between input and output pulses, implying that the delay is sufficient to store the entire pulse in the medium at one time.

Pulse broadening occurs because of a bandwidth mismatch between the input pulse and the EIT spectrum. This is most easily understood in the frequency domain. The 1.9 μs

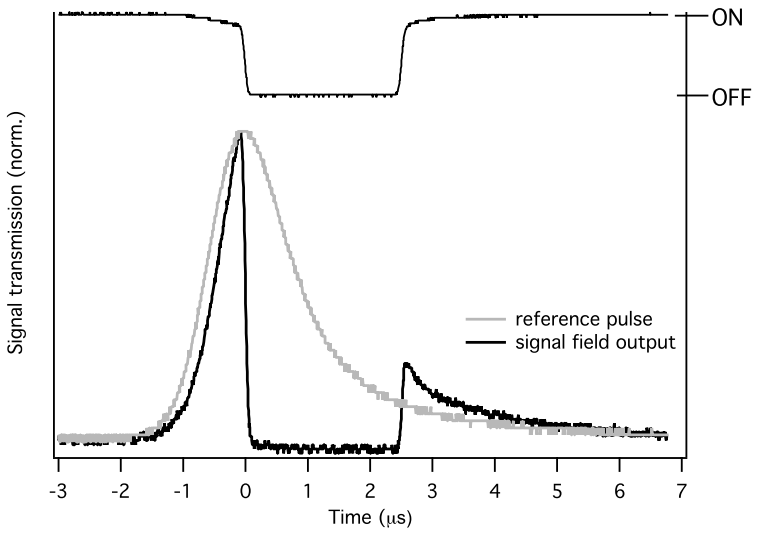

Figure 2.13: Stored light in a natural abundance Rb vacuum cell. Temperature is $T = 65$ °C. Control field output is shown at the top, where it is turned off for a $\tau = 2.5$ μs storage interval, then turned back on to retrieve the stored portion of the input pulse. Note the tails of an upside-down pulse shape in the control field, a result of the Pockels cell generating the signal field pulse at the expense of control field power.

input pulse has a frequency bandwidth of $\sim$ 160 kHz, broader than the EIT linewidth. Thus a pulse traveling through the EIT medium will have its frequency components in the tails absorbed, resulting in a narrower frequency width at the output. This corresponds to broadening in the time domain, which is what we observe.

While the slow pulse travels inside the atomic medium the control field can be turned off (using the AOM as a fast switch, as described earlier), bringing the pulse group velocity to zero. Since our slow light fractional delay is 0.32, only less than 1/3 of the pulse will be traveling in the vapor cell when it is brought to a stop. Thus most of the pulse leaks out the front of the cell, and is also seen on the signal field detector. The stored light process is illustrated in Figure 2.13 for the same input pulse shown in the slow light example of Figure 2.12. The input reference pulse is again shown, and the control and signal fields

are both shut off at the signal pulse's peak time. The shape before the time marked $t = 0$ is leaked signal field, and a section of the pulse 625 ns long is stored in the medium. The control and signal fields remain off for a $\tau = 2.5$ μs storage interval. The control field is turned back on, and the pulse is retrieved in the signal field channel. Note that the original signal field pulse has not finished forming when this occurs, so the amount of light retrieved is actually the difference between the two traces shown in Figure 2.13.

The amount of light stored in the medium is shown as the area of the reference pulse from the time $t = 0$ to $t = 625$ ns. Integrating shows that around 35% of this is retrieved in the readout pulse. The overall efficiency (defined as the output pulse area divided by the input pulse area) is in fact substantially lower because, as noted in the slow light discussion, the pulse is absorbed due to imperfect EIT transmission, and because most of the remaining pulse after absorption is not stored.

A method of improving slow light delay or stored light efficiency is to increase the atom-light interaction by raising the optical depth of the system. Stored light experiments were performed in the Rb vacuum cell at temperatures $T = 65, 68, 72, \text{and } 75$ °C, which correspond to number densities between 1.0 and 2.3×10^{11} cm^{-3}. Pulse readout area was measured as a function of both one-photon detuning from the optical resonance and two-photon detuning from EIT resonance, to study the robustness of the stored light process to deviations from resonance.

Stored light readout as a function of laser frequency is shown in Figure 2.14, which shows that the storage efficiency falls off in a way consistent with Doppler broadening. Data for the other three temperatures (not shown) confirms this, as they all have widths near 500 MHz. The usable optical depth decreases with one-photon detuning because fewer atoms have longitudinal velocities in the tails of the Doppler distribution that are needed to place them on resonance with the input light fields.

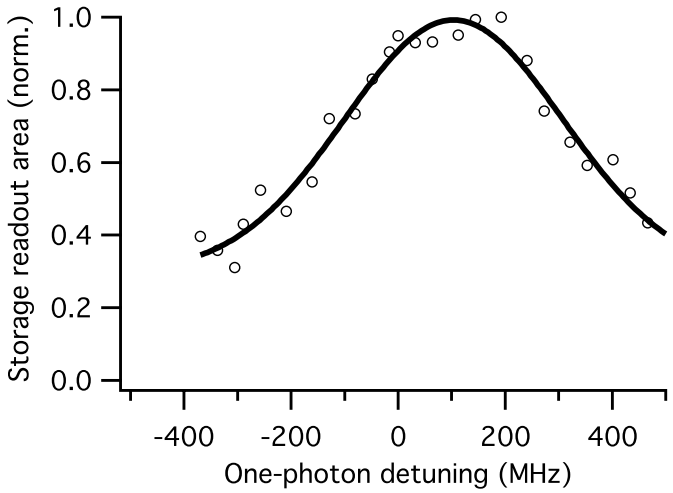

Figure 2.14: Stored light readout area (normalized to 1) vs. laser frequency (one-photon detuning) in the Rb vacuum cell. Temperature is $T = 72$ °C. The width of the feature is ~ 500 MHz, consistent with the Doppler width. Solid curve is a Gaussian fit to the data.

Stored light as a function of two-photon detuning measurements (in this case, as a function of the applied uniform magnetic field) illustrate the phase coherence of the stored light process, and add to our understanding of the role of optical depth. Figure 2.15(a) shows the readout signal field pulse varying with δ in an oscillatory manner. The oscillations are explained by interference between the output signal field and a small amount of control field light leaking into the signal field detector. With non-zero two-photon detuning δ the two ground state terms in the dark state $|D\rangle = [\Omega_c|1\rangle - \Omega_s|2\rangle]/\sqrt{\Omega_s^2 + \Omega_c^2}$ acquire a relative phase while the control field input light is off, since the applied magnetic field Zeeman shifts the ground state energy levels apart. This phase is $e^{i\delta\tau}$, with τ the storage time. During readout, the output signal light retains the accumulated phase and the signal and leaked control fields interfere. This illustrates that stored light is a phase coherent process, a topic explored in greater detail in past stored light work [23] and demonstrated in Chapter 7 for the slow light beamsplitter.

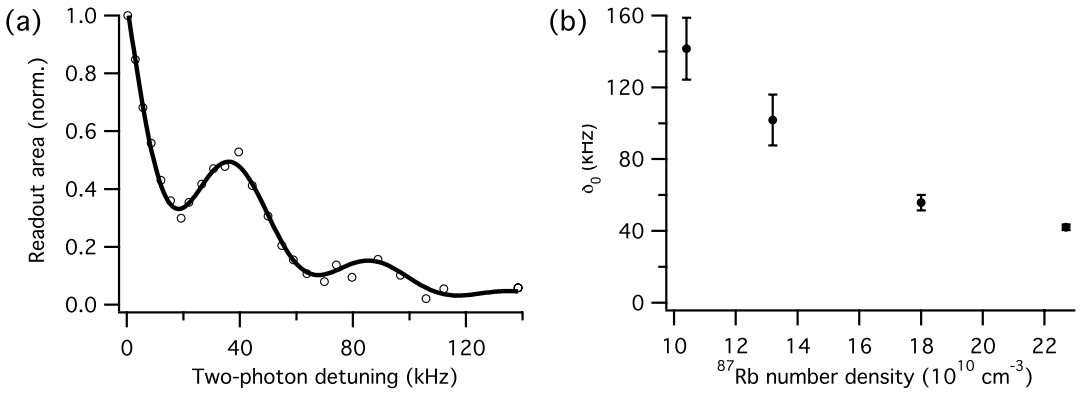

Figure 2.15: Stored light in a natural abundance Rb vacuum cell as a function of two-photon detuning. (a) Results for $T = 75$ °C, with readout area normalized to 1. The oscillations in the δ-dependence illustrate the phase coherence of stored light in vapor cells (*see text*). The solid curve is a fit to an exponentially decaying sine squared function, with δ_0 the decay constant. (b) The two-photon detuning decay constant δ_0 for four temperature settings. This shows that stored light readout area is *less* robust to two-photon detuning deviations at higher optical depth, contrary to ideas in some theoretical work [44].

An analysis of how quickly stored light readout area deteriorates with two-photon detuning from the EIT resonance reveals that high temperature systems are in fact *more* sensitive to changes in δ. Signal field readout vs. δ plots for all four temperatures were fit to functions of the form $e^{-\delta/\delta_0}[y_0 + \sin^2(\omega\delta + \phi)]$, and two-photon decay constants δ_0 were extracted, then plotted in Figure 2.15(b). The falling off of δ_0 with atomic density can perhaps be explained by the narrower EIT lineshapes found at higher density (*i.e.*, density narrowing [45]). Slow light delay does increase with more atoms present, but at the cost of greater absorption of the signal field, in this case leading to reduced readout of the retrieved signal field pulse.

Apart from demonstrating the measurement process in our apparatus and defining the quantities measured in slow and stored light experiments, these Rb vacuum cell results illustrate the need for understanding of the role of Rb density in vapor cell systems. In-

creasing the number of Rb atoms in the cell can lead to better light-atom coupling, but can introduce many other effects, such as density narrowing of the EIT lineshape, spin exchange during Rb-Rb collisions, and radiation trapping. From the limited slow light delay and low readout pulse efficiency seen in this section, clearly an important property of EIT systems is the contrast level. Long delay times are not as useful when most of the input pulse is absorbed, and absorption of the input pulse can drastically reduce readout efficiency. Finally, the short time scale limitation of vacuum cells points toward the need to extend coherence lifetimes to improve slow and stored light behavior. Buffer gas atoms can extend the time atoms spend confined to the laser beam volume, and cells with coated walls allow atoms to leave the beam and return with coherence intact. Buffer gas cells are employed in the work in Chapters 3 and 4, while paraffin-coated cells are used in Chapters 5, 6, and 7.

In the next chapter we quantify the role of EIT contrast and develop a useful tool for predicting slow light behavior from simple EIT width and contrast measurements, while at the same time exploring optical depth effects in buffer gas vapor cells.

Chapter 3

Slow Light from EIT

3.1 Introduction and motivation

In the preceding chapter we studied EIT, slow, and stored light in a Rb vacuum cell. Results pointed toward the need to better understand the role of optical depth in EIT systems, and the role that EIT contrast plays in determining slow and stored light behavior. In this chapter we both measure and model the effect that input control and signal fields have on the effective optical depth of an EIT system, and derive and test a method of predicting slow light behavior.

We show how slow light pulse delays in real EIT media can be determined directly from static transmission spectra. Using only the measured EIT linewidth and off-resonant transmission, the absolute delay of a slow light pulse in an optically thick, power-broadened medium can be simply and accurately determined, while capturing more complex optical pumping behavior.

Slow light from electromagnetically induced transparency (EIT) has many potential applications, including photonic delay lines [46], interferometry [47, 48], quantum memories [3], and atomic spectroscopy [49]. These applications benefit from long pulse delay

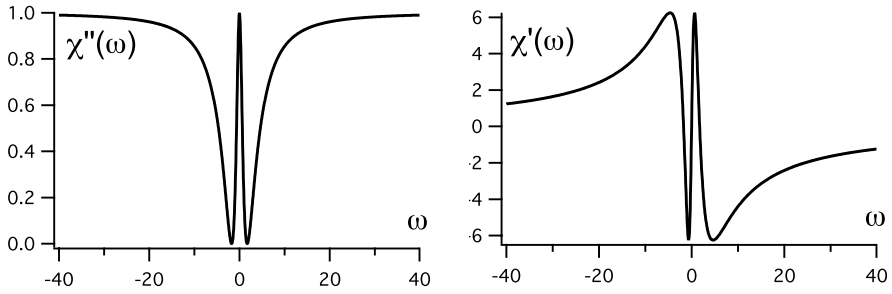

Figure 3.1: An example of using the Kramers-Kronig relations to obtain dispersion from an absorption spectrum. The imaginary part of susceptibility was chosen to be $\chi'' = 2/(\omega^2+1) - 18/(\omega^2+9)$, and the real part of susceptibility obtained is $\chi' = [4\omega(\omega^2-3)]/[\omega^4+10\omega^2+9]$. The function was chosen for illustration purposes and to qualitatively resemble a signal field absorption spectrum (EIT) as a function of two-photon detuning. Real physical spectra do not have such analytic solutions and other approaches are required.

times, which arise from a reduced group velocity associated with steep dispersion from an atomic [3, 16, 18, 1, 24, 50] or optical [51, 52, 53, 54, 55, 56] resonance.

Characterization of slow light for a particular medium often begins with the underlying static absorption resonance (*e.g.*, refs. [3, 18, 50, 51, 57]). The transfer function for any input pulse sent into a medium can be derived from the absorption and dispersion spectra, the former determining pulse absorption and broadening and the latter the time delay. The Kramers-Kronig relations do provide a direct connection between absorption and dispersion,

$$\chi'(\omega) = \frac{1}{\pi}\text{P.V.}\int_{-\infty}^{+\infty}\frac{\chi''(\omega)}{\omega'-\omega}d\omega', \tag{3.1}$$

where $\chi'(\omega)$ and $\chi''(\omega)$ are the real and imaginary parts of the dielectric susceptibility (dispersion and absorption). A simplified example of this is shown in Figure 3.1. However, extracting dispersive slow light behavior from the associated absorption resonance using the Kramers-Kronig relations in real physical systems is often difficult. They can be solved analytically only for a very limited range of absorption functions, and numerical solutions often

diverge [58]. In particular, integrals over absorption functions without complete absorption off two-photon resonance, true of any physical system, will not converge. Further, each value of the refractive index depends on the entire absorption spectrum; it is not always possible in practice to observe the full spectrum, as the one-photon absorption width is typically much broader than the EIT linewidth and very large sweeps can be difficult to manage experimentally.

We set out to find a practical way to infer dispersive (slow light) behavior from the more easily measured static transmission spectra (EIT). Other work [29] has taken a phenomenological Lorentzian absorption spectrum and calculated the resulting group velocity reduction. Here, we show that a simple, realistic model of EIT spectra allows accurate prediction of slow light pulse delay from two easily-measurable parameters: the linewidth and off-resonant transmission level on a logarithmic scale. We find good agreement between the predictions of this model and experimental measurements of EIT and slow light in warm Rb vapor. This technique should be applicable to a wide range of slow light media.

3.2 Derivation of the slow light from EIT prediction

As discussed in Chapter 1, EIT is a two-optical-field phenomenon in which a strong control field renders an otherwise absorbing medium transparent to a weak signal field via quantum intereference between two alternate excitation paths from the ground to excited state [11]. Both static line shapes [36] and dynamic behavior [19, 20] may be straightforwardly calculated. Here, we extract model parameters from the three-level-atom absorption resonance and determine the group velocity and effective optical depth, which together determine the absolute pulse delay.

We calculate steady-state signal absorption in EIT from the imaginary component

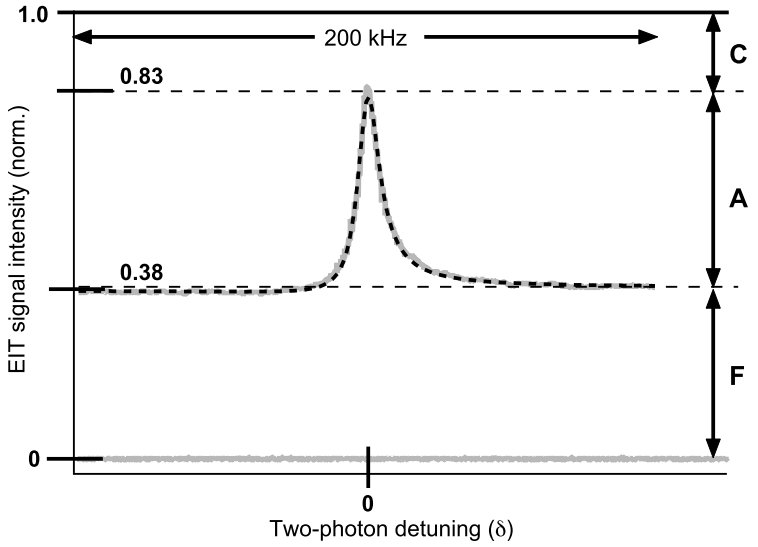

Figure 3.2: Typical buffer gas EIT intensity spectrum with normalized contrast and background levels. Solid gray line is the data while the dashed dark line is a fit to a skew-Lorentzian. **0**: background and control field leakage into signal channel in absence of signal input. **F**: signal intensity above background away from EIT resonance (the "floor"); **A**: amplitude of EIT peak; **C**: difference between EIT peak and 100% transmission (the "ceiling"). Parameters are normalized so that $\mathbf{F} + \mathbf{A} + \mathbf{C} = 1$. (For data shown here, $T = 40\,^{\circ}\mathrm{C}$, in a 25 torr N_2 buffer gas cell, and the total laser power $\approx 490\ \mu$W.)

of the susceptibility. For a three-level Λ-system, the susceptibility as a function of two-photon Raman detuning, δ, is [36]:

$$\chi''(\delta) = \frac{n\wp\omega}{2\hbar\epsilon_0} \frac{\delta^2(\gamma+\gamma_0) - \gamma_0(\delta^2 - \gamma\gamma_0 - \Omega_c^2)}{(\delta^2 - \gamma\gamma_0 - \Omega_c^2)^2 + \delta^2(\gamma+\gamma_0)^2}, \tag{3.2}$$

where n is the atomic density, $\wp$ and ω are the dipole matrix element and frequency between the ground and excited states, γ is the excited state decay rate, γ_0 is the ground state decoherence rate, and Ω_c is the control field Rabi frequency. The factor in front can also be written as g^2N, with g the one-photon Rabi frequency (atom-photon coupling constant) and N the number of atoms. We characterize our EIT resonance by its linewidth, amplitude A, off-resonant floor F, and ceiling C (see Fig. 3.2). These F, A, and C parameters define EIT contrast, and are normalized such that $F + A + C = 1$, where 1 would be the signal

field transmission with no absorption. The normalized off-resonant transmission, F, is

$$F = [e^{-\chi''_{max.}L/c}]^2 = e^{-2d_0}, \tag{3.3}$$

where L is the length of the medium, c is the vacuum speed of light, and d_0 is defined as the system's optical depth. $\chi''_{\max}$, determined from Eq. 3.2, is the absorption away from EIT resonance. The delay of a slow light pulse is proportional to the product of the optical depth and the slope of the medium's dispersion curve. Based on a first-principles dark-state polariton model of propagation in a three-level EIT medium, the maximum delay τ_{max} for a pulse with bandwidth much smaller than the width of the EIT resonance is given by [19, 20]:

$$\tau_{max} = \frac{nL\wp\omega}{2\hbar\epsilon_0\Omega_c^2 c} = \frac{d_0\gamma}{\Omega_c^2}. \tag{3.4}$$

In an optically thin medium, Ω_c^2/γ equals the EIT transmission half-width half-maximum (HWHM), provided that the control field has both a uniform transverse profile [43] and intensity such that in combination with the given buffer gas pressure and beam size, reshaping by Ramsey narrowing is not present [59, 60]. To generalize to optically thick media, we set Ω_c^2/γ to equal the HWHM of the logarithm of the EIT transmission spectrum, assuming the medium to be power-broadened throughout [20]. The maximum delay for an optically thick medium is then

$$\tau_{max} = \frac{-\ln(F)}{\mathrm{FWHM}[\ln(\mathrm{EIT})]}, \tag{3.5}$$

where F is defined above and $\mathrm{FWHM}\,[\ln(\mathrm{EIT})]$ is the full width of the logarithm of the measured EIT transmission spectrum. Even with significant control field depletion, which is often found in systems with large optical depths, Eq. 3.5 still holds, provided that the EIT lineshape is power-broadened. A more detailed treatment of this can be found in [61].

The EIT amplitude, A, determines the fidelity of pulse transmission, but is not directly needed for extracting the pulse delay for narrow bandwidth pulses. The easily-

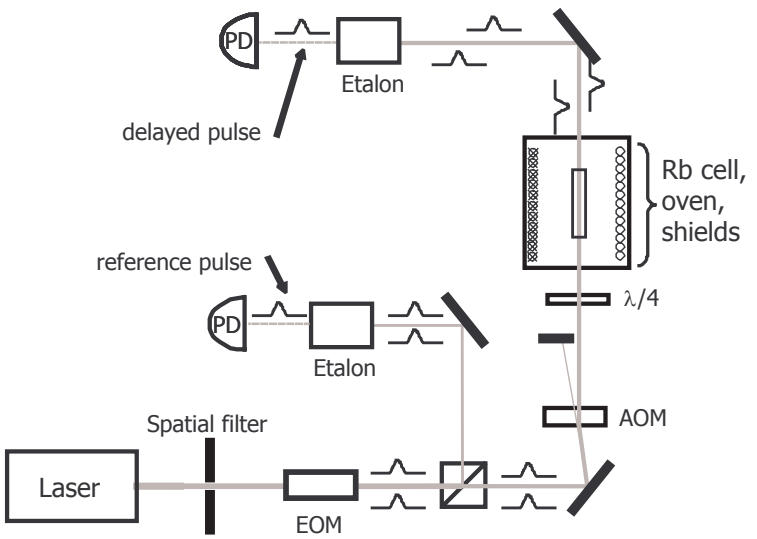

Figure 3.3: Schematic of the apparatus used for EIT and slow light measurements described in this chapter. An electro-optic modulator (EOM) frequency modulates the laser light to generate signal and reference field sidebands (shown as traveling pulses), while an acousto-optic modulator (AOM) regulates the light intensity. Reference and output signal fields are sent into photodetectors (PD) for EIT line shape and slow light delay measurements.

measureable off-resonant transmission, F, serves as a proxy for the optical depth which can be a function of system parameters as discussed below.

3.3 Experimental setup

We tested the efficacy of this simple technique for determining slow light delay using measured hyperfine EIT resonances in warm Rb vapor. For an example spectrum, see Figure 3.2. A schematic of our experimental apparatus appears in Fig. 3.3, a specific implementation of Figure 2.1 using the hyperfine EIT configuration with etalon filtering. An amplified diode laser produced light at 795 nm, which after spatial filtering passed through an EOM driven at 6.835 GHz, the Rb ground state hyperfine transition frequency, producing sidebands with 4% of the carrier (control field) intensity. The +1 sideband served

as the signal field, while the -1 sideband was far off resonance and served as a transmission reference. Adjusting the EOM frequency changed the two-photon detuning, δ. The laser field was circularly polarized with a quarter-wave plate ($\lambda/4$), then expanded and shaped with a telescope and iris to create a flat-top transverse beam profile with diameter 3.5 mm.

The laser beam then passed through a Rb vapor cell of length $L = 15$ cm and diameter $D = 1.2$ cm containing isotopically enriched ^{87}Rb and 25 torr of N_2 buffer gas to confine the Rb atoms. The atypical geometry of this high-aspect-ratio cell is used to minimize coherence loss due to radiation trapping; this is not directly relevant to the predictions measured here, and is discussed more completely in Chapter 4. The cell was housed inside a blown-air oven and high-permeability magnetic shields, and heated above 40 °C, corresponding to an unpolarized optical depth of $d_0 \approx 2$. The output light was filtered using a temperature-stabilized etalon tuned to transmit only the signal light. A small amount of the input signal light, separated from the main beam with a beam splitter and measured through a second stabilized etalon, served as a reference for slow light time delay measurements.

We obtained EIT spectra by measuring the output signal power while sweeping the two-photon detuning δ across the hyperfine resonance. Similarly, we performed slow light measurements at $\delta = 0$ by varying the EOM drive power to shape a pulse of input signal light. We defined the slow light delay as the difference in peak arrival times between the reference and output signal pulses.

The requirement of Lorentzian EIT lineshapes for quantitative slow light predictions dictated the elimination of extra EIT features arising from intensity gradients across the transverse beam profile. Creating a flat-top beam profile minimized reshaping of the EIT resonance from an otherwise Gaussian transverse profile [43, 62]. An example of the flat-top beam's effectiveness is shown in Figure 3.4. The EIT lineshape with a Gaussian beam at high intensity acquires a sharp, narrow feature at the center resonance. With such

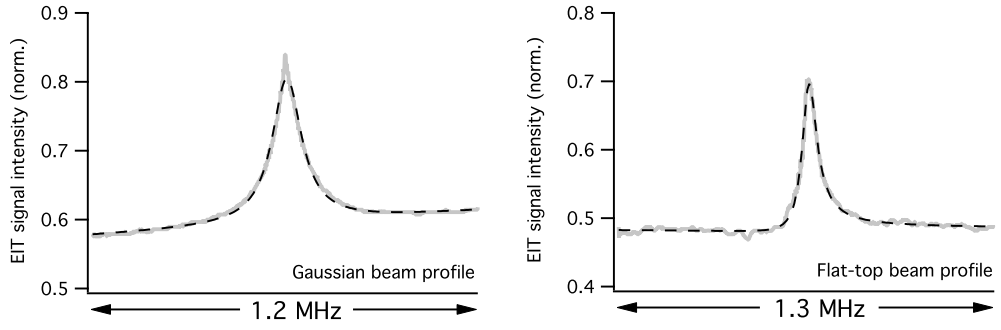

Figure 3.4: EIT lineshapes for a both a Gaussian and flat-top beam profile. $T =$ 40 °C, with a $d = 3.5$ mm beam at 5 mW for the Gaussian beam and 4.5 mW for the flat-top beam. Dashed curves are skew Lorentzian fits. The sharp central feature due to transverse intensity gradients in the beam profile is eliminated when using a flat-top beam shape.

a nonuniform profile, atoms moving through the beam cross section see different intensities along their paths; the final EIT lineshape observed is an integrated result of Lorentzian lineshapes with different power-broadened widths [43]. Switching to the flat-top beam profile results in EIT that clearly fits better to a Lorentzian shape. The cell temperature, beam diameter, and laser power are all the same, but the flat-top profile's EIT is narrower, with different contrast levels. This is because peak intensity is much less, resulting in a less power-broadened line shape, and less effective optical depth reduction (see below).

3.4 EIT contrast and trapped state modeling

Measurements of the EIT floor and amplitude are summarized in Fig. 3.5. The normalized signal transmission level $(F + A)$ increases with laser power, as more atoms are optically pumped into the non-absorbing, dark state [19]. The measured EIT linewidth (not shown) conforms well to the expected linear power broadening: $\gamma_{EIT} \propto \Omega_c^2/\gamma$.

The increase in signal transmission saturates at high power, whereas the off-

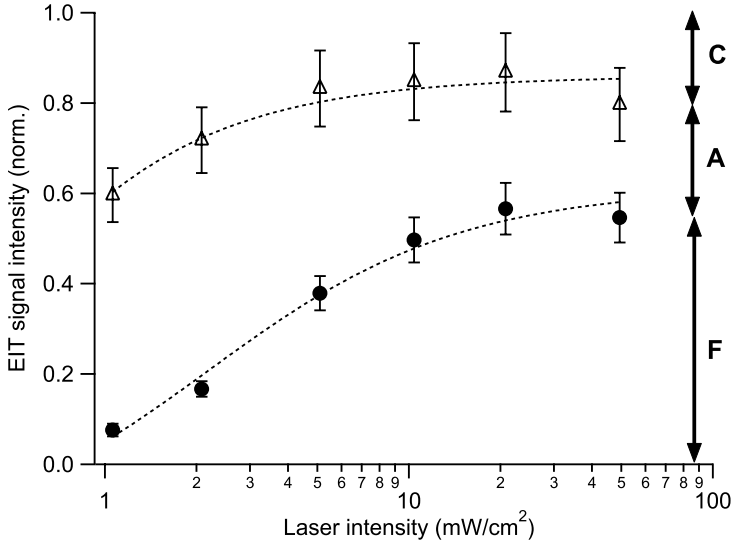

Figure 3.5: Measured EIT floor (**F**, circles) and peak transmission (**F** + **A**, triangles) level vs. total laser intensity for experimental conditions described in the text. Uncertainties in the measured contrasts in this figure are predominantly systematic. Dotted curves are fits of a 4-level model to the data with good agreement between fit parameters and experimental conditions.

resonant transmission level F increases, corresponding to reduced slow light delay (see Eq. 3.5). We attribute this increased F to optical pumping into inaccessible "trapped" states at a rate dependent on buffer gas species and pressure, as well as laser field intensity and polarization. For example, for σ^+-polarized light, atoms pumped into the $|F, m_F\rangle = |2, 2\rangle$ state no longer participate in EIT (recall Figure 2.9). Thus, the *effective* optical depth decreases with increasing control field power. These complex optical pumping processes were not included in the original three-level model used to write our predictive equation 3.5, but are encapsulated in the measured floor value F, illustrating the usefulness of this approach. We also find good agreement between our measured EIT contrast levels and a simple 4-level model that includes the extra "trapped" level in the ground state [41].

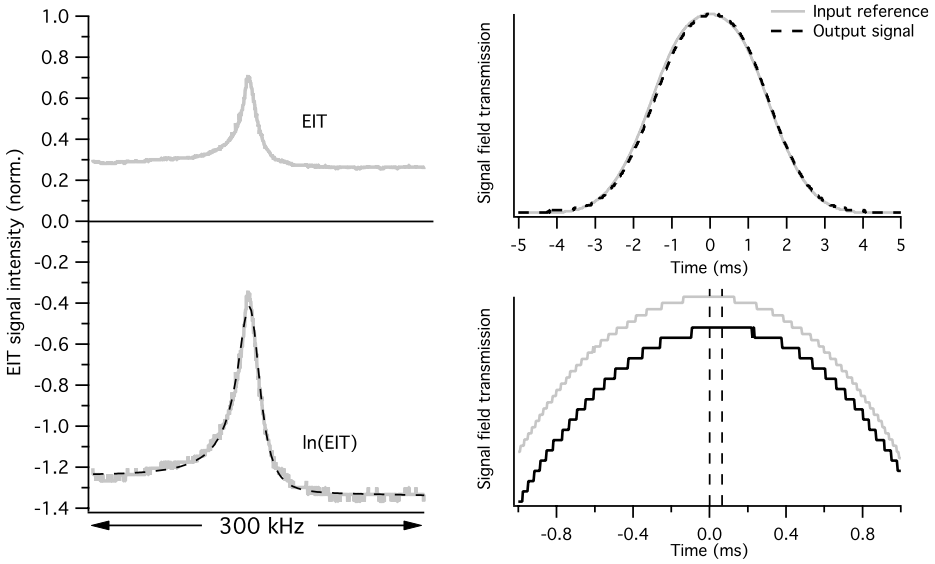

Figure 3.6: Slow light from EIT demonstrated for a particular EIT lineshape. The measured EIT and its natural logarithm appear on the left, and slow light for a narrow-bandwidth input pulse is shown on the right, including a zoomed in view of the pulse peaks to demonstrate the pulse delay precision necessary for the measurement (pulses are offset in the figure for clarity).

3.5 Predicted and measured slow light delays

We found quantitative agreement between directly measured slow-light pulse delays and predictions by the above method using measured EIT lineshapes, over a large range of pulse delays and laser intensities. Narrow-bandwidth pulses were employed, such that the pulse bandwidth was always small compared to the EIT bandwidth. An example of the method working for a particular EIT line shape is shown in Figure 3.6. For a $T = 50$ °C cell temperature, with 1.1 mW of laser power, the EIT lineshape was measured, with a 19 kHz linewidth and contrast parameters of $F = 0.28$, $A = 0.43$, and $C = 0.29$. The natural logarithm (of the normalized EIT) is also shown, as it is preferable to work in the logarithmic domain when extracting slow light delay predictions; the width of $\ln(EIT)$ is 25 kHz and $\ln F = -1.3$. Using Eq. 3.5, the predicted maximum delay is $\tau_{max} = 50 \pm 5$ μs.

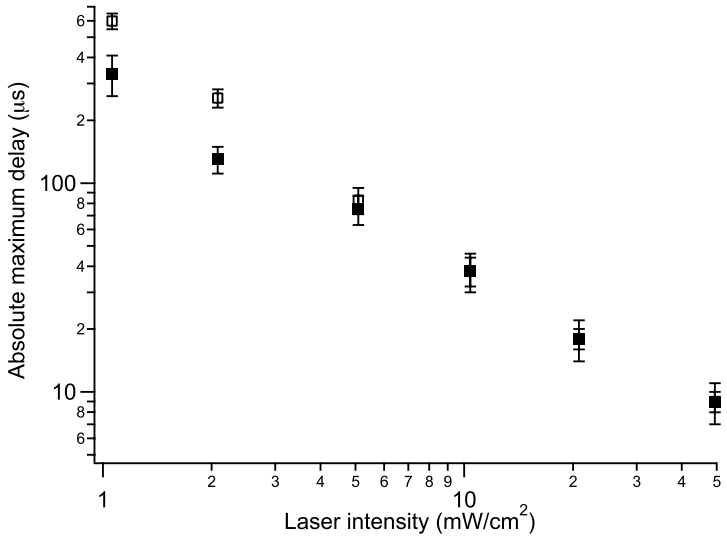

Figure 3.7: Measured slow-light delays (solid squares) and predictions (hollow squares) based on accessible EIT lineshape parameters at a cell temperature of $T = 40$ °C. Good agreement is shown over a large range of pulse delays and laser intensities.

A signal field slow light pulse of width 3.8 ms was sent into the cell, its ~ 80 Hz bandwidth easily allowing it to fully fit within the EIT spectrum; thus the entire pulse should experience the steepest dispersion slope and be maximally slowed. The measured absolute delay was 46 μs, in agreement with the prediction above. Note the small fractional pulse delay of $\sim 1\%$, as measurement uncertainty occurs due to the line splitting.

Measured pulse delays and their static EIT-based predictions agreed over a large range of laser powers and delay times at $T = 40$ °C (Figure 3.7). We found discrepancies between prediction and observation at only the lowest laser intensities, where the approximation of power-broadened EIT began to break down. More detailed modeling improved the agreement at low powers, but at the expense of the simple expressions of Eqs. 3.4 and 3.5 above [63].

Error bars in Figsures 3.5 and 3.7 were derived from the uncertainty in fit parame-

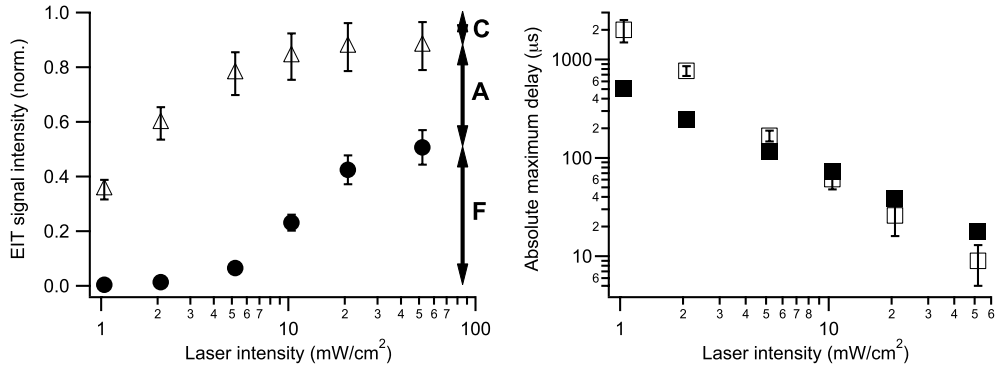

Figure 3.8: EIT contrast measurements, and predicted and measured absolute maximum slow light delays at $T = 50$ °C. Predictions work less well at higher temperatures.

ters for slow light pulse delays and EIT contrast as well as systematic errors associated with laser power and etalon drift (leading to 5% overall uncertainty in maximum signal transmission). Systematic uncertainty dominated over statistical uncertainty in our EIT contrast data. Residual uncertainty due to nonuniform transverse beam profiles and Ramsey narrowing [59, 60] was small.

Our predictive method works less well at higher cell temperature. EIT contrast and predicted and measured pulse delays for $T = 50$ °C are shown in Figure **??**. Qualitatively, the differences in EIT contrast and delays compared to the $T = 40$ °C are understandable: the floor F does not rise as rapidly at this higher temperature, since it is a measure of the optical depth, and the absolute maximum delays are larger at all laser intensities due to the greater amount of light-atom interaction. However, the slow light from EIT predictions are less accurate under these circumstances. Further investigation is needed to draw more reliable conclusions.

3.6 Slow light figure of merit

The slow light from EIT derived in Section 3.2 and given in Eq. 3.5 predicts the maximum absolute pulse delay, a convenient value to measure and an important piece of information in characterizing the slow light properties of a system. However, most applications of slow light do not operate in this regime of input pulse bandwidths being much smaller than the EIT bandwidth. As seen in Figure 3.6, this leads to extremely small fractional delays, meaning the peak separation between reference and delayed pulses are less than the pulse width, and the entire pulse is not trapped in the medium for stored light experiments, and the delay line criteria of full pulse separation is not met for optical communication applications. Further, the maximum delay depends on the EIT linewidth, which in itself does not make for better pulse separation, it merely dictates the bandwidth of pulses to use. In this section we argue for a different slow light figure of merit and show that it can be derived from static EIT measurements under assumptions about symmetric Lorentzian lineshapes and power-broadened EIT, similar to those used earlier in the chapter.

Starting with a symmetric (and normalized) Lorentzian function, with amplitude A and offset F,

$$L(\nu) = F + \frac{A(\gamma/2)^2}{(\nu-\nu_0)^2 + (\gamma/2)^2}, \tag{3.6}$$

its FWHM is γ. However, for the natural logarithm of the function,

$$\ln\left[L(\nu)\right] = \ln F + \frac{A(\gamma/2)^2}{(\nu-\nu_0)^2 + (\gamma/2)^2}, \tag{3.7}$$

the width turns out to be $((F+A)/F)^{1/4}\gamma$. This means we can rewrite our slow light from EIT prediction, Eq. 3.5, as

$$\tau_{max} = -\left(\frac{F}{F+A}\right)^{1/4} \frac{\ln F}{\gamma_{EIT}}, \tag{3.8}$$

where γ_{EIT} is the EIT line width (FWHM) in the linear scale. This allows one to predict

the maximum slow light delay without explicitly taking the logarithm of the normalized EIT line shape.

Next we make the approximation that the absolute maximum pulse delay is the absolute delay for any input pulse width. This is not strictly true, since frequency components of a pulse away from the EIT peak will experience shallower dispersion slopes. However, these components are also absorbed more, having less of an effect on the final observed pulse. Also, an "optimized" slow light pulse (which combines large fractional delay with high transmission) will not have a bandwidth larger than the EIT lineshape, as most would be absorbed. Experimental measurements of fractional pulse delay over three orders of magnitude of input pulse widths confirm that the fractional delay scales inversely with the input pulse width; *i.e.*, that the absolute delay varies little with the input pulse width.

A suitable figure of merit for slow light should include both group velocity delay and transmission. We can find the transmission for an arbitrary Gaussian input pulse traveling in a medium with Lorentzian EIT. For a Gaussian pulse whose amplitude in the time domain is $G(t)$ with a FWHM T, its frequency domain equivalent is

$$\hat{G}(\nu) \propto \exp\left[-\frac{\pi^2 T^2 \nu^2}{4\ln 2}\right], \tag{3.9}$$

and since the normalized EIT line shape gives transmission, the output pulse in the frequency domain will be $\hat{G}(\nu)L(\nu)$, where $L(\nu)$ was given in Eq. 3.6. To find the fractional transmission, we take the ratio of the output pulse area to the input pulse area, staying in the frequency domain:

$$\text{Trans.} = \frac{\int_{-\infty}^{+\infty} \hat{G}(\nu)L(\nu)d\nu}{\int_{-\infty}^{+\infty} \hat{G}(\nu)d\nu} = \frac{\frac{2F}{T}\sqrt{\frac{\ln 2}{\pi}} + + \frac{\pi}{2}A\gamma\left[\text{erfc}\left(\frac{\pi\gamma T}{4\sqrt{\ln 2}}\right)\right]\exp\left(\frac{\pi^2\gamma^2T^2}{16\ln 2}\right)}{\frac{2}{T}\sqrt{\frac{\ln 2}{\pi}}}. \tag{3.10}$$

This expression can be simplified to

$$\text{Trans.} = F + A\sqrt{\pi}x\left[\text{erfc}(x)\right]e^{x^2}, \text{where } x \equiv \frac{\pi\gamma T}{4\sqrt{\ln 2}}. \tag{3.11}$$

This transmission function depends on EIT contrast parameters and on the quantity γT, the product of the EIT linewidth and the input Gaussian temporal pulse width. Using our assumption that absolute pulse delay is constant, we can write γT in terms of contrast levels also. By definition, slow light fractional delay is $f \equiv \tau/T$, with τ the absolute pulse delay. If our assumption $\tau = \tau_{max}$ holds true, this, combined with Eq. 3.8, yields

$$f = \frac{\tau_{max}}{T} = -\left(\frac{F}{F+A}\right)^{1/4} \frac{\ln F}{\gamma T} \rightarrow \gamma T = -\left(\frac{F}{F+A}\right)^{1/4} \frac{\ln F}{f} \tag{3.12}$$

We now have a predicted pulse transmission entirely in terms of EIT contrast parameters and fractional pulse delay f, by substituting this result in for γT in the expression for x in Eq. 3.11. A final correction we want to make to the transmission expression is to remove the F term. Physically this says we are only interested in transmission of light that is slowed by traveling through the EIT resonance, not transmission due to lack of optical depth. For example, an EIT lineshape with a large off-resonant floor F and small amplitude A has weak light-atom coupling and would support only small slow light delay. With this change, we obtain a slow light figure of merit, the slow light quality

$$q_{slow} = A\sqrt{\pi}x\left[\mathrm{erfc}(x)\right]e^{x^2}, \text{where } x \equiv -\frac{\pi}{4\sqrt{\ln 2}}\left(\frac{F}{F+A}\right)^{1/4}\frac{\ln F}{f}. \tag{3.13}$$

Physically the quantity q_{slow} predicts the transmission of a slowed pulse through an EIT medium, where the pulse bandwidth has been chosen to give the fractional delay f. The prediction requires only the off-resonant floor F and the peak EIT transmission $F + A$, obtained straightforwardly from an EIT lineshape measurement in the linear scale. The equation could be used to find EIT settings that meet the delay line criteria (needing $q_{slow} \geq 0.5$ for $f = 1$). This will be used in the coated cell work in Chapter 6 in the search for optimal slow and stored light conditions in vapor cells.

In this chapter we have presented a straightforward model of EIT in optically thick, power-broadened media that provides both a quantitative prediction of the slow-

light delay and a measure of the effective system optical depth from easily derived static properties of the EIT lineshape. We find good agreement between the EIT spectrum-based predictions and measured slow-light delay, and the approach captures more complicated optical pumping behavior present in many-level atomic systems. Slow light with large delay and high efficiency is obtained for small floor F and large amplitude A; hence static EIT lineshape measurements may be used to optimize slow light. These techniques should be applicable in other slow light systems in which static resonance lineshapes can be easily extracted.

Chapter 4

Slow and Stored Light and Optical Depth

4.1 Introduction

With our greater understanding of the relationship between slow light and EIT, we move on to optimizing the stored light process in buffer-gas-filled Rb vapor cells, in particular characterizing the benefits and limitations of working with high-optical-depth systems. In Chapter 2 we saw how increasing optical depth made the stored light efficiency in an EIT system more sensitive to deviations from two-photon resonance, contrary to expectations that failed to take into account the larger absorption that accompanies stronger light-atom coupling. In Chapter 3 we noted that the effective optical depth of a system does not necessarily scale with the actual atomic density, but was strongly dependent on optical pumping mechanisms from the input light fields interacting with real 16-level atoms.

In the present chapter we present an experimental study of the dependence on optical depth of slow and stored light pulses in Rb vapor. In particular, we characterize the

efficiency of slow and stored light as a function of Rb density; pulse duration, delay and storage time; and control field intensity. We then investigate and characterize ways to mitigate radiation trapping, an incoherent pumping mechanism that becomes important at high atomic density; this includes using nitrogen as a buffer gas to quench the excited state, and using cells with different geometries to reduce the transverse optical depth. Experimental results are in good qualitative agreement with theoretical predictions.

Applications of EIT-based slow and stored light, in both quantum information processing and optical communication, will benefit from improved efficiency and delay-bandwidth product. Proof-of-principle experiments in both cold and warm atomic systems have successfully demonstrated reversible storage of photon states [4, 6, 5], single-photon EIT [7], and in quantum repeaters aimed to increase the efficiency of long distance quantum communication [2, 9, 8, 10]. However, practical applications will require significant improvements in the efficiency of writing, storing, and retrieving an input photon state beyond values achieved to date [64, 65, 66, 67]; high efficiency and large delay-bandwidth products have not been fully realized in all-optical systems. Here we seek to optimize semiclassical stored light in vapor cells, and probe their limitations as candidates for quantum information and optical communication work.

As described in Chapter 1, a weak signal pulse will propagate with very slow group velocity through an otherwise absorbing medium [16], which is established by a strong control field under conditions of EIT. The reduced group velocity is the result of the transfer of photonic excitation in the pulse to the collective spin coherence of the atoms. The group velocity is proportional to the control field intensity, and can be reduced to zero by shutting off the control light. In this case the photonic information of the pulse is completely transferred to the atoms. This coherent transfer is reversible, and thus after some storage time the pulse may be retrieved, converting it back into photonic excitation when the control

light is turned back on.

To optimize slow and stored light will require reducing the absorption of signal field light and spin decoherence, as well as increasing optical depth to achieve a large delay-bandwidth product [3]. In vapor cells, signal light absorption is typically caused by incomplete polarization of the atomic medium due to such mechanisms as radiation trapping Atomic decoherence arises from mechanisms such as collisions with buffer gas atoms and cell walls, diffusion out of the laser beam, and residual magnetic field gradients. And as seen in Chapter 3, the effective system optical depth (and thus pulse delay) can decrease when attempting to optimize with respect to input laser light power.

A simple three-level stationary atom treatment finds that slow and stored light properties improve with increasing atomic density or optical depth. The EIT bandwidth, γ_{EIT}, for moderate to large optical depths is found to be [14, 20]

$$\gamma_{EIT} = \frac{|\Omega_c|^2}{\sqrt{\gamma g^2 N L/c}} = \frac{|\Omega_c|^2}{\gamma\sqrt{d_0}}, \tag{4.1}$$

where Ω_c is the Rabi frequency of the control field, γ the excited-state line width, N the total number of three-level atoms, L the length of the medium (the optical depth, $d_0 = g^2 N L/\gamma c$), g the light-atom coupling coefficient, and c the speed of light. The corresponding group velocity for a slow light signal pulse is [14, 20]

$$v_g = \frac{c}{1 + g^2 N/|\Omega_c|^2} \approx \frac{c|\Omega_c|^2}{g^2 N} = \frac{L|\Omega_c|^2}{\gamma d_0}. \tag{4.2}$$

The absolute pulse delay, ΔT_{abs}, is then given by the length of the medium divided by the group velocity and we find that $\Delta T_{\text{abs}} \propto d_0$: time delay is proportional to the optical depth.

A careful, three-level atom, theoretical study of storage efficiency η (defined as the ratio of the number of output photons to the number of input photons), optimized for a given optical depth [68, 69], finds that the optimal temporal pulse width $T_{opt} \sim d_0$, and

finds that η scales as $1 - 19/d_0$ at high optical depth, and increases more rapidly at lower d_0. This treatment implies continued efficiency improvement with increasing optical depth.

In practice, our experiments find that slow and stored light efficiency improve with increasing optical depth for modest optical depths. However, at higher optical depths, efficiency reaches a maximum and then degrades. Measuring coherence loss rates (due to the various decoherence mechanisms introduced in Section 1.5) and including them in the efficiency optimization model does yield good agreement between theory and experiment as η falls off with increasing optical depth. We also report promising storage efficiency results for a new cell geometry designed to reduce coherence loss due these decoherence mechanisms, particularly radiation trapping, which we characterize and mitigate using different buffer gas and cell geometry.

4.2 Experimental setup

As in the preceding chatpers, we measured EIT and slow and stored light, using the D_1 transition in a warm ^{87}Rb vapor, here using the hyperfine EIT configuration (Figure 2.9). Measurements were made using either the beat note detection method (Figure 4.1) or the temperature-stabilized etalon detection method used in Chapter 3 (Figure 3.3).

The input optical fields were generated by the laser, then phase modulated by an EOM at the ground state hyperfine splitting ($\sim$ 6.835 GHz); the +1 sideband acted as the signal field, with a maximum signal to control intensity ratio of 2.5%; the sideband amplitude was varied to shape the desired signal pulse. The frequency could be varied to change the two-photon detuning δ of the EIT transition for measuring its line shape.

The output fields, in the beat note detection case, were measured by sending the laser light into an optical fiber, then into a fast photodetector (PD) along with a reference

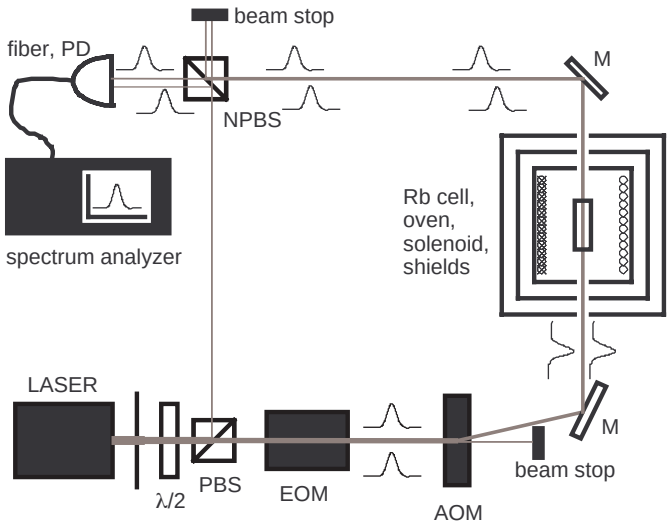

Figure 4.1: Schematic of apparatus for experiments described in this chapter. Output of laser is split with a half-wave plate ($\lambda/2$) and PBS into a reference beam and main beam; an EOM and AOM shape the signal and control fields; a fast photodetector measures the beat between the unmodulated reference beam and the output from the vapor cell.

beam picked off prior to the EOM and AOM. The control field, signal field, or the unused -1 sideband could thus be measured by beat note detection with a spectrum analyzer, at 80 MHz, 6.835 GHz + 80 MHz, and 6.835 GHz $-$80 MHz, respectively. The transmission of the -1 sideband (off EIT resonance), which is ~ 6 GHz away from any Rb resonance, was used as a reference for determining slow light delay or storage efficiency, where ΔT_{abs} was the difference between pulse peak arrival times and efficiency $\eta =$ (signal pulse area)/(-1 sideband area).

A procedure for optimizing stored light efficiency for a given d_0 and control field laser power was used throughout the measurements in this chapter. This method takes an output stored light pulse, time-reverses it, and uses the resulting shape as the new input pulse; the input pulse converges to the optimal pulse shape after a few iterations. The time-reversed pulse shape iteration scheme has been developed theoretically [68, 69] and directly

Figure 4.2: The long, narrow Rb vapor cell used in stored light optimization experiments to mitigate the effects of radiation trapping. Length is 15 cm and diameter is 1.2 cm.

implemented experimentally [70, 71]. In effect, this procedure balances the tradeoff between fractional delay (larger for high-bandwidth pulses) and transmission (peaks for narrow-bandwidth pulses) and chooses the pulse width that maximizes pulse readout efficiency.

The collimated, circularly polarized laser beam entering the Rb vapor cell had a diameter of approximately 7 mm. The cell temperature was varied between 40 and 80 °C, or atomic number density between 4×10^{10} and 100×10^{10} cm^{-3}. Four Rb vapor cells were used in our experiments; all four contained isotopically enriched ^{87}Rb and were filled with buffer gas to confine atoms and extend their coherence life times. The cell used only for indirect radiation trapping measurements had diameter $D = 2.5$ cm and length $L = 7.5$ cm, with 10 torr of Ar and 15 torr of Ne. Of the three primary cells used for slow and stored light experiments, two had had dimensions $L = 15$ cm and $D = 1.2$ cm; one was filled with 40 torr of Ne buffer gas and the other with 25 torr of N_2. The fourth cell also contained 40 torr of Ne, with dimensions $L = 7.5$ cm and $D = 2.5$ cm. The unusually long aspect ratio cells (see Figure 4.2) were used to combat the effects of radiation trapping, as described below. An example measurement of stored light is shown in Figure 4.3. These cell choices allowed us to directly investigate the role of different buffer gases (by comparing the two long cells), and the role of cell geometry (by comparing the two Ne buffer gas cells).

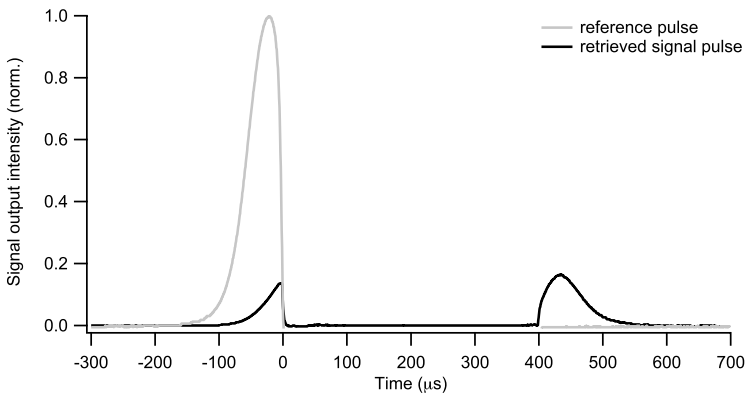

Figure 4.3: Example stored light measurement using the long, narrow vapor cell, which is filled with 40 torr of Ne buffer gas. The control field is turned off for 400 μs, and the pulse is retrieved with $\sim$ 20% efficiency. Note the shape preservation of the pulse, a benefit of spatial confinement of the Rb atoms. Efficiency (η) is the area (energy) ratio between the retrieved pulse and the reference pulse. Control field power is 23 mW/cm^2 and cell temperature is $T = 59$ °C.

4.3 Stored light scalings

We studied slow and stored light as a function of optical depth by measuring the fractional delay (delay-bandwidth product) and efficiency of optimized pulses as the vapor cell temperature was varied.

Measured EIT bandwidths and slow light delays scaled as expected with optical depth. Figure 4.4(a) shows EIT linewidth (FWHM, as extracted from a Lorentzian fit) vs. atomic density, which follows the $\gamma_{EIT} \propto 1/\sqrt{d_0}$ trending expected from Eq. 4.1. Figure 4.4(b) shows that absolute pulse delay $\Delta T_{abs} \propto d_0$; and Figure 4.4(c) shows that the optimal pulse width $T_{opt} \propto d_0$.

We measured linewidths and pulse delays at two control field powers, 3.8 mW and 8.8 mW, corresponding to intensities 10 and 23 mW/cm^2 and Rabi frequencies 6.7 and 10 MHz. Slow light delays in Figures 4.4(b) and 4.4(c) are tailored for optimized stored light, obtaining neither the maximum absolute delay (achieved for a temporally long pulse

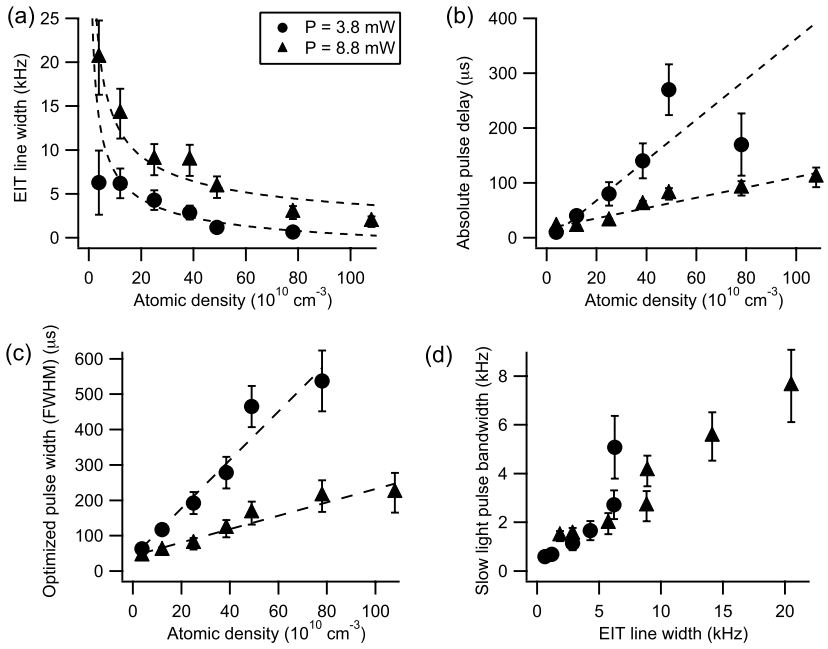

Figure 4.4: Measured EIT linewidth, slow light delay, and optimized pulse width at various optical depths and for two control field powers (3.8 mW and 8.8 mW). (a) EIT line widths are consistent with power broadening and density narrowing. (b) Absolute pulse delay (equal to the time elapsed between the peaks of the reference pulse and the slowed pulse) and (c) optimized temporal pulse widths are approximately linear in atomic density. (d) Optimized slow light bandwidth vs. EIT line width. Error bars for all measurements are derived from a systematic uncertainty in the Rb temperature of ~ 2 °C and uncertainty in the laser frequency of $\sim$ 150 MHz. Dashed lines are fits of data to the simplified three-level model described in the text.

experiencing only the steepest part of the dispersion, but having a small fraction of the pulse in the medium at one time) nor the maximum fractional delay (achieved for a temporally short pulse which suffers large absorption due to frequency components outside the EIT bandwidth). Comparing the optimized pulse bandwidth (where T_{opt} is the temporal pulse width) to the measured EIT bandwidth [Figure 4.4(d)], we find that $1/T_{opt} \sim \gamma_{EIT}/3$, over a large range of fractional delays (from 0.2 to > 1.0), a somewhat greater pulse bandwidth than predicted theoretically [20, 72], where $\gamma_{EIT}T >> 1$ or even $>> 10$. Note that based on

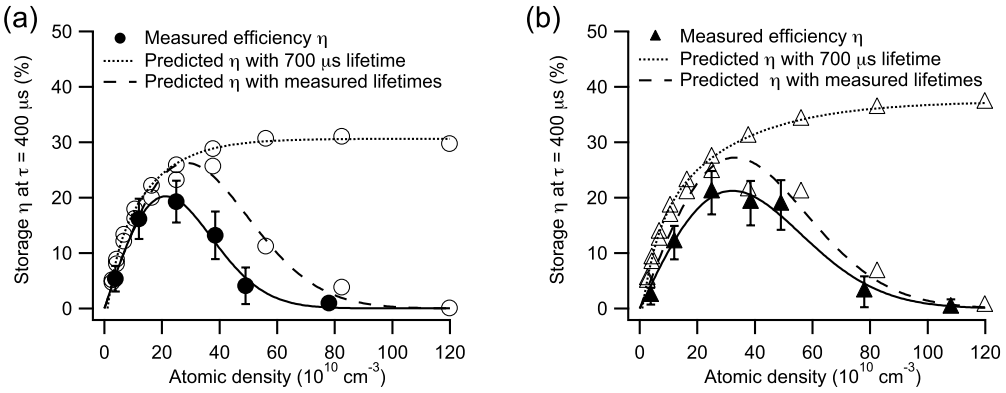

Figure 4.5: Measured and calculated storage efficiency η at fixed storage time $\tau = 400$ μs vs. atomic density for control field laser powers of (a) 3.8 mW and (b) 8.8 mW. Theoretical predictions are shown both for a coherence lifetime of 700 μs with no density-dependent decoherence (open symbols with dotted curves) and for the measured coherence lifetimes shown in Figure 4.6 (open symbols with dashed curves). Comparison of the two calculated results indicates that density or temperature-dependent decoherence during the storage interval dominates high-density losses. The remaining discrepancy between measurement and calculation is likely due to radiation trapping. Error bars are from systematic uncertainty in Rb temperature of ~ 2 °C and of the laser frequency of ~ 150 MHz. *Curves added to guide the eye.*

the scalings of $\Delta T_{abs} \sim d_0$ and $T_{opt} \sim d_0$, we would expect the optimal frequency bandwidth to be quadratic in the EIT line width which is not clearly observed in Figure 4.4(d).

Stored light efficiency was measured for a range of Rb densities between 4×10^{10} cm^{-3} (40 °C) and 100×10^{10}cm^{-3} (80 °C) and storage intervals from $\tau = 50$ μs to $\tau = 1.5$ ms and plotted for $\tau = 400$ μs in Figure 4.5. The efficiencies peak at temperatures between 60 and 65 °C ($23 - 37 \times 10^{10}$ cm^{-3}), falling at higher optical depth. The $1/e$ coherence lifetimes during storage (*i.e.*, the time constant from an exponential fit to a storage area vs. storage time plot, see Figure 4.6) also fall at high density. This points to possible high-density or high-temperature phenomena adversely affecting slow and stored light.

Increased loss during storage and readout at high optical depth agrees with predictions from theoretical simulations when the density dependence of decoherence is included

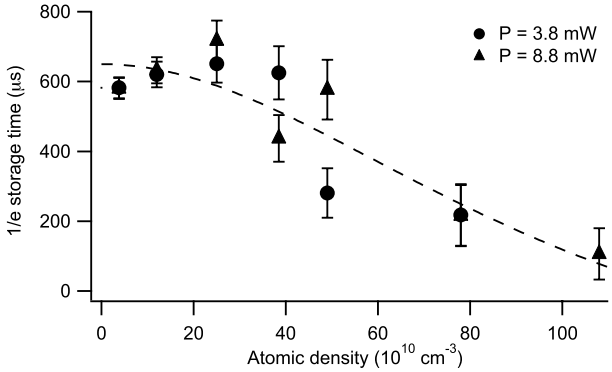

Figure 4.6: Lifetimes of stored coherence as a function of atomic density, derived from measurements described in text. The coherence lifetime drops at high atomic density, likely due to the effect of temperature-dependent losses such as Rb-Rb spin exchange. Error bars are derived from Rb temperature and laser frequency uncertainty as well as statistical uncertainty in fits to coherence lifetimes. *Dashed line added to guide the eye.*

(Figure 4.5). The simulations, described fully in earlier work [68, 69, 70, 71, 3], consist of iterated solutions to the stored light dynamics equations for an ensemble Λ-system. The dashed curve in Figure 4.5 uses the measured rates of decoherence during storage and read-out taken from Figure 4.6 as an input parameter for the spin-wave decay rate, and most closely matches the experimental results.

4.4 Stored light energy accounting

In this section we verify that the loss mechanisms for stored light are consistent. A slow light pulse that is not stopped in the medium (the control field is left on) has loss from imperfect EIT transmission and from pulse bandwidth lying outside the region of maximum transmission (after normalization to a reference pulse; this is the "slow-light efficiency"). A stored and retrieved pulse will experience that same loss, and additional loss from two sources: (i) part of the pulse escapes the medium before the pulse is stored (fractional delay

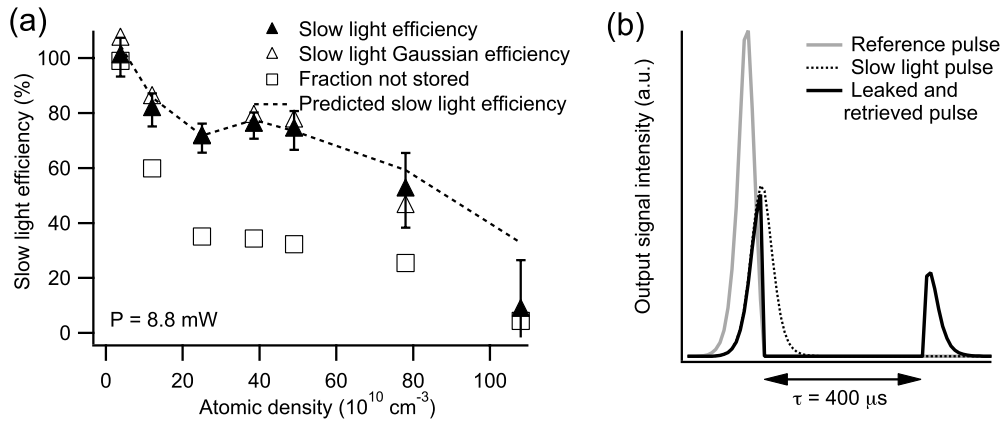

Figure 4.7: (a) Slow light efficiency (output pulse area divided by input pulse area) as a function of atomic density, for input pulse shapes optimized for maximum stored light efficiency (solid triangles) and for input Gaussian pulses with the same FWHM (hollow triangles). Also shown are measurements relevant to stored light efficiency: the fraction of the optimized input pulse that escapes the medium before the pulse is stored (open squares). The dashed line combines light storage data at $\tau = 400$ μs and coherence lifetime measurements to predict slow light efficiency (*see text*) in good agreement with measured efficiency. Error bars are from systematic uncertainty in Rb temperature of ~ 2 °C and in the laser frequency of ~ 150 MHz. Error bars on other data sets are of equal magnitude. (b) Sample data for density of approx. 8×10^{11} cm^{-3} showing the retrieved and unstored pulses (dark, solid line), the slow light pulse with optimized shape (dotted line), and the reference pulse (gray solid line).

less than unity implies significant losses from this mechanism); and (ii) atomic coherence decay during the storage and readout periods. Figure 4.7(a) shows the directly measured slow light efficiency η_{slow}, the area ratio of the output pulse to the reference pulse, and an inferred $\eta_{slow,predict}$ from the storage measurement. Using the measured decoherence rate from Figure 4.6 and the storage readout areas at $\tau = 400$ μs, we can back out the storage readout at $\tau = 0$; combining this with the area of the not-stored pulse leakage we infer η_{slow} [see Figure 4.7(b)]:

$$\eta_{slow,predict} = \eta_{leak} + \eta \times \exp(400\ \mu s/\tau_{coherence}), \tag{4.3}$$

where η_{leak} is the leaked pulse area divided by the reference pulse area, and $\tau_{coherence}$ is the atomic coherence lifetime from Fig 4.6. The measured and inferred slow light efficiencies match very well, only deviating significantly at the highest atomic density, where the term with $\exp(400\ \mu s/\tau_{coherence})$ becomes very sensitive to the short coherence lifetime measurement, which is more error prone due to the low signal-to-noise in the signal transmission.

As indicated from both the storage efficiency and the comparison between slow and stored light, at high Rb densities the effectiveness of the medium is reduced. We believe that several mechanisms are responsible for this. First, at higher densities, temperature or density-dependent losses such as Rb-Rb spin exchange become more significant, contributing to decoherence even during the storage interval (see Figure 4.6). Second, in the presence of light at high Rb densities, radiation trapping becomes significant: light absorbed and then incoherently radiated by one Rb atom is reabsorbed by another Rb atom, and this process leads to decoherence and loss of efficiency. In the next sections, we present investigations of high-density losses due to radiation trapping, both with direct measurement of the effect and reducing its magnitude using a change in cell geometry.

4.5 Radiation trapping studies

In this section we discuss radiation trapping and its effect on light storage in atomic vapor cells. First we infer the effect of radiation trapping by examining one-photon linewidths, then directly measure it by observing transverse fluorescence using a simplified experimental apparatus. Finally we compare the performance of two otherwise identical vapor cells with different aspect ratios, showing that a small transverse optical depth can reduce radiation trapping and improve stored light efficiency.

Direct measurements of large optical depths are difficult due to the large corre-

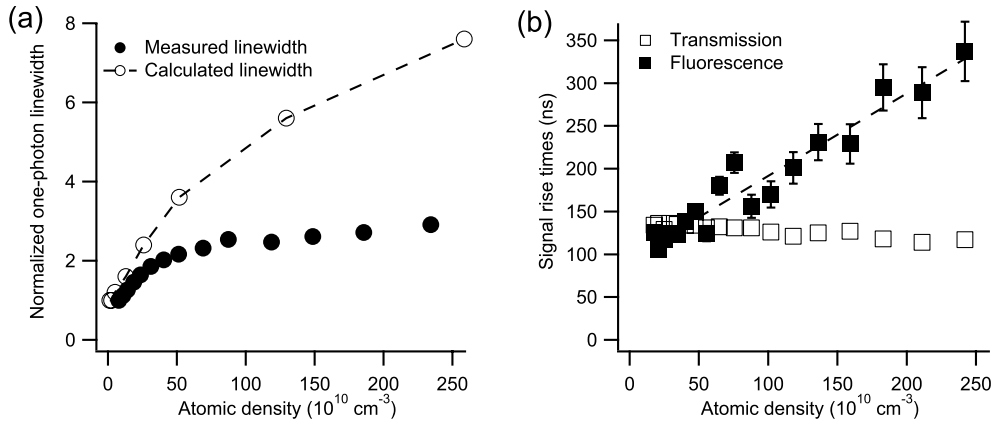

Figure 4.8: (a) Measured and calculated optical line widths for the signal field when detuned from two-photon resonance as a function of Rb density, consistent with an effectively reduced optical depth at high densities due to radiation trapping. (b) Fluorescence signal rise time increases as the atomic density is increased, whereas transmission signal rise time has minimal density dependence, indicating that absorbed and re-emitted photons are trapped in the medium for a longer time due to the large transverse optical depth. (*See text.*) Error bars are smaller than data points except where shown (derived from uncertainty in Rb temperature).

sponding absorption of the optical field. To characterize the optical depth for comparison with the optimization models described above, we used optical absorption linewidth as a proxy for the optical depth. The signal field was detuned from two-photon resonance by changing the frequency driving the EOM and the signal intensity monitored as the one-photon detuning (laser frequency) was swept through resonance. The linewidth of the signal field absorption serves as a proxy for the optical depth because the logarithm of the measured absorption is proportional to the product of the detuning and the optical depth.

Figure 4.8(a) shows a comparison of the measured one-photon linewidth and the expected linewidth from a simple numerical model based on an optically thick sample of three-level Λ-systems. At high densities (and optical depths), the measured linewidth stops increasing while the model shows continued line broadening. We attribute this to radiation trapping: photons scattered inside the medium depolarize the rubidium ground state. Fewer

atoms are polarized in the signal field channel, leading to both decoherence and absorption of the signal field.

We also directly measured the presence of radiation trapping in our vapor cells, with a simplified apparatus. Light from a diode laser was focused through an AOM with a small spot size to allow for rapid rise times in the AOM. This AOM output was turned on and off at a rate of 1 MHz with a rise time of $\sim$ 75 ns. The beam diameter was then expanded to approximately 2 mm and sent into a Rb vapor cell housed inside a small plastic oven, unshielded from stray laboratory magnetic fields, and warmed with resistive heaters to temperatures between 54 and 90 °C. Output light from the cell was measured with two photodetectors: one for transmission, and the other for fluorescence mounted to the side of the cell oven where a lens close to the cell focused scattered light onto the detector. When light was turned on via AOM modulation, the rise time of the signal was observed in both detectors.

Evidence for radiation trapping is shown in Figure 4.8(b). At high atomic densities, the rise time in the fluorescence detection signal increases significantly. The greater the transverse optical depth, the greater the number of absorption and re-emission cycles that occur before absorbed photons exit the medium, so the rise time seen in fluorescence detection should grow with the transverse optical depth. In Figure 4.8(b) we see rise times up to 350 ns, whereas the lifetime for the excited state of the $5p_{1/2}$ state of Rb is $\sim$ 28 ns, indicating many scattering events for each absorbed photon.

In order to minimize the decoherence resulting from radiation trapping in our vapor cells, we developed a cell designed to minimize its effects. A 15 cm long, 1.2 cm diameter cell with N_2 buffer gas was designed to reduce radiation trapping in three ways: (i) the aspect ratio is four times larger than the cell used for stored light experiments in previous sections, which allows fluorescence to escape the cell in the transverse direction with fewer

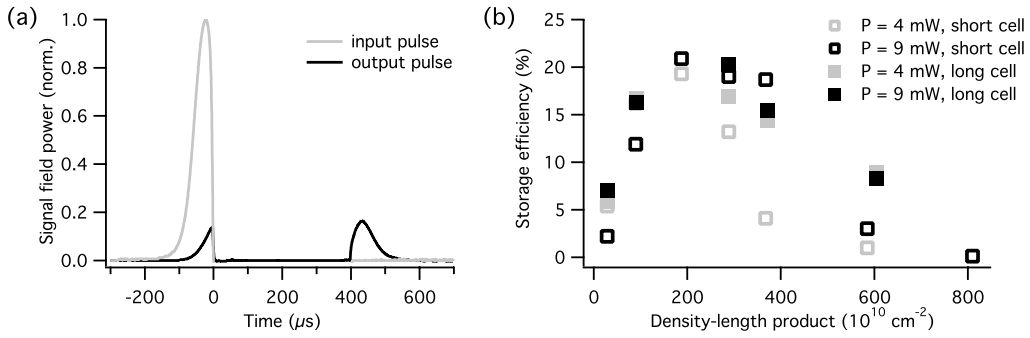

Figure 4.9: Stored light in Ne buffer gas cells, and the dependence on geometry. (a) Example stored light measurement in the long, narrow 40 torr Ne buffer gas cell. The input reference pulse is normalized to the off-resonant transmission level for the probe field. The output probe pulse consists of a leaked part, escaping before the control field is shut off, then a readout after a 400 μs storage interval. Temperature is $T = 57$ °C, and the laser beam diameter and power $d = 6.8$ mm and $P = 9$ mW. Efficiency is defined as the area of the output pulse divided by the area of the input pulse, here 20.3%. (b) Geometry-dependence of stored light, using Ne buffer gas cells, with storage efficiency plotted against the density-length product. At high optical depth, the short cell yields very low efficiency, while the long, narrow cell has significantly greater efficiency. We attribute the improved storage efficiency to a reduction in radiation trapping due to reduced transverse optical depth from both a smaller cell diameter and lower Rb density.

depolarizing interactions with Rb atoms; (ii) the absolute length of the cell is twice that of the other cell, allowing the equivalent longitudinal optical depth to be reached at lower Rb density, minimizing density-dependent effects, including spin exchange; (iii) N_2 buffer gas acts to quench radiation trapping by collisionally de-exciting Rb atoms before the atoms fluoresce, preventing the emission of unpolarized photons that could destroy the coherence of nearby atoms. A cell of the same geometry but with 40 torr of Ne buffer gas was also used, to distinguish between the role of geometry and the role of buffer gas type, as this cell could be compared to the lower-aspect-ratio cell used in preceding sections.

To test the effects of cell aspect ratio, we compared stored light results in two 40 torr Ne buffer gas cells with different geometries: a longer cell with $D = 1.2$ cm and $L = 15$ cm,

and a shorter cell with $D = 2.5$ cm and $L = 7.5$ cm. Optimal stored-light efficiency was measured using the iterative processed described in Section 4.2 as a function of optical depth for a fixed storage time of $\tau = 400$ μs, at two laser powers. Results (Figure 4.9) showed generally improved efficiency for the long cell relative to the short cell. Long cell data is plotted with the same efficiency data from Figure 4.5, against the density-length product.

At high optical depth, the long cell yielded much higher efficiency, indicative of reduced radiation trapping in the high-aspect-ratio cell. However, the theoretically expected larger overall efficiency [69] was not achieved. We attribute this to the presence of greater magnetic field inhomogeneity in the long cell. The addition of higher order compensating coils could reduce this inhomogeneity and may improve the storage efficiency.

Our measurements suggest that a high aspect-ratio cell is a route towards improved efficiency. Such aspect ratios were also investigated in a cold atom cloud, where radiation trapping was reduced, enabling laser cooling to much higher phase-space densities [73].

4.6 Ne and N_2 buffer gas comparison

We compared the use of Ne and N_2 buffer gases in EIT with the aim of mitigating radiation trapping in stored light media. Radiation trapping occurs when atoms absorb input light, then undergo spontaneous emission; these emitted photons can then be re-absorbed and re-emitted multiple times before escaping an optically-thick atomic medium. Since spontaneously-emitted photons have random polarization, re-absorbed photons act to equilibrate the population distribution among different Zeeman sublevels, reducing the optical pumping efficiency and coherence lifetime. Radiation trapping can significantly impact the polarization of an EIT medium [38, 39, 40, 74] and thus potentially the efficiency of stored light.

To reduce the negative effects of radiation trapping, we tested nitrogen as buffer gas, since nitrogen de-excites the Rb atoms without scattering photons by transferring the energy to vibrational states in the N_2 molecules [38, 39, 40]. We note that many optical pumping experiments have used nitrogen for this purpose but these studies used much higher nitrogen pressure than we use here [75, 76]. We used two identical ^{87}Rb vapor cells, one with 40 torr of Ne, and the other with 25 torr of N_2 chosen such that the excited state pressure broadening (γ) was the same in both cells. The nominal optical pumping rate, Ω_c^2/γ, was then the same in both cells for a given laser power. Since radiation trapping depolarizes and decoheres the atomic ground state, we used measurements of EIT (which is based on ground state coherence) in the two cells to study the effect of radiation trapping.

EIT is sensitive to both optical depth and ground state decoherence, and is thus, as shown in Chapter 3, a useful proxy for slow and stored light experiments [77]. In particular, the off-resonant floor of an EIT spectrum is determined by the effective optical depth d_0: $F = \exp(-2d_0)$, where d_0 is proportional to the optical path length, the atomic density, and the fraction of atoms in the relevant atomic levels. The peak transmission is determined by the control field Rabi frequency, the effective optical depth d_0 and the ground state coherence decay rate γ_0 : $F + A = \exp(-2d_0\gamma\gamma_0/\Omega_c^2)$. Here, the floor ($F$) and amplitude ($A$) are normalized to the off-resonant transmission level of the probe light, as shown in Figure 4.10(a). In general, a lower floor and a higher EIT transmission are desirable for stored light experiments.

We observed lower EIT floors and higher peak transmissions in Ne buffer gas cells than in N_2 cells (Figure 4.10). Therefore, we expect reduced stored-light performance from the N_2 buffer gas cell in comparison to the neon cell. We believe the increased EIT floor in the N_2 cell was predominantly due to increased population in the $|F = 2, m_F = 2\rangle$ trapped end state. The σ^+ polarization of the control and probe light led to optical pumping into

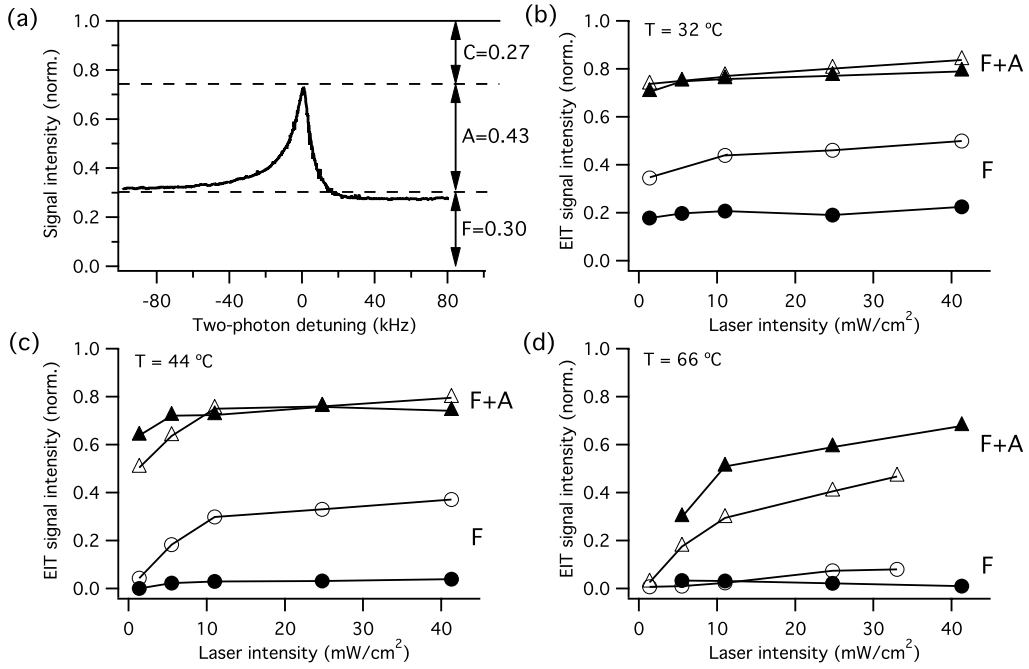

Figure 4.10: Comparison of EIT measurements in neon and nitrogen buffer gas, demonstrating reduced effective optical depth in N_2. (a) Example EIT spectrum, normalized to the full off-resonant signal transmission level, with the 25 torr N_2 buffer gas cell at $T = 44$ °C and with 12 mw/cm^2 input laser intensity. The contrast levels are labeled by F, the off-resonant transmission level, which is a measure of the system's optical depth; A, the EIT amplitude; and C, the normalized difference between full transmission (away from the ^{87}Rb D_1 transition) and the peak of the EIT spectrum. EIT contrast levels F (circles) and $F + A$ (triangles) vs. laser intensity for both 40 torr Ne (solid symbols) and 25 torr N_2 (open symbols) are shown for Rb cell temperatures (b) $T = 32$ °C, (c) $T = 44$ °C, and (d) $T = 66$ °C.

this state, which was then inaccessible to the EIT process, effectively reducing the optical depth and raising the EIT floor. As seen in Figure 4.10, the floor level increased with laser intensity in both cells because more atoms were optically pumped into the trapped state at high laser intensity. The higher EIT floor in the N_2 buffer gas cell was indicative of more efficient optical pumping to the trapped state, and poorer performance for slow and stored light.

Since radiation trapping reduces optical pumping efficiency, the higher trapped

state population in the N_2 cell may indicate that this cell had less radiation trapping. However, the population distribution as Rb de-excites to the ground state in the presence of different buffer gases may also play a role. We carried out a full 16-level density matrix simulation of both cells in the optically thin regime, and found that if the Rb atoms are quenched to the ground state with the same m_F state before excited state mixing occurs (as in the N_2 cell) there is a higher population in the trapped state. However, if Rb is allowed to de-excite to all allowed ground states (as in the Ne cell, since the excited states are uniformly mixed before spontaneous emission), then there is less population in the trapped state. Detailed modelling of the population distribution after optical pumping requires branching ratios of Rb de-excitation in the presence of various buffer gases and further study will be required.

The N_2 buffer gas cell also showed lower peak EIT transmission (Figure 4.10) due to the larger ground state decoherence rate in the nitrogen cell. We also measured the ground state coherence decay rate by the $1/e$ time of stored light efficiency vs. storage time, and found a decoherence rate that was four times greater in the nitrogen cell. Shorter atom-light interaction time (the diffusion time) in the nitrogen cell contributed to this increase in decoherence. The N_2 buffer gas did not provide better EIT than Ne buffer gas, due to increased pumping of Rb atoms into the trap state. Further work is needed to understand the details of Rb de-excitation, and other techniques must also be developed to reduce the effects of radiation trapping in stored light vapor cells.

4.7 Conclusions

Our experiments here investigated slow and stored light at a variety of Rb densities (*i.e.*, optical depths), and as a function of pulse duration, delay and storage time, and control

field intensity. Experimental results are in good qualitative agreement with theoretical calculations based on a simplified three-level model at moderate densities; and indicate that radiation trapping is an important limitation at high atomic density. Results with both N_2 and long, narrow cells show promise for reducing the effects of radiation trapping. Optical pumping of population into trapped end states needs to be addressed before one can make effective use of an N_2 buffer gas cell. The long, narrow cell is also a promising route to high efficiency with improved magnetic field compensation. Our results showing the superior EIT contrast performance in the Ne buffer gas cell may have implications outside of the study of slow and stored light, as vapor cell atomic clocks have frequently employed N_2 buffer gas to quench radiation trapping; the reduced excited state mixing that changes population distributions will affect lineshape contrast and thus clock performance as well.

The study of the role of optical depth in slow and stored light in vapor cells continues in the following chapters. The rest of this work shifts to Rb vapor cells with anti-relaxation coating on their inner walls, while still seeking to optimize slow and stored light in vapor cell systems.

Chapter 5

EIT in Paraffin-coated Vapor Cells

5.1 Introduction

This chapter covers EIT in coated cells, including both Zeeman and hyperfine configurations, as we probe the possibility of long time scale slow and stored light, with a thorough study of the EIT on which they are based.

Anti-relaxation coatings in rubidium vapor cells allow atomic coherent spin states to survive many collisions with the cell walls. This reduction in the ground state decoherence rate gives rise to ultra-narrow-bandwidth features in EIT spectra, which can form the basis of, for example, long time scale slow and stored light, sensitive magnetometers, or precise frequency standards.

We first study how Zeeman EIT contrast and linewidth are determined by cell and laser beam geometry, laser intensity, and atomic density. Using a picture of Ramsey pulse sequences, where atoms alternately spend "bright" and "dark" time intervals inside and outside the laser beam, we explain the behavior of EIT features in coated cells, highlighting their unique characteristics and potential applications.

Then, using coated cells in the hyperfine configuration for EIT allows slow light

pulses to propagate without off-resonant absorption; but also requires longitudinal atomic motion to be confined to the hyperfine wavelength, not realized in most buffer-gas-free coated cells. We employed a narrow, miniature coated cell geometry, which is itself useful for several applications, to study hyperfine EIT, slow, and stored light.

Atomic coherence lifetime is often limited by the interaction time between the atoms and resonant light fields. For a dilute atomic vapor interacting with a laser beam and constrained inside a cell, the interaction time is the time of flight of an atom through the beam, as in the vacuum cell results from Section 2.4. In cells with anti-relaxation coated walls [31, 26, 32, 78], atoms move ballistically and maintain coherence during wall collisions, allowing for coherent interactions over many beam crossings. These long coherence lifetimes result in very narrow resonances. If the optical pumping interaction is sufficiently slow, velocity averaging during multiple passes of atoms through the beam places the system in a regime of Dicke narrowing [79]. Lifetimes of up to 1 second have been observed in coated cells [34, 35]. Such cells have shown promise for a number of applications, such as magnetometry [80], atomic clocks [26], squeezing [81] and quantum information storage [82]. Of particular interest here are applications based on EIT [11]. For example, the slowing and storing of optical information [1, 16, 18, 17, 21, 22] in atomic vapor relies on long coherence times of atomic ground states, and the possibility of realizing long storage times leads us to investigate the underlying EIT in coated cells.

Most coated cell applications operate in a regime of either very low laser intensity to take advantage of ultra-narrow widths (clocks or magnetometers), or high intensity for stronger optical pumping and efficient readout (information storage). Here we will investigate the more complex intermediate intensity regime, which embodies characteristics of both low and high intensity. This regime supports higher EIT contrast, which along with coherence lifetime is important in many quantum optics applications. In the next three

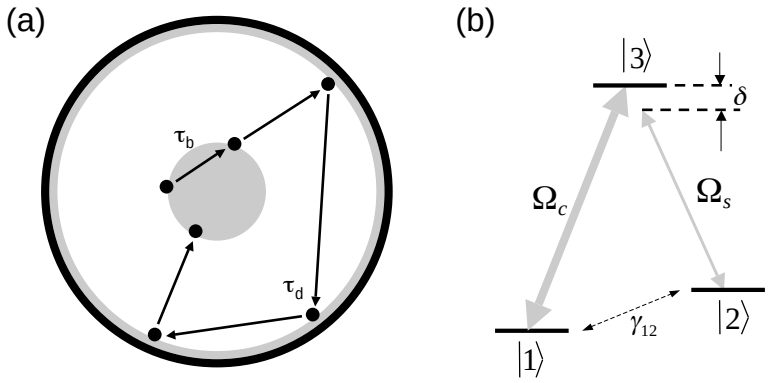

Figure 5.1: (a) Cross-section view showing the coated cell and beam geometry. Both the bright time interacting with the beam τ_b and the dark time outside it τ_d are important in determining the character of the EIT line shape. (b) Three-level atomic system under consideration, Λ scheme.

sections we study and characterize Zeeman EIT in a paraffin-coated, warm ^{87}Rb vapor cell, and seek to understand EIT behavior in all three intensity regimes, in particular the less-often-employed intermediate one, where we can propose novel stored light experiments that support high-bandwidth signal storage with long storage times.

This systematic investigation of EIT lineshapes reveals a number of interesting results: a characteristic dual-structured shape, unique saturation limits, and unique beam/cell geometry dependence of the two structures. The physics behind the EIT properties is illuminated by treating the system as undergoing a set of Ramsey pulse sequences [83, 84, 59, 60] where the distribution of times atoms spend inside and outside the laser beam [see Figure 5.1(a)] are key to determining the system's behavior, both in the static EIT case and in dynamic applications like slow and stored light.

The Zeeman EIT material in this chapter is organized as follows. Section 5.2 explains the dual-structured nature of EIT in coated cells, drawing on a Ramsey pulse sequence picture of "bright" and "dark" times, and describes a numerical model used to predict EIT linewidths. Section 5.3 describes our coated Rb vapor cell and the surrounding

apparatus. Results appear in Sections 5.4 and 5.5. In 5.4 we study the EIT linewidth, which saturates at the laser intensity where single-pass optical pumping occurs; we also find that the broad and narrow structure widths exhibit opposite dependence on beam size; all of which is consistent with the Ramsey-based picture and the numerical model. In 5.5 we study EIT contrast, which turns out to be highest in the intermediate intensity regime, and discuss its optimization and limitations, including radiation trapping and optical pumping into nonparticipating trapped states. Contrast data fits well to a four-level model that includes a trapped state (in the style of [41], as in Section 3.4). We conclude with a proposed experiment to store a light pulse at high intensity, with high bandwidth, then retrieve it after a long storage time enabled by the anti-relaxation wall coating, which is tested in Chapter 6.

In the last three sections of this chapter we investigate EIT and slow light using the hyperfine configuration in a coated cell. These are the first such measurements reported [85], as hyperfine EIT without buffer gas confinement imposes strict requirements on the shape of the cell. Using such coated cells in the hyperfine configuration for EIT allows slow light pulses to propagate without off-resonant absorption; but also requires longitudinal atomic motion to be confined to the hyperfine wavelength, not realized in most buffer-gas-free coated cells. We employed a narrow coated cell geometry, which is useful for several applications, to study EIT, slow, and stored light. We also investigate the interplay between wall coating quality and optical pumping into an inaccessible trapped state.

5.2 Theory for EIT in coated cells

Many EIT-based vapor cell experiments, as noted above, use low or high laser intensity, both resulting in standard, single transmission peak lineshapes. However, in the

most general case EIT lineshapes in coated cells exhibit a dual structure, with a broad feature tied to the transit time of atoms moving through the laser beam, and a narrow feature resulting from atoms repeatedly interacting with the beam and then evolving in the dark between wall collisions.

Consider the three-level Λ-system of Figure 5.1(b), a simplified version of the full energy level diagram of Figure 2.9. A control field Ω_c drives the transition $|1\rangle \rightarrow |3\rangle$, while a weaker signal field Ω_s drives the $|2\rangle \rightarrow |3\rangle$ transition. Together, these fields optically pump the three-level system into a dark state [19, 20] (see Section 1.2), a particular coherent superposition of $|1\rangle$ and $|2\rangle$, which has the same relative phase as that between Ω_c and Ω_s: $|D\rangle = [\Omega_s|1\rangle - \Omega_c|2\rangle]/\Omega$, where $\Omega = [\Omega_c^2 + \Omega_s^2]^{1/2}$. Atoms in this dark state, which is decoupled from the two input light fields, absorb no light, and transmission of the signal field is maximized. On two-photon resonance ($\delta = 0$), the phase relation between the ground states is constant. Away from resonance, the fields accumulate relative phase at a rate proportional to δ, and atoms prepared in the dark state at time $t = 0$ will no longer be fully in that state at $t \sim 1/\delta$, having acquired components of the maximally absorbing "bright state" orthogonal to $|D\rangle$. For systems where atoms leave the light fields and return, as in the coated cell work presented here, atoms can dephase out of $|D\rangle$ even for small δ values, and transmission becomes a very sensitive function of two-photon detuning; the resulting ultra-narrow EIT feature's width is determined by the ground state decoherence rate γ_{12}.

Coated cell EIT behaves differently depending on the laser intensity regime. For low laser intensities, atoms may travel through the beam many times before being optically pumped into the dark state, and Dicke narrowing holds. The EIT lineshape can be understood to be based on velocity-averaged atoms that are effectively at rest, with a field interaction based on the average times spent inside and outside the beam. At high laser intensity, in which the atoms are pumped into the dark state on time scales short compared to

the beam crossing time, the role of the coating is minimal and the lineshape can be modeled as a non-interacting series of velocity classes with varying one-photon Doppler shifts. The operating regime for some coated cell experiments lies between these two limits, utilizing the typically higher EIT contrast levels (see Section 5.5), leading to, for example, large delay-bandwidth products for slow light. At such moderate intensities, EIT lineshapes exhibit both low and high laser intensity behavior simultaneously, and more careful consideration is required.

Two time scales are present in any buffer-gas-free, wall-coated vapor cell, as illustrated in Figure 5.1(a). An atom moving ballistically across the cell spends a "bright" time t_b interacting with the beam (with mean $\tau_b = \langle t_b \rangle$, averaging over path distributions), followed by a "dark" time t_d (mean $\tau_d = \langle t_d \rangle$) outside the beam, where its state is preserved over some number of collisions with the coated walls. It should be noted that effective dark times can be extended due to the time atoms spend in the beam with large Doppler shifts, or when interacting with a weak laser beam that requires multiple passes to optically pump into the dark state. The number of collisions between interactions with the beam will depend on the ratio of the laser beam diameter to the cell diameter.

In vapor cells *without* wall coatings, atoms are optically pumped into the dark state at rate $|\Omega|^2/\gamma_D$ (where γ_D is the Doppler linewidth), exit the beam at rate $1/\tau_b$, then depolarize on the cell walls. The fraction of atoms within the beam that are in the dark state is limited by the transit time, while the remaining unpolarized atoms contribute to absorption of the applied fields.

In the case of anti-relaxation-coated cells, atomic coherence is preserved over many wall collisions. For two-photon detuning $|\delta| \ll 1/\tau_d$, the total phase accumulated by the fields during the atoms' evolution in the dark is small, and coherence lifetime is limited by the small ground state decoherence rate γ_{12}. For $|\delta| \gg 1/\tau_d$, the coherence is washed out by

inhomogeneous mixing resulting from atoms spending a wide distribution of times t_d outside the beam, and the extra narrow resonance is not present.

As a result of the two time scales τ_b and τ_d, typical EIT spectra exhibit dual structures: a broad, transit-time limited EIT; and an additional ultra-narrow feature with a bandwidth inversely proportional to the dark state coherence lifetime. In the experiments presented here, the ground state relaxation from wall collisions and magnetic field gradients is generally small enough such that the coherence lifetime is limited by optical pumping (power-broadened EIT), and is determined by the geometry of the beam and the cell, and by field intensity. Atoms will be re-pumped into the dark state $|D\rangle$ before they would otherwise dephase into the bright state during time spent outside the beam. The pumping rate is determined by both the light field intensity and the size of the beam (which sets the interaction time).

The situation outlined above is equivalent to atoms interacting with the light fields as if the fields were a sequence of Ramsey pulses [83, 84]; a comparison in buffer gas vapor cells is made in [59, 60]. During extended periods between "pulses" (beam crossings), atoms undergo coherent phase evolution in the dark and inhomogeneously mix upon returning to the beam. Thus longer τ_d gives EIT enhanced sensitivity to changes in δ, narrowing the lineshape.

We model the coated cell system [63] as a collision-less alkali vapor in an infinite cylindrical cell (see also the models in [86, 87]). The axial velocity distribution and the associated Doppler shifts are included (as in [88]). In our infinite cylinder model, an atom's position and velocity are independent, and beam and cell geometry are reduced to bright and dark time distributions. We derive transfer functions which map the initial state of the atomic ensemble to that attained after interaction with the beam or after evolving in the dark for a randomly distributed amount of time with mean τ_b and τ_d, respectively. We then

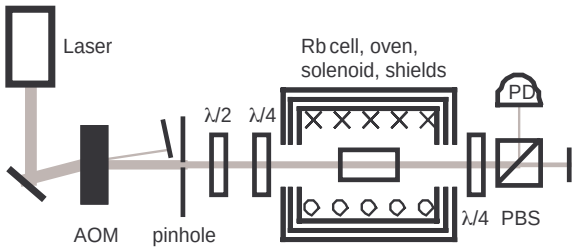

Figure 5.2: Schematic of the apparatus used in coated cell EIT experiments. *See text for details.*

iterate these transfer functions to obtain a steady-state solution. This solution corresponds to the state of an atomic ensemble composed of atoms which have independently experienced an infinite Ramsey pulse sequence, where the alternating interaction and phase accumulation periods in each sequence are $\{t_b^{(1)}, t_d^{(1)}, t_b^{(2)}, t_d^{(2)}, ...\}$, and the times are randomly drawn from the appropriate distribution of "bright" and "dark" interaction times. Results from this model are compared to experimental measurements in Section 5.4, and a detailed presentation of the model is given in [63, 61].

The dual-time-scale picture described here provides a useful framework for interpreting coated cell behavior in many experiments, and in particular for the EIT width and contrast results in our Rb vapor experiment.

5.3 Zeeman EIT: experimental setup

As in all experiments in this work, we measured EIT in warm ^{87}Rb vapor. The experimental apparatus (Figure 5.2) is a simplified version of the general apparatus shown in Figure 2.1. Overall light intensity was regulated by an AOM, and the beam profile improved with a spatial pinhole filter, after which beam size was selected by using interchangeable telescope lenses, with a $1/e^2$ diameter range between 1 and 8 mm. We used circularly polarized light to couple atomic transitions, so quarter-wave plates ($\lambda/4$) on both sides of

the Rb cell converted polarization from linear to circular and back. Polarization was rotated by a half-wave plate ($\lambda/2$), such that the orthogonally polarized control and signal fields had a $10:1$ intensity ratio. The output fields were divided using a polarizing beam splitter (PBS) and the signal field was measured on a photodetector.

The coated Rb cell was housed inside the Nylatron plastic oven, with cell temperature varying between 42 and 73 °C, or atomic number density between 1.4 and 20×10^{10} cm^{-3}. A solenoid surrounded the oven, and the homogeneous magnetic field could be swept slowly to vary the two-photon detuning δ by splitting Zeeman sublevels. The resulting signal field transmission during a δ-sweep constituted an EIT line shape measurement.

The cell used in these experiments was coated, and filled with natural abundance rubidium (28% ^{87}Rb) following the techniques described in [89], in Section 2.3, and in Appendix A. The cylindrical cell had length $L = 5.1$ cm and diameter $D = 2.5$ cm. The minimum two-photon resonance width observed was 22 Hz, which includes losses from wall collisions and from magnetic field gradients. It implies an average number of coherence-preserving wall collisions between 100 and 200, and magnetic field homogeneity of $\lesssim 150$ μG/cm.

5.4 Zeeman EIT: linewidths

5.4.1 EIT linewidth and laser intensity

The high and low intensity limits have straightforward behavior. At high laser intensity, fast optical pumping establishes equilibrium coherence and population on time scales shorter than the beam-crossing time. In this limit, atoms in different velocity classes independently undergo EIT, with a broad linewidth. At low laser intensity, many passes through the beam are required for the population distribution to reach equilibrium. In this

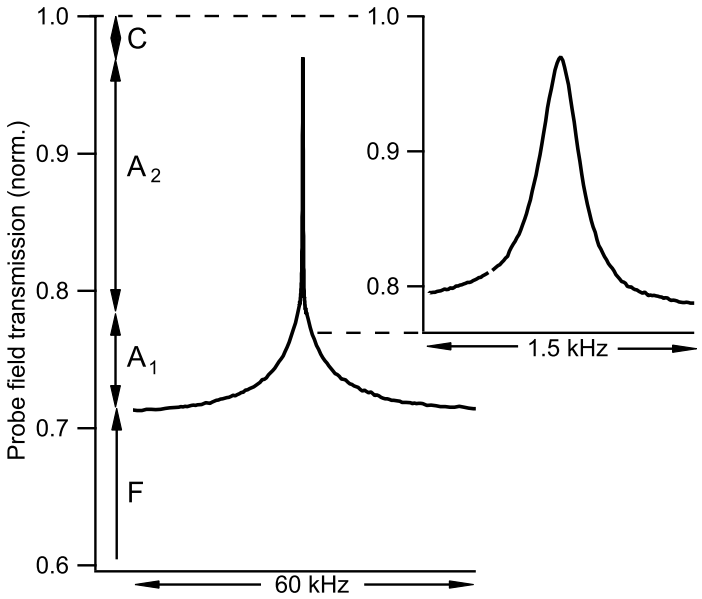

Figure 5.3: Dual-structured EIT characteristic of coated cells using the Zeeman configuration. Signal transmission is plotted against two-photon detuning. Contrast levels are: the floor (F) is the off-resonant transmission level (measured from zero, which is not shown in the plot), a measure of the system's optical depth; A_1 and A_2 are the respective amplitudes of the broad and narrow structures; the ceiling (C) is the difference between the maximum signal transmission (defined to be 1) and the top of the narrow structure. Conditions here are $T = 42$ °C, $I = 2.5$ mW/cm^2, and $d = 3$ mm. The broad structure has width 16 kHz and the narrow 260 Hz. *Inset*: zoomed-in version of the narrow structure.

limit, each atom undergoes many wall collisions, effectively averaging its velocity to zero. This Lamb-Dicke limit [79] leads to narrow, Doppler-free, two-photon resonances.

Maximal coupling to the narrow resonance occurs in an intermediate regime in which there is sufficient laser intensity to create good contrast, yet not so strong as to optically pump the sample during a single pass through the laser beam, nor to optically pump a large fraction of the atoms into the $F = 1$ trapped states, which do not participate in EIT (see Section 3.4). In this intermediate regime, both the narrow resonance attributed to atoms repeatedly interacting with the beam and the broad, single-pass resonance are

visible, as in Figure 5.3.

The EIT width is a key parameter in choosing operating conditions for experiments. For example, magnetometer sensitivity, clock precision, and absolute pulse delay for slow light are determined by the EIT linewidth. As noted earlier, for coated cells there are two widths to consider, as both broad and narrow structures are present in the most general case. Linewidth saturation limits the choice of operating parameters for the narrow EIT structure: higher laser intensity does not increase the available bandwidth.

The linewidths of both structures in Figure 5.3 agree with the bright/dark time picture. The line shape has a broad structure of width ≈ 16 kHz, consistent with the transit time of $\tau_b = (d/v)(\pi/2) \approx 17$ μs ($d = 3$ mm is the beam diameter, $v = 280$ m/s the rms atomic speed, and $\pi/2$ a geometry factor). The narrow, central peak has a width of 260 Hz, above the lower bound set by measurements of the wall decoherence time allowed in this particular cell, and below the upper bound set by the estimated average dark time τ_d.

The Ramsey picture of bright and dark times (t_b and t_d) also indicates that the narrow structure linewidth should saturate with increasing intensity, rather than continue power broadening as it would in most vapor cell systems. This occurs because, for sufficient intensity, light fields optically pump atoms into the dark state in a single pass through the beam. This sets τ_d, an upper limit on the coherence lifetime: the average time for an atom to leave the beam and return once.

This saturation of the narrow linewidth saturation effect is confirmed in Fig. 5.4. At low laser intensity EIT linewidths exhibit the expected power broadening and density narrowing. The widths of both broad and narrow structures increase linearly with laser intensity, scaling like $\gamma_{EIT} \sim I/\sqrt{N}$, with I the intensity and N the atomic density. Data for $T = 51$, 58, and 73 °C are omitted for visual clarity in Figure 5.4, but also follow this relationship, as does data for a $d = 8$ mm beam up to 7 mW/cm^2. At higher intensity,

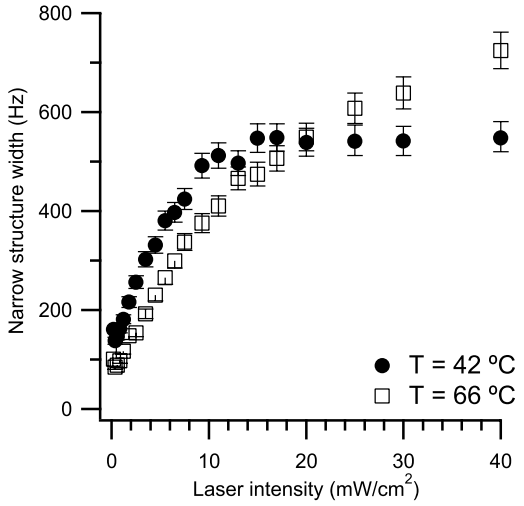

Figure 5.4: Measured width of the EIT narrow structure in a 5 cm long coated cell as a function of laser intensity for $d = 3$ mm laser beam diameter at two temperatures. Broad structure widths (not shown) have the standard linear dependence on intensity due to power broadening. Note the saturation of the linewidth at higher intensity.

the slopes change and the widths saturate, corresponding to an estimated $\tau_d \sim 1$ ms. At the highest temperature ($T = 66$ °C), saturation is not yet reached at our maximum laser power. We attribute this effect to control field depletion at high atomic density, and the resulting variation of the dark state along the length of the cell. A more challenging model would need to be developed to incorporate spatial variation of the input light.

5.4.2 EIT linewidth and beam size

Coated vapor cell experiments employ a range of input laser beam sizes (as a fraction of the cell's cross sectional area). The fraction can be near unity in quantum memory applications [82], where the photon readout probability is maximal when the beam covers the entire area of the atomic ensemble; or near $\sim 1/10$ in magnetometry and slow light applications [80, 89, 90], where longer phase evolution in the dark makes lineshapes

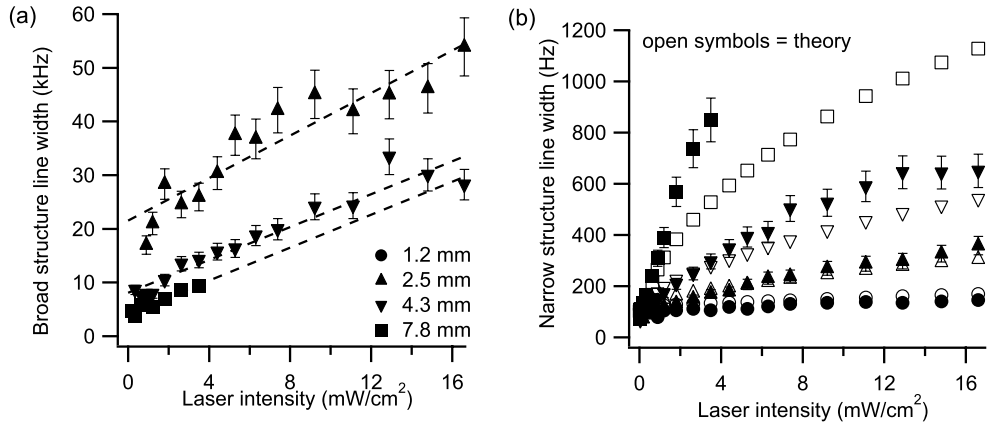

Figure 5.5: EIT broad and narrow structure linewidths in a 5 cm long coated cell as a function of laser intensity for a range of laser beam diameters at $T = 45$ °C. (a) The broad structure width is set by the average transit (bright) time τ_b, and is thus smaller for large beams. (b) The narrow structure has the opposite behavior — width is limited by the average dark time τ_d outside the beam, so larger beams result in wider line shapes. Open symbols are results from a theoretical model, with parameters according to experimental conditions associated with the solid symbol of the same shape. No free parameters are employed.

more sensitive to magnetic fields or allows long-time-scale delay. The geometry of the cell and beam is important in determining EIT lineshapes in coated cells, as the size ratio sets the relative scales for average times τ_b and τ_d the atoms spend inside and outside the laser beam. In this picture, a larger laser beam will reduce τ_d and increase τ_b, leading to a narrower broad structure (which is based on beam transit time), but to a *broader* narrow structure, for a given intensity.

We measured EIT for a number of laser beam sizes. For the broad structure [Fig. 5.5(a)], EIT linewidths scale like $\gamma_{EIT} = \Omega_c^2/\gamma + \gamma_{12}$, *i.e.*, linearly with laser intensity. For low control field intensities, the first term is negligible and the width scales inversely with the transit time across the beam. Thus smaller beams yield wider lineshapes for any given power. This also occurs for lineshapes in uncoated cells with buffer gas.

However, as expected, the narrow resonance behavior is the opposite [Fig. 5.5(b)].

Smaller beams allow longer phase evolution in the dark, making the EIT lineshapes narrower. Results from numerical simulations based on the Ramsey pulse sequence picture are also shown. At low intensity or small beam size, atoms require multiple trips through the beam before being optically pumped into the dark state. The equilibrium fraction of atoms found in the dark state is determined by many independent atom-field interactions and dark times during an optical pumping period. As the number of interactions increases, the choice of individual t_b and t_d distributions becomes less important. Hence, our numerical modeling results agree with experiment better for the smaller beam sizes and low intensities, where our approximate distribution is more accurate.

The ultra-narrow EIT width is highly sensitive to the distribution of dark times. The exact distribution is known, but we assumed an exponential distribution for t_d with a mean equal to the mean of the exact distribution to make calculations tractable. This overestimates the number of atoms returning to the beam after a very short time, but quantitative predictions of linewidths are still possible for small beam sizes or low field intensities due to the final result being dominated by sums of many crossing times rather than the evolution in a single crossing.

The opposing geometry dependence of the broad and narrow EIT structures is important to consider in choosing beam and cell size. For small beams, the two structures are well-defined and distinct; when using one of the bandwidths, the presence of the other feature must be taken into account. For example, an experiment with a small beam could use the broad EIT structure (due to its higher bandwidth, and to the coating improving contrast with its better optical pumping), but the sharp narrow feature would add distortion to signals sent into the medium. For large beams approaching the cell size, the broad and narrow widths approach each other, and the two features are difficult to resolve, resulting in a non-lorentzian EIT shape.

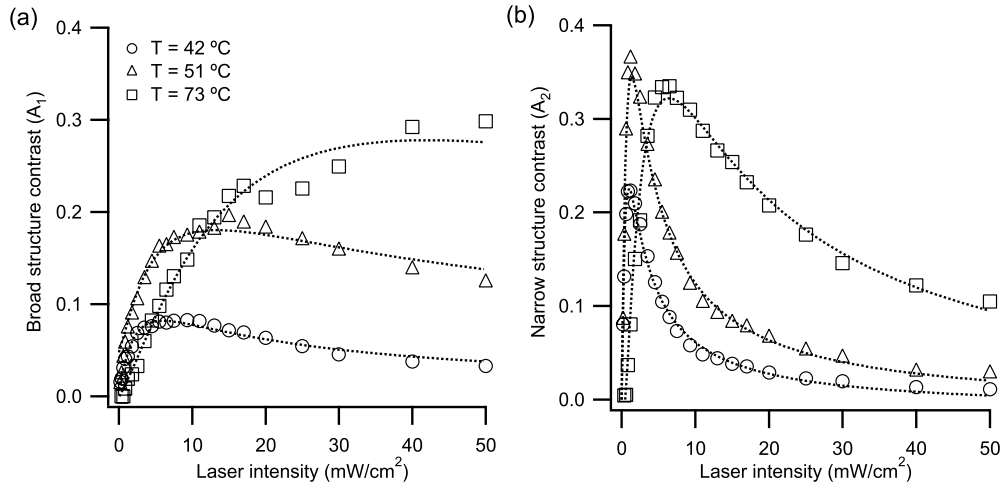

Figure 5.6: EIT contrast vs laser intensity for laser beam diameter $d = 3$ mm at various temperatures. Contrasts are determined from EIT lineshape measurements, such as in Figure 5.3. (a) Broad structure contrast. (b) Narrow structure contrast. Peaks of these plots may indicate optimal conditions for experiments performed in coated cells. Dotted curves are fits to a four-level model (*see text*).

EIT spectra in the preceding plots (Figs. 5.4 and 5.5) were fit to the sum of two Lorentizans. Error bars associated with EIT linewidths are derived from: (i) statistical uncertainty in Lorentzian fits to the data; (ii) uncertainty in the laser frequency leading to with uncertainty of typically $\pm 10\%$; (iii) systematic uncertainty from difficulty distinguishing broad and narrow features: often the width is a sensitive function of the fit range chosen. We chose the fit range that gives the smallest width uncertainty [type (ii)], then added to the error the difference between widths resulting from using 90 or 110% of that fit range. For larger beams and high laser intensity, type (iii) error becomes large because the narrow and broad widths become similar and the narrow structure contrast diminishes.

5.5 Zeeman EIT: contrasts

EIT contrast indicates the strength of interaction between input light and atoms, and high contrast levels are preferred in most experimental applications. The contrasts and widths allow us to propose a stored light experiment that uses both the transit-time and coherence-time scales, enabling long storage times of high-bandwidth signals.

We investigated EIT contrast over more than three orders of magnitude in intensity, for several cell temperatures. Contrast levels reach maximum values at moderate intensities. Figure 5.6 shows the EIT contrast for both broad and narrow structures. Contrast for both structures increases with laser intensity from zero as the pumping rate into the dark state becomes large compared to the ground state decoherence rate. At lower intensity, atoms lose coherence before being fully pumped into the dark state. At high intensity contrast falls because the floor (off-resonant transmission) of the EIT increases. This occurs because of optical pumping into the trapped state sublevels $|F, m_F\rangle = |1, -1\rangle$,$|1, 0\rangle$, and $|1, +1\rangle$, so fewer atoms participate in EIT. Contrast data was fit to a four-level EIT model [41], as in Section 3.4 for contrasts in buffer gas cells. This is a standard Λ-scheme EIT with two input light fields, but with an additional ground state acting as a "trapped" state reached by excited state decay and inaccessible to the light fields.

Despite the greater optical depth, peak contrast levels eventually fall off at high temperature [Fig. 5.6(b)], an effect we attribute to radiation trapping [37, 39, 40, 89], where spontaneously emitted photons are re-absorbed by the atomic medium; atoms in the dark state that absorb such photons lose their coherence. This was measured and discussed in Section 4.5. This also explains why the peak contrast occurs at higher laser intensity for higher temperature, as a faster pumping rate into the dark state is required to reach maximal coupling. Contrast peaking at a transverse optical depth of ~ 1 or 2 in our operating regime

is consistent with a simple three-level EIT analysis, with an appropriate radiation trapping term (see [75]) added to the ground state decoherence rate. We expect radiation trapping to be a more significant effect in coated cells (compared to vacuum or buffer gas), since atoms throughout the cell volume participate in EIT, so spontaneously emitted photons continually reduce overall coherence along the entire path exiting the cell.

Past work [89, 90] has shown that signal pulses can be delayed on either the broad or narrow structure time scale, even in intermediate intensity regimes when both structures are present. However, the extended spin coherence lifetime supported by the wall coating exists during the storage interval (when the input light is off) regardless of which EIT structure was used to slow and store the input pulse. Thus, one can find a maximal broad structure contrast level at high laser intensity, then send a corresponding high-bandwidth signal pulse into the medium (with minimal narrow structure contrast, to avoid pulse distortion). The pulse can be stored as long as coherence is preserved, then read out. For example, values extracted from Figs. 5.5 and 5.6 suggest that a 3 mm beam with 50 mW/cm^2 intensity sent into a $T = 73$ °C vapor cell would establish EIT with a dominant broad structure of $\sim$ 150 kHz; a bandwidth-matching 30 μs slow light pulse could be stored for several ms. This should lead to storage times much longer than the temporal pulse width, where we use the transit-time scale for writing, but the coherence-time scale for storage. This plan will be tested in Chapter 6.

5.6 Hyperfine EIT: experimental setup

Slow light using EIT between non-degenerate ground state hyperfine levels in alkali atoms has the potential for low incoherent losses and improved optical depth in comparison to degenerate Zeeman EIT [30]. However, hyperfine EIT in a paraffin-coated cell requires

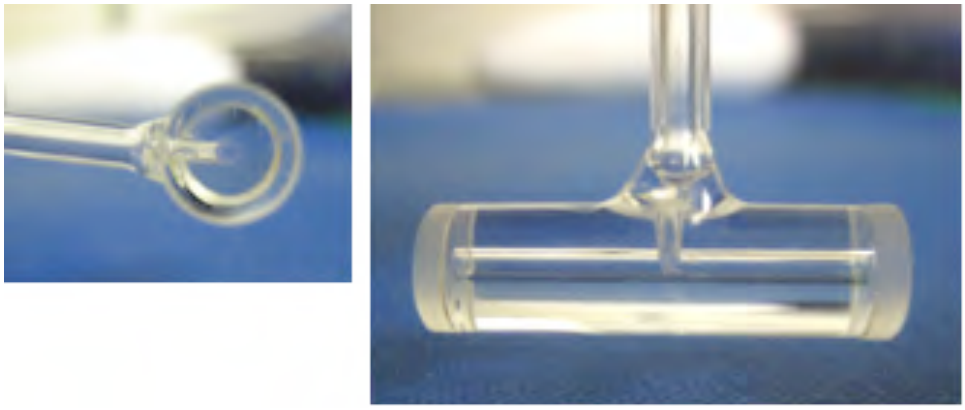

Figure 5.7: Photographs of the miniature paraffin-coated ^{87}Rb vapor cell. The central cylindrical channel as a diameter of 1 mm and a length of 25 mm. (*See text.*)

a careful choice of cell geometry. First, a large optical depth is required for large delay-bandwidth product in slow light and good efficiency in stored light, necessitating a long cell, as deleterious effects such as spin exchange and radiation trapping limit absolute densities. Second, atomic motion must be confined to substantially less than the hyperfine wavelength, to avoid differential phase evolution between the two light fields in the medium, which would increase decoherence and absorption. Third, rapid motional and velocity averaging is necessary for most thermal, Doppler-shifted atoms to interact with the monochromatic optical fields, requiring short mean times between velocity-changing wall collisions and thus a small cell diameter. Combining a long cell for greater optical depth and stronger light-atom interaction, with a small diameter for rapid velocity averaging leads to a high-aspect-ratio cell. Such a long, narrow cell also restricts longitudinal atomic motion due to repeated wall collisions.

In these sections we report the first measurements of coated cell hyperfine EIT and slow light, using a high-aspect-ratio vapor cell. We also investigate the interplay between wall-coating quality and optical pumping into inaccessible trapped states, finding that a cell

with moderate coherence lifetime provides greater effective optical depth and thus greater delay-bandwidth product in slow light than a cell with long coherence time. Results compare favorably to those of standard buffer gas cells (such as the EIT contrast measurements from Chapter 4), and indicate that miniature coated cells could serve as an asset for several applications.

We employed special Rb vapor cells (Figure 5.7) made of 25 mm long, 1 mm i.d. Pyrex capillary tubing with optical flats fused to the ends. A 1 mm hole was drilled perpendicular to the length of each cell and a larger glass sidearm was fused to the cell to hold metal Rb and to connect to a vacuum system during fabrication. The 1 mm $\times$ 25 mm dimensions ensured that, on the timescale of typical slow-light experiments, few atoms travel a significant fraction of a hyperfine wavelength (4.4 cm for the ^{87}Rb D_1 transition) despite the absence of buffer gas confinement. Instead, atoms repeatedly interact with the cylindrical walls slowing any motion along the cell.

Each cell was coated with tetracontane ($C_{40}H_{82}$) [31, 32, 78]. Tetracontane flakes were placed in the sidearm before evacuating and heating the cell and surrounding tubing above the paraffin vaporization temperature of $\approx$ 200 °C. The cell walls were uniformly cooled to coat the entire cell. Isotopically enriched ^{87}RbCl salt and CaH_2 were crushed and mixed together, then heated to $\approx$ 500 °C to produce ^{87}Rb metal (along with CaCl salt and H_2 gas). The metal was then distilled into the sidearm, which was then sealed [91]. Techniques for constructing these miniature coated cells are explained more fully in Appendix A. Two narrow cells were employed in the experiments reported here: a cell with a "good" wall coating, which provided an intrinsic hyperfine EIT FWHM linewidth of 20 kHz and Zeeman EIT FWHM linewidth of 750 Hz; and a cell with a "moderate" quality wall coating, which provided a hyperfine EIT linewidth of 45 kHz and a Zeeman EIT linewidth of 9 kHz [92].

The apparatus for detecting hyperfine EIT and slow light in the miniature coated

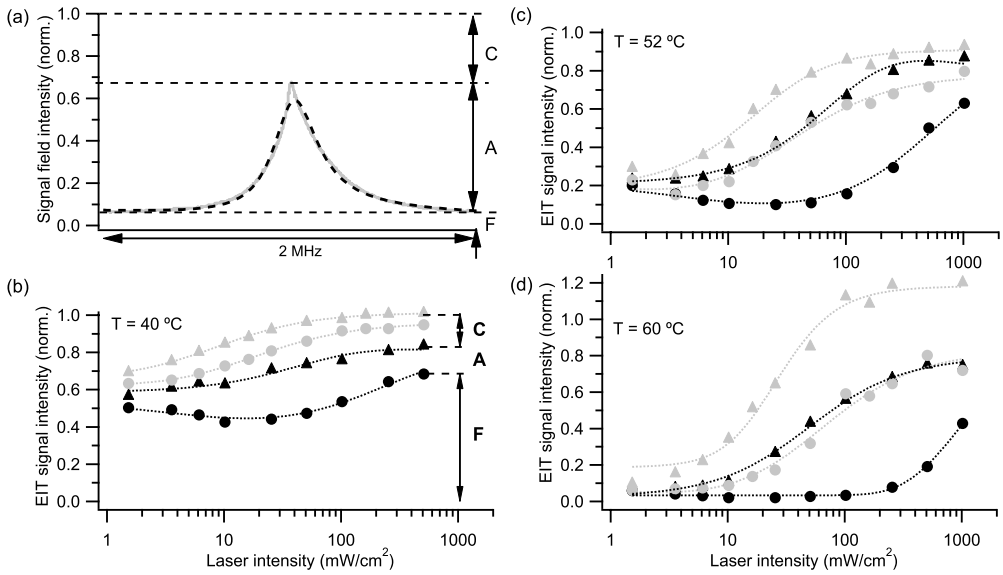

Figure 5.8: Measured EIT behavior in miniature paraffin-coated cells. (a) Characteristic non-Lorentzian EIT lineshape, normalized to far-off resonant signal light transmission; dotted curve is a Lorentzian fit. Data from the cell with shorter coherence time is shown. $T = 60$ °C, $I = 100$ mW/cm^2. Contrast parameters are $F = 0.08$, $A = 0.60$, and $C = 0.32$, and the linewidth is 180 kHz. (b, c, d) EIT contrast parameters F (circles) and $F + A$ (triangles) as functions of laser intensity for $T = 40$, 52, and 60 °C, (respective Rb densities are 4, 12, and 25×10^{10} cm^{-3}). Black symbols are for the cell with shorter coherence time, gray symbols for the longer coherence-time cell. Dotted curves are fits to a four-level model (*see text*).

vapor cells is the same used for the slow-light-from-EIT measurements in Chapter 3, where input light fields were formed using a driven EOM, and the output signal field light was separated using a temperature-stabilized etalon (Figure 2.3). The only difference is in the beam size, which was brought to a soft focus of 500 μm at the center of the vapor cell.

5.7 Hyperfine EIT: contrasts

The measured EIT lineshapes exhibited a non-Lorentzian shape typical of coated cells. See Figure 5.8(a). This non-Lorentzian lineshape consists in general of a narrow

peak, based on the phase evolution of atoms that spend significant time outside the laser beam between repeated interactions with the beam; atop a broad pedestal, based on the single pass time-of-flight of atoms through the beam [59, 89]. This was described in the first several sections of the present chapter. For a beam size comparable to the cell size, such as employed here, these two components of the coated-cell EIT spectrum merge together into a single non-Lorentzian resonance [Fig. 5.8(a)], unlike the distinct dual-structure nature of the Zeeman EIT with a fractionally smaller beam (Figure 5.3). Long slow light pulse delays or storage times can be achieved in coated cells, due to the extended spin coherence lifetime allowed by the wall coating [18, 89].

In addition to long coherence times, high EIT contrast is crucial for good slow and stored light efficiency. EIT contrast is described as before with the three parameters F, A, C, which vary as a function of laser intensity, cell geometry and properties, and atomic density [Fig. 5.8(b-d)], enabling the parameters to be adjusted to optimize slow and stored light performance. The peak signal transmission level $(F + A)$ increases with laser intensity, as more atoms are optically pumped into the EIT dark state [19, 20]. The off-resonant signal transmission level (F) is also power-dependent: at modest laser power, atoms will be optically pumped out of the $F = 2$ states and into $F = 1$ states, increasing the effective optical depth for the signal field and thus reducing F; however at high laser power the signal field will also pump atoms out of the $F = 1$ states and atoms will be optically pumped into the $|F = 2, m_F = 2\rangle$ trapped state, reducing effective optical depth and increasing F.

We performed numerical simulations using the full set of D_1 transition states [93] and variable input light intensity, which reproduce this effect. We also find good agreement between measured EIT contrast at all laser powers and a simple four-level model including an extra "trapping" level in the ground state to which population can be optically pumped but which then does not interact with the optical fields [41].

There is a quantitative connection between experimentally-measured EIT lineshapes and slow light behavior [29, 77], as derived in Chapter 3. Slow light fractional delay (delay-bandwidth product) and transmission are both greater for larger EIT amplitude, A, and smaller floor, F. The measured EIT contrasts for coated cells, shown in Fig. 5.8, are comparable to similar experiments done in buffer gas cells [77] (Chapters 3 and 4), although our narrow cells' length of only 25 mm leads to reduced optical depth (higher F values), limiting the slow light delay.

EIT with conditions more favorable to slow light are found in the cell with the *shorter* coherence lifetime (black symbols), which has smaller F and larger A values for almost all laser intensities and Rb densities. A longer coherence time leads to enhanced optical pumping into the trapped state $|2,2\rangle$, and hence greater reduction of the effective optical depth. Depopulating the $|2,2\rangle$ state is likely needed to properly take advantage of longer coherence times and achieve high EIT contrast without suffering reduced optical depth. Thus for a given cell length, there will be an optimal maximum atomic ground state coherence time.

We also observed resonant transmission $F + A > 1$ at high laser intensity for the long coherence-time coating cell [Fig. 5.8(d)]. We attribute this to gain in the signal field induced by four-wave mixing [94]. This process is more pronounced at high Rb density and high laser intensity, and its efficiency is enhanced by the long coherence lifetimes provided by the high-quality wall coating. Such amplification may improve slow light in classical information applications.

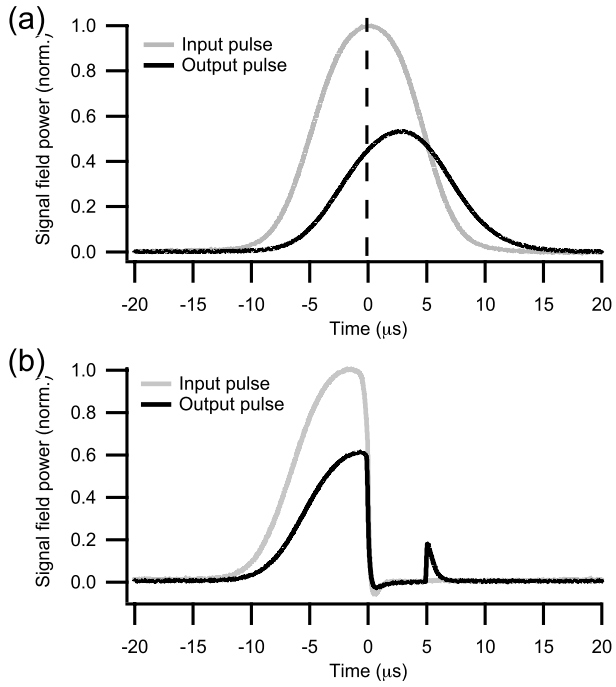

Figure 5.9: Measured slow light in the miniature coated cell with shorter coherence time. Fractional delay is 0.26 and the transmission fraction is 0.53. $T = 60$ °C and $I = 250$ mW/cm^2.

5.8 Hyperfine EIT: slow and stored light

The next chapter is devoted to long-time-scale slow and stored light using coated cells in the Zeeman EIT configuration. Because of the miniature cell's size and limited coating quality, the high wall collision rate prevents operation at long times scales. Hyperfine slow and stored light in coated cells do have potential uses in quantum memory applications (discussed below), and these are the first such measurements, and included here.

An example slow light pulse is shown in Figure 5.9, for the narrow coated cell with shorter coherence time and for near-optimal values of F, A and C [see Figure 5.8(d)]. An input pulse length of 10 μs was used to fit within the EIT linewidth. In this example, the input pulse is delayed by 0.26 of its width, and retains more than half its original amplitude

with minimal pulse broadening.

A stored light experiment for an input pulse of the same 10 μs width is shown in Figure 5.9(b), with a storage time interval of 5 μs, several times longer than the time atoms take to cross the beam, again demonstrating enhanced storage time due to the wall coating. Most of the pulse is lost to absorption (imperfect EIT contrast) and leakage (imperfect fractional delay); the stored component of the pulse is mostly retained over this time scale. Efficiencies are consistent with the slow light transmission and delay shown in Figure 5.9(a), and measured decoherence rates. Both slow and stored light performance should improve with more refined state selection combined with better coating techniques for longer narrow cells to enable small F and large A.

In conclusion, we have demonstrated hyperfine EIT, slow, and stored light in narrow, anti-relaxation coated vapor cells. The unconventional geometry dictated by the need for limited longitudinal atomic motion could be an asset for a number of applications. Small systems for vapor cell physics have found use in atomic clocks [95, 96], and potentially in magnetometry where the motional averaging is over a small volume. Rapid diffusion out of the beam in small cells makes buffer gas less viable as a mechanism to extend coherence lifetime.

Quantum optics applications such as a coated cell "slow light beamsplitter" [90] (see Chapter 7) could see improved transfer of information between multiple channels in a smaller medium. Future work may also use miniature coated cells for single photon storage [4, 7]. More complete optical pumping facilitated by the wall coating, and the absence of dephasing collisions occurring inside the beam should improve the repeatability and efficiency of such experiments.

Chapter 6

Slow and Stored Light in Coated Cells

6.1 Introduction and experimental setup

In Chapter 5 we characterized EIT in paraffin-coated Rb vapor cells, highlighting their unique dual-structured nature, with the standard broad feature based on beam transit time, and an ultra-narrow feature resulting from atoms in the dark state superposition leaving the presence of the input light fields, phase evolving in the dark, and returning. The dual-width property of coated cell EIT permits optical signal field pulses to propagate with reduced group velocity on two separate time scales.

In this chapter we will explore the optimization of pulse delay in such coated cell systems by measuring slow and stored light as a step towards the application of vapor cells for a quantum memory [20, 3] in a quantum repeater [2] as well as for long delay times for classical pulses. First, we utilize the ultra-narrow feature of the dual-structured EIT spectrum to achieve ultra-slow group velocities for the propagation of weak classical pulses through the EIT medium [18]. Then, we will explore the limitations of coated cell slow light and mitigate them with the addition of a second laser beam to optically pump atoms out of the optical-depth-reducing trapped states (which were discussed in Chapters 3, 4,

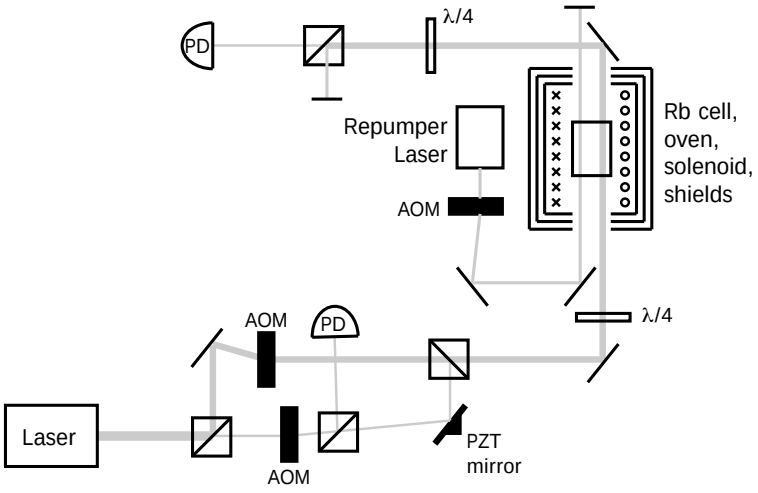

Figure 6.1: Schematic of the experimental apparatus used for Zeeman-EIT-based slow and stored light in paraffin-coated cells. *See text for details.*

and 5). Finally we characterize stored light in coated cells. We can achieve long storage times with limited efficiency using the narrow EIT structure to propagate signal pulses; but we find promising developments in the idea proposed in Chapter 5 for storing light using the broad structure to propagate pulses while taking advantage of long coherence times during the storage interval. Using our understanding of how stored light efficiency depends on our experimental parameters, we can propose a way to achieve high-efficiency, long-time-scale storage of high-bandwidth pulses with an improved and optimized experimental setup.

The experiments performed in this chapter use the Zeeman EIT configuration for slow and stored light, which is described in Chapter 2. Since the signal field in slow light experiments is dynamically shaped, the apparatus is similar to that shown in Figure 5.2, but with the dual-AOM configuration of Figure 2.2 replacing the half-wave plate. This is shown in Figure 6.1. The coated cell is the same as was used in Chapter 5, with a 5.1 cm length and 2.5 cm diameter, filled with natural abundance Rb, with paraffin-coated inner walls that support EIT linewidths as narrow as 40 Hz.

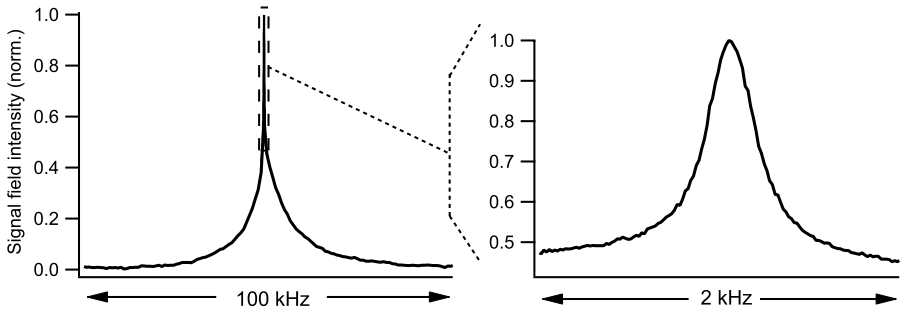

Figure 6.2: Measured dual-structure EIT lineshape characteristic of coated cells. The full widths are 13 kHz for the broad structure and 350 Hz for the narrow peak. Note that the narrow peak is substantially narrower than the width of ~ 10 kHz expected from transit time broadening across the 4.5 mm beam. Control field intensity is 3.5 mW/cm^2 and cell temperature is 48 °C; hence the narrow EIT peak is subject to moderate power broadening.

Another addition to the setup is a second laser beam entering the cell alongside the control and signal field beam. This comes from a separate laser, and is used a repumper to depopulate inaccessible trapped ground states, as described below.

6.2 Slow light at two time scales

Zeeman EIT in coated vapor cells was discussed more fully in Chapter 5. Figure 6.2 shows another example of a measured dual-structure EIT lineshape, which consists of two distinct features: a broad pedestal due to atoms interacting with the laser beam only once, and a narrow central peak due to atoms returning to the beam after multiple bounces from the walls (and thus having a much longer coherence lifetime).

We explored slow light pulse propagation over a wide range of experimental parameters: field intensities between 1 and 60 mW/cm^2, cell temperatures from 50 to 75 °C, and pulse widths from 1 μs to 20 ms. See Figure 6.3.

We found two distinct regimes of maximum fractional pulse delay, corresponding

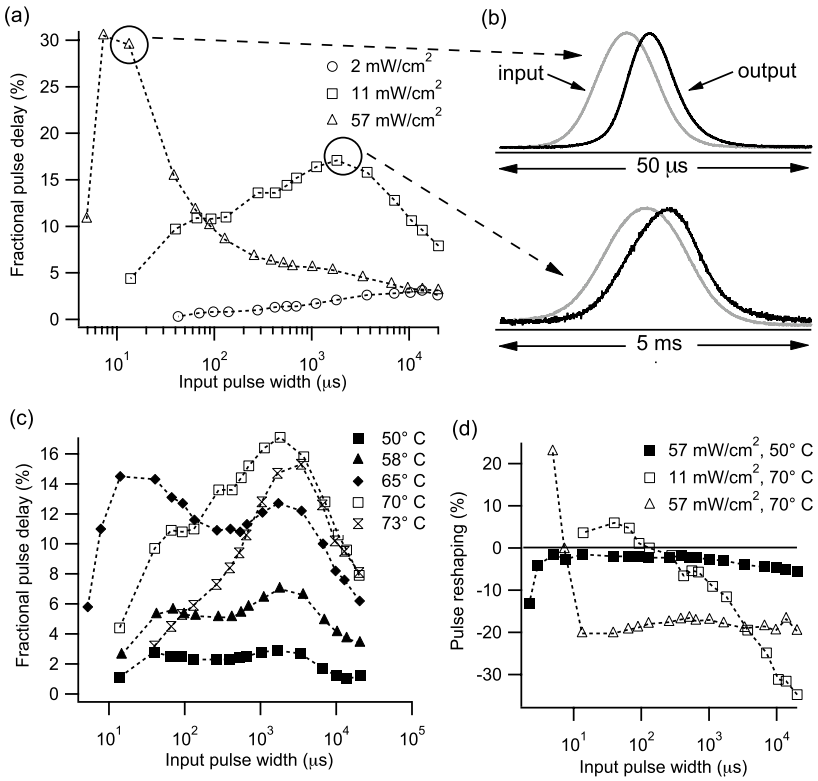

Figure 6.3: Fractional pulse delay as a function of input pulse width for (a) different laser intensities at constant cell temperature (70 °C) and (c) different cell temperatures at constant laser intensity (11 mW/cm^2). (b) Examples of slow light pulse propagation for two maximum fractional delay regimes. (d) Slow light pulse reshaping (*see text*). Beam diameter $\approx$ 2 mm.

to the two frequency scales observed in the dual-structured EIT lineshapes. At high laser intensity, many atoms are pumped into the dark state on a time scale comparable to the transit-time of an atom through the laser beam (as in an uncoated cell). This leads to an observed maximum fractional delay for pulse lengths near 10 μs [triangles in Figure 6.3(a)], corresponding to the broad EIT pedestal in Figure 6.2. At lower laser intensities [squares in Figure 6.3(a)], the maximal fractional delay is observed for much longer pulses with lengths of several ms. These pulses match the narrow central feature of the EIT resonance of Figure 6.2.

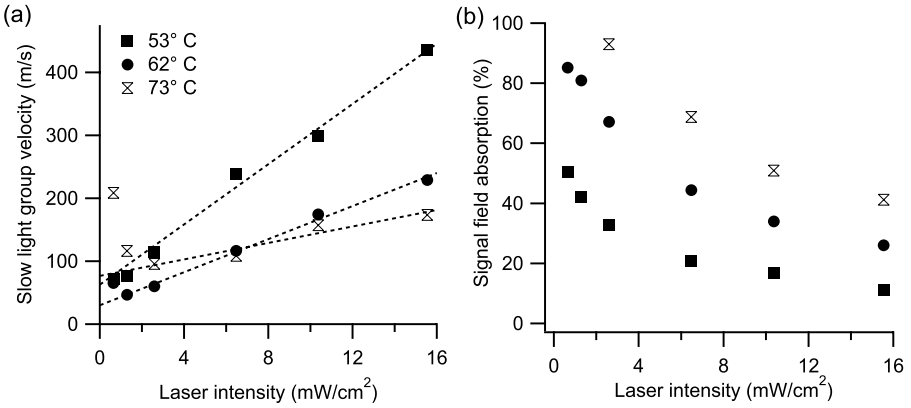

Figure 6.4: Dependence of (a) group velocity and (b) pulse absorption on control field intensity for different cell temperatures. Dashed lines indicate linear trending with control field intensity expected without radiation trapping.

Note that maximizing fractional delay in a coated cell requires both intermediate cell temperatures and laser intensities. Low laser intensity or temperature have small amounts of light-atom interaction and thus reduced slow light delay. High laser intensity leads to high population in the inaccessible $F = 1$ trapped states, while high temperature introduces incoherent pumping effects such as spin exchange and radiation trapping, and the latter is especially influential in coated cells where coherence fills the cell volume.

Naively, we expect broadening of output pulses (*i.e.*, narrowing of the frequency spectrum) when the pulse bandwidth is larger than the EIT spectral window [29]. However, in these measurements, we typically observe negative fractional pulse reshaping (defined as the difference of the input and output pulse widths, normalized to the input pulse width) as shown in Figure 6.3(d). We are currently studying this counterintuitive phenomenon in greater detail.

The maximum fractional pulse delays observed in these coated cells do not exceed 0.30. We believe that our observed delays are limited in part by radiation trapping, *i.e.,* the re-absorption of spontaneous, incoherent photons by the atomic medium [38, 39, 40].

Although fluorescence is suppressed by EIT, spontaneously emitted photons are still present due to residual absorption such as that from other excited state levels [30]. If an atom in the dark state absorbs an unpolarized photon, its coherence is destroyed. Thus radiation trapping effectively increases the ground state decoherence rate, leading to higher absorption, broader EIT linewidth, and shorter pulse delays. Motional averaging of atoms with ground state coherence throughout the vapor cell exacerbates the effects of radiation trapping in coated cells in comparison to buffer gas cells in which atoms participating in the slow light process are typically close to the axis of the cell.

For low-bandwidth pulses we expect the group velocity to be proportional to the control field intensity and inversely proportional to the atomic density [97, 1]. At low atomic densities for which most spontaneous photons are not reabsorbed [squares in Figure 6.4(a)] we observe such linear scaling of the group velocity with laser intensity. Similarly, at relatively high laser intensities, for which the additional decoherence due to radiation trapping is insignificant compared to the power-broadened EIT bandwidth, the measured group velocity scales inversely with atomic density [Figure 6.4(a)]. However, at low control field intensities and high densities the group velocity begins to increase [Figure 6.4(a)] as the absorption of the signal beam by the slow light medium becomes substantial [Figure 6.4(b)].

We have clearly shown in this section that the dual-structured EIT characteristic of coated cells can support slow light propagation through either of its transparency windows. The potential for high contrast (and therefore better fractional delay and transmission) is diminished at high densities by radiation trapping, and at high laser intensities due to trapped state optical pumping; the latter effect we can mitigate by using an additional repumping laser in the cell.

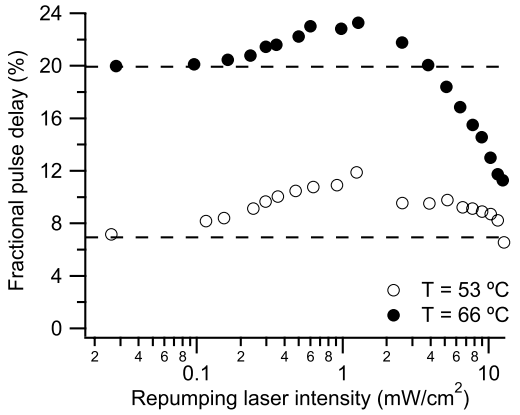

Figure 6.5: Slow light fractional delay vs. repumping laser power. Dashed horizontal lines show the fractional delay without repumping laser.

6.3 Repumping laser effect on EIT and slow light

By adding a repumping beam on the lower energy hyperfine level, we can increase the number of atoms interacting with the laser fields without increasing the atomic density. The repumper laser field depopulates the $F = 1$ hyperfine ground state by being resonant with the $F = 1 \rightarrow F' = 2$ transition and circularly polarized with the same polarization as the control field. At optimized repumping intensity, the fractional delay of a slow light pulse is increased (Figure 6.5); the fractional delay nearly doubles for low densities and therefore relatively low fractional delays (open circles in Figure 6.5). At higher densities and delays, however, the benefit of the repumping beam is less significant (solid circles in Figure 6.5).

The effect of the repumping field on a specific EIT lineshape is shown in Figure 6.6. The effective optical depth increases as the repumper depopulates the $F = 1$ trapped states, indicated by the lower off-resonant transmission. The peak transmission drops at the same time due to the increased absorption when more atoms are available to participate in EIT. The EIT linewidth is also reduced in the presence of the repumper, consistent with density narrowing. EIT contrast levels follow this behavior over a large range of input laser intensities

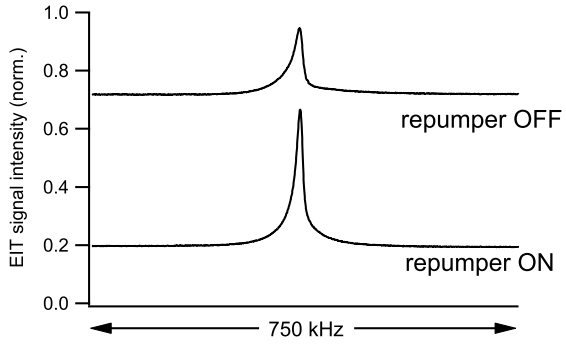

Figure 6.6: EIT lineshapes with and without the additional repumping laser field in the cell. The repumper acts to increase the effective optical depth, as evidenced by the much lower off-resonant transmission. Cell temperature is $T = 51$ °C, beam diameter $d = 18$ mm; control field power 2.3 mW, repumping field power 3.6 mW.

[Figure 6.7(a)], as the repumper maintains the effective optical depth even at high intensity. The initial dip in the EIT floor was explained in Section 3.4 and appears again here. The predicted effect on slow light performance indicates that the repumper should improve slow light the most at high laser power, even approaching the delay line criteria (fractional delay of 1 with transmission 0.5), as shown in Figure 6.7(b), which plots the predicted transmission (*i.e.*, q_{slow}) using the expression derived in Section 3.6. In practice the slow light pulses do not quite reach the predicted delays, in part because the EIT lineshapes in coated cells in the intermediate intensity regime are not Lorentzian (see Chapter 5), an assumption made in deriving the predicted transmission expression.

An examination of the temporal response of the medium to the repumping field turning on and off suggests a method to add to the benefit of the increased effective optical depth by timing the input slow light pulses to minimize the EIT transmission reduction effect. Figure 6.8 shows the recovery of the EIT contrast levels in the presence or absence of the repumping field. The repumping laser light was measured on a photodetector after the cell (gray trace in Figure 6.8), and the light was turned on or off after allowing the system

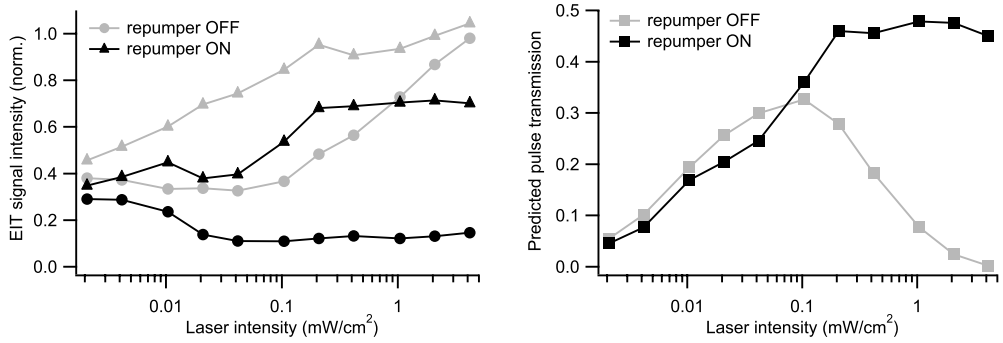

Figure 6.7: EIT contrast levels with and without the additional repumping laser. (a) Contrast levels, where the upper traces are the peak EIT transmissions $(F + A)$ and the lower traces are the off-two-photon resonance transmissions (F). The repumper increases the effective optical depth for a large range of laser intensities. (b) Predicted slow light pulse transmission for an input pulse with bandwidth chosen to achieve a fractional delay of 1. Cell temperature is $T = 51$ °C, beam diameter $d = 18$ mm. The repumping field power was chosen to maximize the effective optical depth while keeping amplitude reduction as small as possible.

to reach equilibrium transmission for the signal field. The short rise time in the repumper signal when the light is first turned on is due to the finite optical pumping rate as the field drives transitions from the $F = 1$ trapped states.

The peak transmission $(F + A)$ trace in Figure 6.8 was obtained by setting two-photon detuning to zero, and can be explained as follows. When the repumper turns off, the peak EIT transmission increases as atoms either absorb light and decay back into the $F = 1$ states (no longer participating), or atoms lose their coherence from repeated wall collisions and either absorb more light or end up in $F = 1$ due to the collision itself. When the repumper turns on there is a rapid influx of atoms from the $F = 1$ to $F = 2$ manifold, leading to a drop in EIT transmission; this occurs via spontaneous emission from the excited state, as the repumping field depopulates $F = 1$; given the short excited state decay time, this rapid drop happens at the optical pumping rate. However, as the control field optically pumps these atoms in $F = 2$ towards the $|F, m_F\rangle = |2, 2\rangle$ state, the absorption of the signal

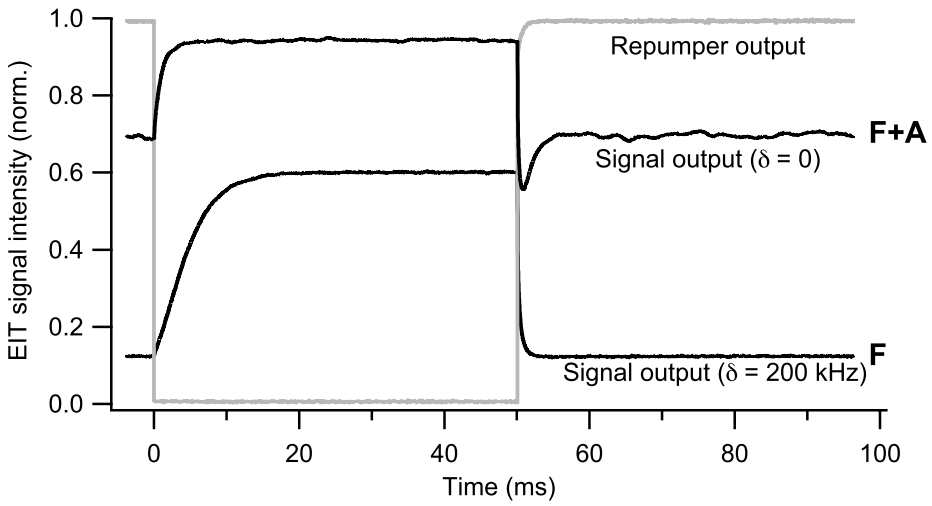

Figure 6.8: Response of the EIT contrast levels to the presence of absence of the repumping field over time. The peak transmission ($F + A$) and the off-resonant floor (F) both increase when the repumper is turned off (at time $t = 0$), but recover at different rates, leaving a range of times where we expect improved delay and transmission of slow light pulses. Noise in the EIT transmission output is from the laser.

field is reduced as EIT is established, causing the resonant transmission to increase again, at the two-photon pumping rate of the control field.

The off-resonant EIT floor (F) was also measured, with a two-photon detuning of 180 kHz applied via the magnetic field from the solenoid. This floor transmission is essentially a measure of the $|2, 2\rangle$ population. When the repumper turns off, atoms in the $|2, 2\rangle$ state can leave that state and end up in the $F = 1$ states, but the time scale is approximately the lifetime of the population of $|2, 2\rangle$. In coated cells, as we have seen, the lifetime is of order ms, much longer than the optical pumping times; hence the recovery time of the EIT floor is much slower than that of the EIT peak transmission. When the repumper turns on, more atoms quickly end up in the $|2, 2\rangle$ state, as atoms decay into $F = 2$ from the excited state, and are rapidly pumped to the highest m_F states by the control field. The

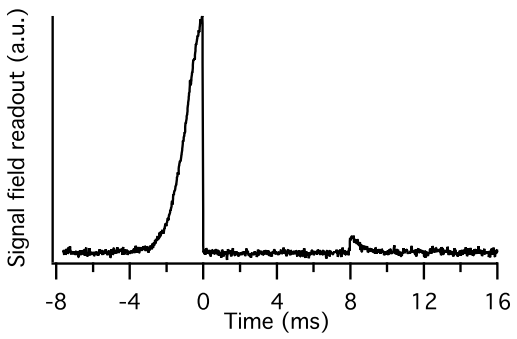

Figure 6.9: Demonstration of stored light in coated cells, achieving long time scale storage, but with limited efficiency. Pulses are sent through the ultra-narrow EIT feature, with storage time 8 ms after the control field is turned off. Cell temperature is $T = 65$ °C.

EIT floor responds at a rate related to the repumper field and control field pumping rates.

Putting all this together, there exists a window of time where the EIT floor remains low (high optical depth), but the EIT peak transmission has recovered to nearly its original value. In the example in Figure 6.8, this is roughly between 1 and 4 ms after the repumper turns off. Slow light pulses could be sent into the medium during this time interval, and benefit from the increased optical depth afforded by the repumper field but without the usual drop in transmission.

6.4 Coated cell stored light

We now turn to stored light experiments in our coated vapor cells. We have seen how the ultra-narrow EIT feature characteristic of such cells supports ultra-slow propagation of pulses whose bandwidth matches the narrow EIT feature, in addition to the standard slow light propagation based on the transit-time-based broad feature. Here we explore stored light using both time scales of input pulses, in both cases taking advantage of long coherence times allowed by the wall coating to observe long storage times.

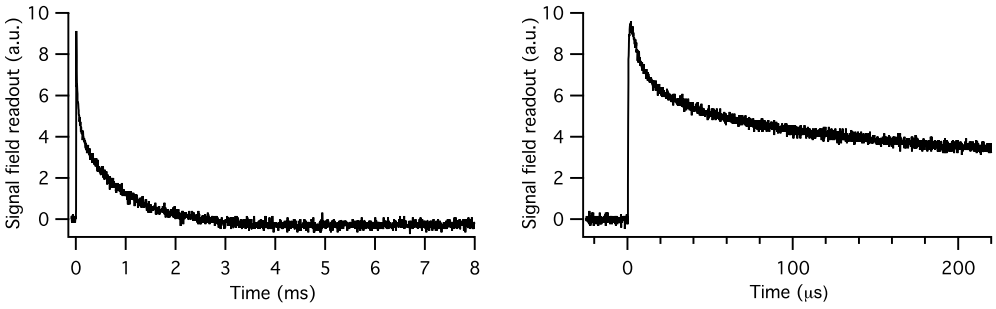

Figure 6.10: Signal field pulse readout typical of stored light in coated cells. Readout pulses are the same data, but shown at two different times scales. The short-time-scale readout (right) is from the control field reading out coherence present in the beam when it is turned back on, while the long-time-scale readout (left) occurs as atoms with coherence intact return to the beam after a number of collisions with the cell walls. Cell temperature is $T = 69$ °C with a control field power of 340 μW. The input pulse (not shown) had a temporal width of 3 ms.

A demonstration of long storage times for a pulse propagating via the narrow structure of coated cell EIT is shown in Figure 6.9. An input pulse of order ms in temporal width is stored for 8 ms, albeit with low readout efficiency. Low efficiency is due to a number of factors, many already discussed with the stored light work presented in Chapter 4. First, fractional delay is limited, as evidenced by the large pulse leakage observed before the storage interval, and the input pulse is partly absorbed, both leading to less light being stored even before the storage interval. Second, 8 ms is significantly longer than the $1/e$ decay time of coherence as measured in this cell, so the light that is stored decays. Third, a low readout control field power can limit readout efficiency as atoms in the dark state may pass through and leave the beam without having coherence read out, and can then lose this coherence before returning. And fourth, a small beam size has a similar detrimental effect, as dark state atoms take much longer to find the beam, and the interaction time when passing through the beam is short.

Examining the readout shape for stored light in coated cells further illustrates these

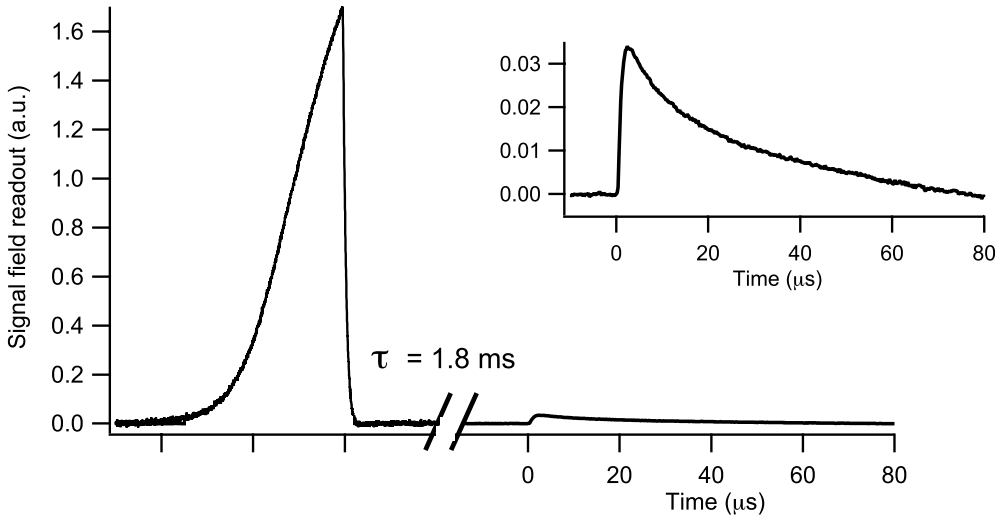

Figure 6.11: Demonstration of high-bandwidth pulse storage with a long storage time using a coated cell. The input pulse width is $\sim$ 15 μs, and the slow light fractional delay of the same pulse was 0.20. The long storage time supported by the wall-coating is more than 100 times the width of the input pulse. Cell temperature is $T = 51$ °C with a control field power of 4 mW and a repumper field power of 1.2 mW. *Inset*: Zoomed-in readout pulse.

efficiency issues. An example readout is shown in Figure 6.10. Just as EIT operates with two time scales, and slow light can propagate with two time scales of input pulse widths, stored light readout also occurs at two time scales. During the short time scale, in this case of order 10 μs, dark state atoms already in the beam have their coherence read out and transported out of the cell via slow light propagation; during the long time scale, dark state atoms originally elsewhere in the cell enter the beam, and their coherence is read out on the time scale of order ms, the coherence lifetimes allowed by the wall coating. Readout with a more powerful control field and a larger beam should increase the amount of light recovered after the storage interval.

As proposed at the end of Chapter 5, we can also perform stored light experiments with high-bandwidth input pulses that propagate through the broad EIT structure, while

still utilizing the long coherence lifetime allowed by the coating during storage. An example is shown in Figure 6.11. The overall stored light efficiency is not high (around $\eta = 1\%$), but the method appears promising after careful consideration. The EIT contrast levels were $F = 0.10, A = 0.48, C = 0.42$ with the repumper on, and the fractional delay of the same input pulse was 20%; this means less than 10% of the input pulse was stored in the medium. This included using the repumper timing scheme discussed above (the pulse sent 2 ms after the repumper turns off). The long storage time and limited beam size (9 mm diameter, where the cell diameter is 25 mm) explains the remaining loss. It should be noted however, that the storage time is more than 100 times greater than the input pulse width, so the input and output pulses are extremely well separated. Upgrades to the experimental setup can likely make this technique viable as a tool for high-bandwidth pulse storage.

High-efficiency readout of the stored pulse should occur with a large beam and higher control field in the readout stage.

Measurements of storage readout area vs. control field power have confirmed that the readout area will saturate with power, provided the detection is sufficiently fast. The readout area also increases with beam size, and is maximized when the beam size is near the size of the cell. The primary overall efficiency issue is in the delay and transmission of slow light pulses, and by implication the off-resonant floor (effective optical depth) and peak transmission of EIT spectra. Several experimental improvements should help here too. A larger beam should provide higher contrast for the broad structure, especially if aided by a strong repumping field; this would require more laser power than currently available in the experiment. A reasonable estimate is to have a readout control field power 3 times greater than that used for the input, so a but 150 mW of laser power at the vapor cell entrance with a beam of diameter of 24 mm should be sufficient.

A final improvement could be in the coated cell itself, in several respects: (i)

better wall coating means a lower ground state decoherence rate γ_{12}, leading to higher peak transmission, as well as cutting the loss rate during the storage interval; (ii) a narrower cell geometry to reduce the transverse optical depth and thus mitigate radiation trapping (note that this would itself require better coating quality to reach the same coherence lifetime of a larger cell); (iii) isotopically enriched ^{87}Rb instead of natural abundance Rb, allowing for higher atomic density at lower temperature. This last change becomes especially relevant if (i), (ii), and the input laser power are such that operation at high temperatures becomes feasible; the wall coating melts at around 80 °C, and enriched Rb would provide a factor of 4 increase in optical depth for the same temperature.

In this chapter we have demonstrated both slow and stored light in coated vapor cells, taking advantage of the unique properties of EIT in coated cells to achieve long-time-scale pulse delay, including for high-bandwidth input pulses as discussed above. Realistic improvements to the experimental setup provide the potential to make this storage method viable for optical communication or quantum optics applications. Even with the current apparatus, an important demonstration of such an application can be made: the "slow light beamsplitter," which is the topic of the next chapter.

Chapter 7

A Slow Light Beamsplitter

7.1 Introduction

Armed with understanding of the physics of EIT and slow light in atomic vapor cells, and in paraffin-coated cells in particular, we are in a position to exploit its properties in a demonstration of a novel slow light application: the slow light beamsplitter.

In this chapter we report the demonstration of a dynamically controllable beamsplitter using slow light and rapid transport of atomic coherence in a coated cell. Recall from Chapter 1 that EIT-based effects work by putting atoms into dark states, coherent superpositions of energy ground states. In warm atomic ensembles, these internal degrees of freedom (spin states) of atoms are effectively decoupled from their external (motional) degrees of freedom. We exploit this decoupling to split an input optical signal field into two spatially separated output signals by (i) writing coherence into an atomic medium at one transverse position with a control field using EIT, (ii) letting atomic motion distribute this coherence throughout the cell, which can occur quickly in buffer-gas-free coated cells, and (iii) reading out two slow light signals at both the original location and a second transverse location set by a second control field (see Fig. 7.1 and Fig. 7.2). Transport of coherence

between channels at rates faster than the rate of change of the internal atomic state distinguishes this scheme from previous experimental work [98, 99, 100, 101] and other EIT proposals related to light splitting [102, 103].

A key result is the demonstration that even particles undergoing random and undirected classical motion can mediate coherent interactions between two or more quantum states. This is relevant to a range of fields not only for its potential uses, but also as a demonstration of a widely applicable concept. The slow light beamsplitter may be useful in both classical and quantum information processing, *e.g.*, as an all-optical dynamically-reconfigurable router and for the efficient production of entanglement for quantum repeaters [2].

We realize rapid transport of coherence using the paraffin-coated Rb vapor cell described in Chapter 2, and used in Zeeman EIT and slow light experiments in Chapters 5 and 6. This enables atoms to undergo many wall collisions without destroying their internal state, thus enhancing the coherence lifetime and narrowing ground state linewidths. As noted in earlier chapters, coated cells have been used successfully in atomic clocks [104, 105], magnetometers [34, 92], slow light [18, 89], and squeezing and entanglement generation [82, 106, 107].

EIT results from optical pumping of an atomic ensemble into a noninteracting collective "dark state" for two optical fields (the signal and control fields) in two-photon Raman resonance with a pair of long-lived ground states of the atomic system [15]. A weak signal field propagates with very slow group velocity (slow light [16]) due to a nearly adiabatic transfer of the input photonic excitation to a combined excitation of photons and collective spin coherence known as a "dark-state polariton" [19, 20].

As discussed in Chapter 5, EIT line shapes in coated cells exhibit a dual structure: a narrow peak on top of a broad pedestal [89, 77]. The broad pedestal arises from the

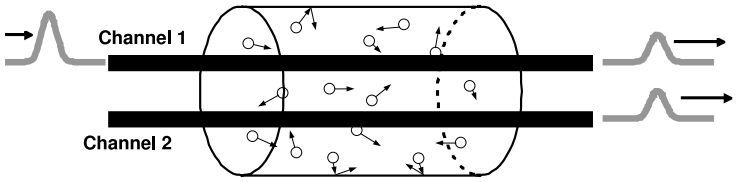

Figure 7.1: Schematic of slow light beamsplitter operation. An optical signal pulse enters an atomic EIT medium in Channel 1 together with a strong optical control field. Rapid atomic motion in a wall-coated cell with no buffer gas distributes atomic coherence throughout the medium. Output optical signal pulses leave the medium in both Channel 1 and a spatially-separated Channel 2 defined by the position of a second control field. The propagation direction of the two control fields, and hence the two output signal pulses, need not be the same.

single pass, transit-time-limited interaction of atoms moving ballistically through the laser beam. The narrow peak forms in the weak laser intensity limit in which atoms undergo little evolution of their internal state between velocity-changing wall collisions (the Dicke regime [79, 108]). The atoms experience a Doppler-free, averaged laser field with long interaction time, resulting in a narrow EIT linewidth determined by decoherence from wall collisions, spin-exchange, magnetic field gradients, etc. A quantitative description of coated-cell EIT is provided by the repeated Ramsey sequence model [59, 60, 77]. High contrast of the narrow EIT feature allows slow light pulses with bandwidths comparable to the narrow peak linewidth to propagate in the presence of rapid transport of coherence throughout the cell, thereby enabling slow light beamsplitter operation. As in Chapter 5, the contrast of the narrow EIT feature depends on cell/beam geometry and the strength of the input light fields. Thus the properties of the slow light beamsplitter can be controlled by balancing interaction time, time outside the laser beam, and power broadening by adjusting the laser intensity and beam size.

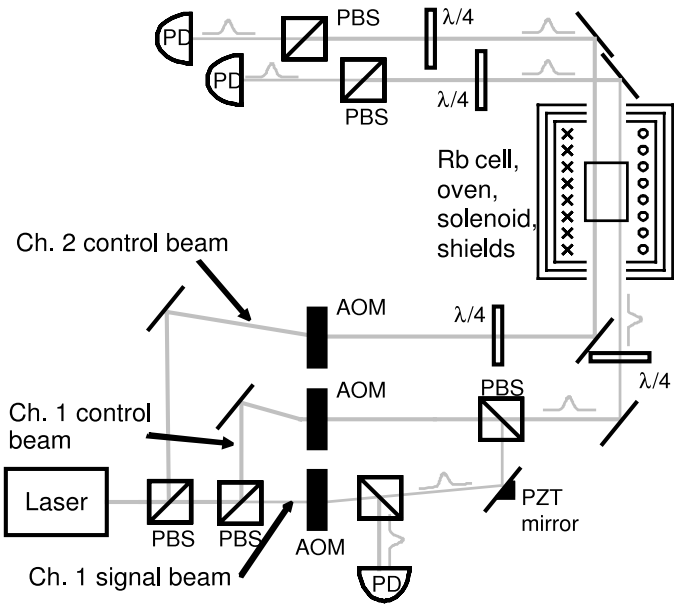

Figure 7.2: Schematic of the apparatus used in the coated cell slow light beamsplitter experiments. *(See text for details).*

7.2 Experimental Setup

We used the experimental apparatus shown schematically in Figure 7.2 to demonstrate the slow light beamsplitter. This is similar to the dual-AOM Zeeman EIT configuration described in Chapter 2, but with the addition of a third light field, which is used to read out the signal field pulse at a new location. As before, the laser operated at the ^{87}Rb D_1 line, but here was spatially split into three beams using half-wave plates (not shown) and polarizing beam splitters (PBS): orthogonally polarized input signal and control beams were recombined and sent into Channel 1 (Ch. 1), while the second control beam was sent into Channel 2 (Ch. 2) at a different transverse location in the Rb vapor cell (see Figures 7.1 and 7.2). The signal and control fields formed an EIT Λ-system between the two ground electronic state Zeeman sublevels $|F = 2, m_F = 0\rangle$ and $|F = 2, m_F = 2\rangle$, and an excited state $|F' = 1, m_{F'} = 1\rangle$ (other Λ-systems also participate, but this is the dominant one;

see Figure 2.9). Acousto-optic modulators (AOMs) provided independent intensity control for the optical fields. The two AOMs controlling the signal and control fields of Ch. 1 were driven from the same oscillator to stabilize their phase relationship. The input signal beam was reflected off a PZT-controlled mirror to adjust its path length and thus its phase relative to the Ch. 1 control field. All three laser beams were 3 mm in diameter, and the transverse separation between the centers of the two channels was 8 mm. At the cell output, PBS cubes transmitted only the signal field light in each channel to the photodetectors (PD).

The vapor cell (see Section 2.3 and Appendix A) was heated to approximately 65 °C by the blown air plastic oven, housed inside the high-permeability magnetic shielding. The solenoid between the oven and magnetic shields generated a uniform magnetic field used to adjust the two-photon detuning. EIT line shapes were measured by sweeping the magnetic field while observing the output cw signal light in each channel. Slow light pulses were shaped using the signal field beam's AOM, with a small part picked off as a reference for measuring pulse delay through the atomic medium.

7.3 Steady-state operation

To demonstrate steady-state operation of the slow light beamsplitter, constant intensity signal and control fields were sent into Ch. 1, for the two cases of the Ch. 2 control field on and off. The simplest demonstration is to use the coated cell as a beamsplitter for cw input fields on EIT resonance. This is shown in Figure 7.3, with signal field light showing up in both Ch. 1 and Ch. 2 when the Ch. 2 control field is turned on.

Figure 7.4(a) shows coherent transfer of the EIT lineshape by monitoring the detected output signal in both channels as the two-photon detuning was swept slowly. A strong Ch. 1 control field was used in this example so that both the broad and narrow EIT

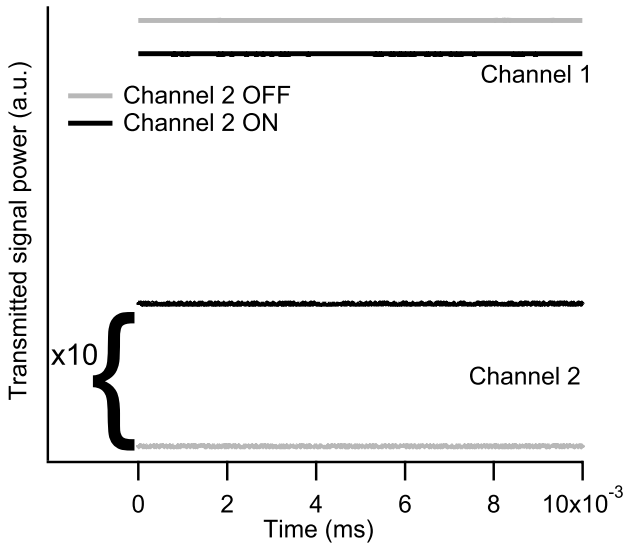

Figure 7.3: Simple demonstration of beamsplitter operation. Input signal field light is transferred into Ch. 2 as coherence is read out by the Ch. 2 control field; and this transfer occurs at the expense of the signal field output in Ch. 1. With the Ch. 2 control field off (gray lines), no signal field light shows up in Ch. 2.

lineshape features described above could be observed [89, 77]. With no control field in Ch. 2, EIT was only visible in Ch. 1; with the Ch. 2 control field on, an EIT signal also appeared in Ch. 2, and the medium acted as a steady-state beamsplitter.

Note that the broad pedestal of the coated cell EIT lineshape does *not* transfer into Ch. 2, because coherence associated with the broad structure dephases on a time scale short compared to the time to reach the second channel. The signal transfer efficiency between channels is limited by the finite fraction of atoms that repeatedly cross the Ch. 2 laser beam with sufficiently small longitudinal velocity to establish good coupling to the Ch. 2 control field during the finite coherence time. With a larger filling fraction for the laser beams in the cell and/or improved wall coatings, such that decoherence is reduced by ~ 100, we estimate that the signal transfer efficiency would be of order unity. We also observed a decrease in the Ch. 1 EIT amplitude when the Ch. 2 control field is on, due to partial read-out in Ch. 2

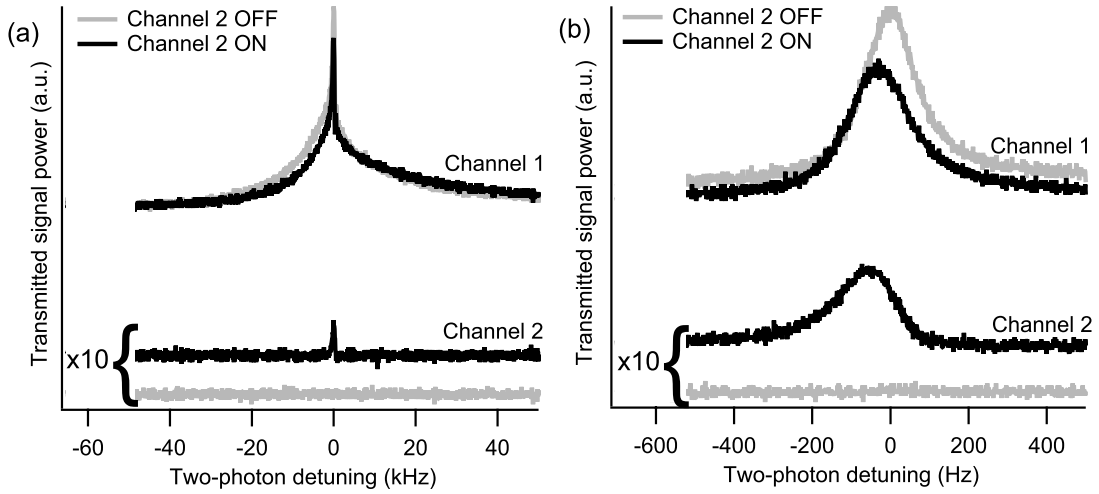

Figure 7.4: Example measurements of EIT spectra in Chs. 1 and 2, demonstrating steady-state beamsplitter operation. (a) Both the broad pedestal and narrow peak of the coated-cell EIT lineshape are visible in the Ch. 1 output with large Ch. 1 input control power of 600 μW. Only the narrow EIT structure is observed in Ch. 2 with the Ch. 2 control field on, because coherence associated with the broad pedestal dephases before it is transfered from Ch. 1 to Ch. 2. Ch. 1 input signal power of 9 μW; Ch. 2 input control power of 150 μW. (b) Only the narrow EIT lineshape structure is visible with weak Ch. 1 control power of 270 μW and other parameters as in (a). Note: frequency range $\simeq$ 100-times smaller than in (a). (For both plots: linear scales for power; Ch. 2 background from control field leakage due to finite extinction ratio of PBS).

of the finite atomic coherence in the cell and increased optical pumping; and also a shift of the Ch. 1 EIT resonance center frequency when the Ch. 2 control field is on, due to an increase in the ac Stark shift of the EIT resonance, proportional to the total control field power in the cell (in both Ch. 1 and 2). Figure 7.4(b) illustrates this behavior for relatively weak control fields, so that the EIT lineshape is dominated by the narrow structure [89].

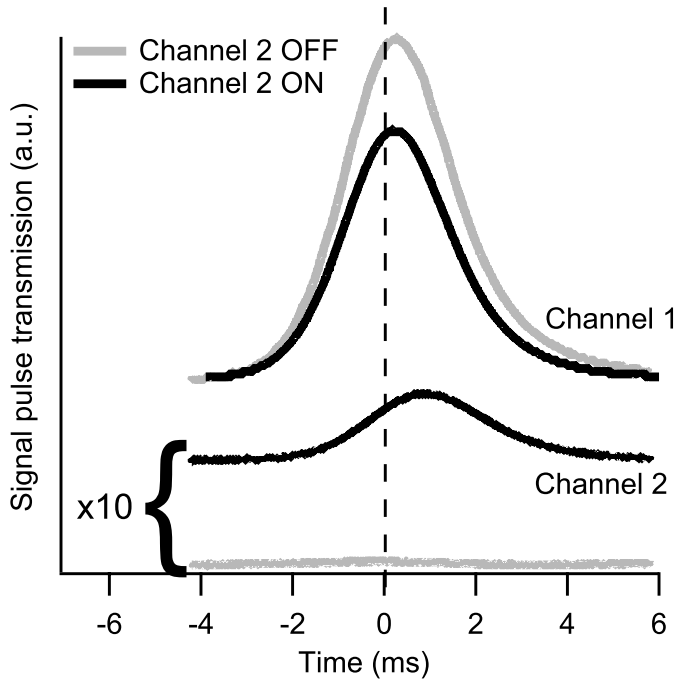

Figure 7.5: Primary demonstration of the slow light beamsplitter in pulsed operation. Signal field pulses detected from each channel. With the Ch. 2 control field on, a slow light pulse is read out in both channels. Input powers: Ch. 1 control 270 μW, peak signal 9 μW, Ch. 2 control 150 μW.

7.4 Pulsed operation: the slow light beamsplitter

To demonstrate pulsed operation of the slow light beamsplitter, a constant control field and a pulsed input signal field were sent into Ch. 1, again for the two cases of constant Ch. 2 control field on and off. Figure 7.5 shows examples of output signal pulses observed in both channels at the same time. An output signal pulse in Ch. 2 is not present with the Ch. 2 control field off, since there is no field present to read out the coherence. There is no output signal field in Ch. 2 if the Ch. 1 control field is off either (see Figure 7.6), an important fact to establish, as it more rigorously demonstrates that the signal field pulse in Ch. 2 does not arise simply from leakage of the Ch. 1 control field into the location of the Ch. 2 beam. The output pulse in Ch. 2 legitimately comes from the transferred coherence

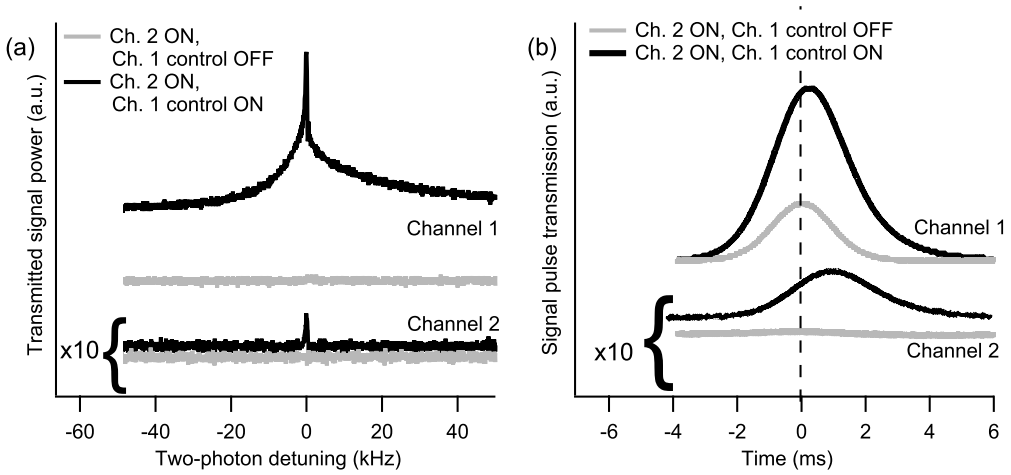

Figure 7.6: Direct evidence that the slow light beamsplitter really does transfer the signal field pulse, and that it is not due to leakage from the Ch. 1 input into Ch. 2. Signal field light only appears in Ch. 2 when both control fields are turned on. Ch. 1 control power is 270 μW, Ch. 1 signal power is 9 μW, and Ch. 2 power is 150 μW. Note that an un-slowed signal field pulse still appears in Ch. 1 because it is not completely absorbed (optical depth is finite).

generated in Ch. 1.

In the same way that the broad feature of the dual-structured EIT was shown not to transfer to Ch. 2 in Figure 7.4, high-bandwidth pulses do not transfer either. This is demonstrated clearly in Figure 7.7, which has conditions identical to the successful pulse splitting from Figure 7.5 except for the time scale. The signal field pulse is still delayed (time $t = 0$ is marks the center of the input reference pulse), but due to the dispersion slope from the broad EIT feature.

The time it takes for atoms carrying coherence to propagate effusively from Ch. 1 to Ch. 2 accounts for the relative delay between output slow light signal field pulses in the two channels. The delay in each channel as a function of the power in Ch. 2 is shown in Figure 7.8. This could be a useful beamsplitter feature: since the pulse delay in Ch. 1 varies little with Ch. 2 power, the delay in each channel could be controlled by adjusting the two

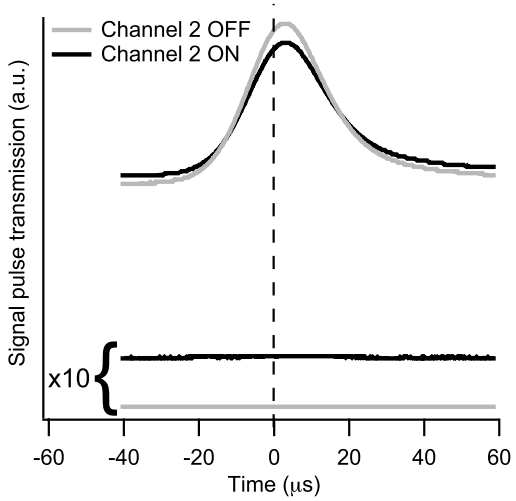

Figure 7.7: The slow light beamsplitter fails to transfer an input signal field pulse when the pulse does not fit inside the narrow feature of the dual-structured EIT, even if it is slowed due to the broad structure EIT. Ch. 1 control power is 600 μW and Ch. 2 power is 150 μW and Ch. 1 signal power is 9 μW

control field powers.

The slow light beamsplitter is also tunable: the area (*i.e.*, energy) of the signal pulse that is transferred from Ch. 1 to Ch. 2 can be varied by changing the laser power in either control field. Figure 7.9 shows the Ch. 2 signal pulse area as a function of Ch. 2 control field power for three different Ch. 1 control field powers. With increasing Ch. 2 control power, the generated signal field pulse area first grows because entering coherence is more efficiently read out; it then drops when the Ch. 2 control field performs significant optical pumping of atoms in a single beam crossing, destroying the atomic coherence and leading to increased absorption. The optimal Ch. 2 control power also depends on the Ch. 1 control power: for a weak Ch. 1 control field, even low Ch. 2 control power will optically pump atoms out of the dark state; for sufficiently high Ch. 1 control power, the benefit of more efficient Ch. 2 readout saturates (when the atom-light interaction is strong enough to read out atomic coherence in a single trip through the Ch. 2 beam), and the optimal Ch. 2

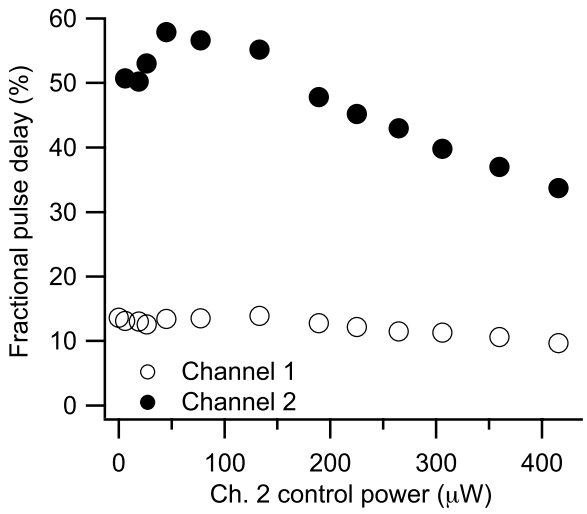

Figure 7.8: Extra delay in Ch. 2 compared to Ch. 1. Ch. 1 control power is 270 μW and Ch. 1 signal power is 9 μW

control power becomes independent of the specific Ch. 1 power.

7.5 Phase coherence demonstration

Signal transport between beamsplitter channels is phase coherent, due to rapid atomic motion in the wall-coated cell. Thus the phase difference between the output signal and control fields in Ch. 2 is determined by the phase difference between the input signal and control fields in Ch. 1.

We demonstrated this phase coherence between the two channels by adding half-wave plates at the output of each channel to intentionally mix a small part of the corresponding control field into the detected output signal. The resulting interference between the signal and control fields at each PD made the detected amplitudes depend directly on the signal/control phase difference in each channel [23]. Figure 7.10 shows that the measured output in both channels vary nearly identically as the phase difference between the input

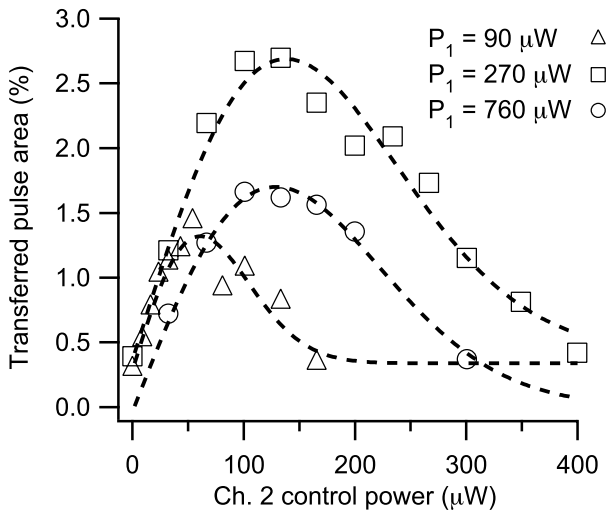

Figure 7.9: Tunable slow light beamsplitter. Transferred pulse percentage (area of Ch. 2 pulse normalized to the area of Ch. 1 pulse without Ch. 2 light) can be optimized as a function of Ch. 2 power for fixed Ch. 1 powers.

signal and control fields in Ch. 1 is scanned by nearly 2π using the PZT mounted mirror (see Figure 7.2).

Note that a conventional beamsplitter imparts a $+\pi/2$ phase shift to signals transfered between channels. This $+\pi/2$ phase shift could be realized in the slow light beamsplitter by applying a two-photon detuning to atoms moving outside the two control field regions, e.g., with an off-resonant laser field. Simulations indicate that such a phase shift will also enable maximally efficient mapping of the input signal pulse into two output pulses while exhibiting standard beamsplitter statistics [63].

7.6 Further ideas

In conclusion, we demonstrated a tunable slow light beamsplitter that operates by using rapid transport of atomic coherence in a wall-coated vapor cell. Once optimized, the slow light beamsplitter may be used to improve quantum repeater performance and

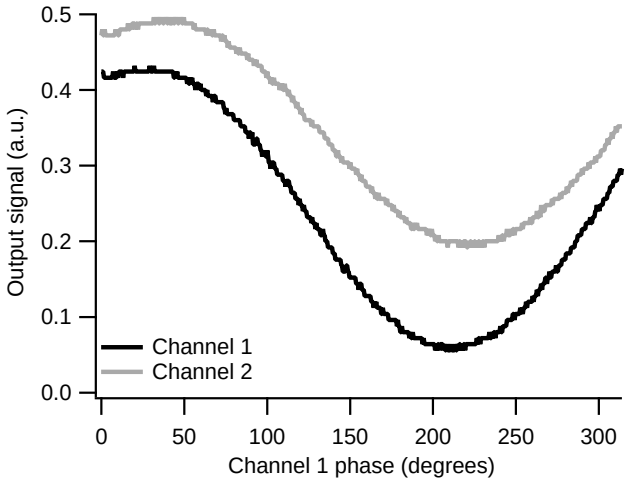

Figure 7.10: Demonstration of phase coherent signal transport in the slow light beamsplitter. For each channel, a small part of the control field is interfered with the signal field at the photodetectors such that the output signal amplitude is a measure of the phase difference between the signal and control fields. Near identical variation is observed in the two channel outputs as the phase difference between the input signal and control fields in Ch. 1 is scanned by nearly 2π. Vertical offset in Ch. 1 and Ch. 2 output signals is caused by slightly different control field admixtures. Ch. 1 and Ch. 2 control fields 160 μW. Input Ch. 1 probe field 13 μW.

generate nonclassical photon states. This approach could succeed even for short repeater memory times [109] provided that the beamsplitter interferes photons from channels with entanglement in less than the memory storage time of a repeater node.

The slow light beamsplitter could also increase the efficiency with which maximally-entangled N-photon states can be generated from probabilistic single photon sources (each with generation efficiency η). An M-port ($M > N/\eta$) slow light beamsplitter could replace a symmetric N-port fiber coupler [110]. The increased number of single-photon sources would ensure that more than N photons are generated each cycle, while the dynamic reconfigurability of the beamsplitter allows us to activate (and thus interfere) only those channels which contain single photons. For $N = 1, 2$, this may also have application to generating inputs for quantum computation schemes based on linear optics [111].

The slow light beamsplitter may also have applications in classical telecommunications: *e.g.*, as an optical buffer with adjustable multi-port output. Here, orthogonal linearly polarized light could be used for the signal and control fields, in order to enhance transport efficiency in both channels via self-rotation induced gain [112]. Potential realizations in other media include ions and atoms in traps, and atoms in hollow core fibers [113] where precise control over the (largely classical) motion of the mediating atomic ensemble would be difficult or impossible.

The key result of this work is the demonstration that even particles undergoing random and undirected classical motion can mediate coherent interactions between two or more modes. This work, then, is relevant to a range of fields not only because of the potential uses of the coated-cell beamsplitter, but also as a demonstration of a widely applicable concept.

Chapter 8

Conclusion

This thesis has presented a wide variety of experimental findings related to EIT, slow, and stored light in atomic vapor cells. At the outset, we claimed that vapor cells could be considered an ideal playground for exploring the potential and limitations of light storage using EIT. Cells with a range of shapes (*e.g.*, the long cells used in Chapters 3 and 4) and sizes (*e.g.*, the miniature cells in Chapter 5) were employed, with slow light propagating through the optically thick and thin.

In Chapter 3 we developed a practical tool for predicting dynamic slow light pulse delay from easily measured static EIT parameters, and verified it experimentally. We also derived an expression for a slow light figure of merit that gives the predicted transmission of a pulse traveling with a 100% fractional delay. Both these tools, we expect, should be useful in any EIT-based system, not limited to vapor cells, and will provide a useful method of searching for optimal slow and stored light conditions.

The vacuum cell results of Chapter 2 introduced the complicated role that optical depth plays in slow and stored light experiments, and led into the more detailed treatment of optical depth in buffer gas cell stored light experiments in Chapter 4. Here we found

that increasing optical depth (by raising cell temperature) ceased to benefit stored light efficiency and eventually negatively affected it. By direct and implicit measurement we established radiation trapping as a major deterrent to high efficiency stored light at high optical depth, and also showed a way to mitigate its effect by a difference choice of cell geometry. This demonstrates the general point (not limited to vapor cells) that the size and shape of the atomic medium are important in determining the slow light propagation. We also noted that choice of buffer gas in the cell strongly affects the trapped state optical pumping phenomenon, whereby atoms are optically pumped into inaccessible trapped states at high laser intensity. Due to rapid excited state mixing, Ne buffer gas allows higher effective optical depths. This result is relevant to many systems that use buffer gas, not limited to slow and stored light applications, including atomic clocks where the effective optical depth helps determine lineshape contrast and thus the clock stability.

Tetracontane-coated vapor cells were used in the remainder of the work. Chapter 5 explained EIT in coated cells, described and modeled using a Ramsey pulse sequence picture, highlighting the dual-structured nature of EIT lineshapes, with a broad feature arising from transit time of atoms through the laser beam, and an ultra-narrow feature from high sensitivity to phase evolution of dark state atoms outside the beam. We noted the peculiar dependence of coated cell EIT on laser intensity and beam geometry, and the relevance of these dependences to various applications.

We also demonstrated hyperfine EIT, slow, and stored light in a coated cell, the first such measurements reported. Hyperfine EIT without buffer gas confinement dictated a unique cell geometry in the miniature coated cell. Despite its size, EIT contrast levels were competitive with the results in buffer gas cells and standard-sized coated cells. The small cell size is also a promising feature, as the miniaturization of vapor cell experiments has application towards small clocks, magnetometers, quantum information and communication

components, etc. With an improved optical pumping scheme, such as by the addition of a repumping laser into the miniature cell, the high-quality coating could better be utilized, pointing toward the potential use of a miniature cell device.

Long-time-scale slow and stored light (Chapter 6) were observed in coated cells under the Zeeman EIT configuration. Using the narrow structure for propagating slow light pulses does lead to long absolute delay times and long-time-scale storage, but at generally low efficiencies due to pulse absorption, limited fractional delay, and limited readout capability. Adding a repumping light field to depopulate inaccessible trapped states increased the number of usable atoms (effective optical depth, and thus the fractional pulse delay); and, due to an improved timing scheme for pulse propagation, with minimal extra absorption. Slow light propagating under these conditions did come close to meeting the delay line criteria for photonics applications (fractional delay of 1.0 with a transmission of ~ 0.35), and we believe with some improvements to the setup, the delay line conditions could be met in vapor cell systems. Combining the repumper field with the idea to send slow light pulses through the broad EIT structure, while using long storage times afforded by the coating, we observed a dramatic storage demonstration where a pulse was stored for more than 100 times its own temporal input width. With appropriate improvements to the experimental setup (longer coherence times from coating, larger beam, more laser power), we believe the efficiency of this technique could be made much higher.

Finally, in Chapter 7, we demonstrated a novel application of coated cell slow light. The "slow light beamsplitter" was able to rapidly transport coherence from an input pulse in one beam into a second beam spatially separated by 8 mm, while maintaining the phase coherence of the of the pulse. The beamsplitter was also shown to be tunable by suitably adjusting the control field powers in the two channels. This was an initial demonstration of a potentially useful tool, which could be configured as a multi-port adjustable router of

quantum information.

Overall, these experiments have not only shown that atomic vapor cells are useful tools for understanding slow and stored light, but have demonstrated a number of promising avenues for future applications of atomic vapor cell EIT.

Appendix A

Coated Cell Construction

This appendix describe techniques for constructing vapor cells used in the experiments described in this thesis. Most cells described here are coated on the inside with paraffin. As described in Chapters 2 and 5, this allows atoms to maintain their coherent ground-state superposition states during wall collisions, and leads to long-time-scale EIT and slow light behavior.

Vapor cell coatings have been investigated for over 50 years utilizing various techniques and derivatives of paraffin as a coating material [32, 33, 31]. Presently, we employ a technique similar to Alley and co-workers [114] for our cylindrical cell geometry. (Previous work in this laboratory [115] used techniques similar to those described by Bouchiat [31], which was more appropriate to spherical vapor cells). Following Robinson [26], we coat with tetracontane ($C_{40}H_{82}$), a readily available component of paraffin.

The appendix is organized as follows. Section A.1 explains in detail the various steps required for constructing coated Rb cells, including initial preparation, coating techniques, and Rb distillation. In Section A.2 we describe how the cells are tested afterwards, using either EIT linewidth or Zeeman double resonance linewidth measurements. These

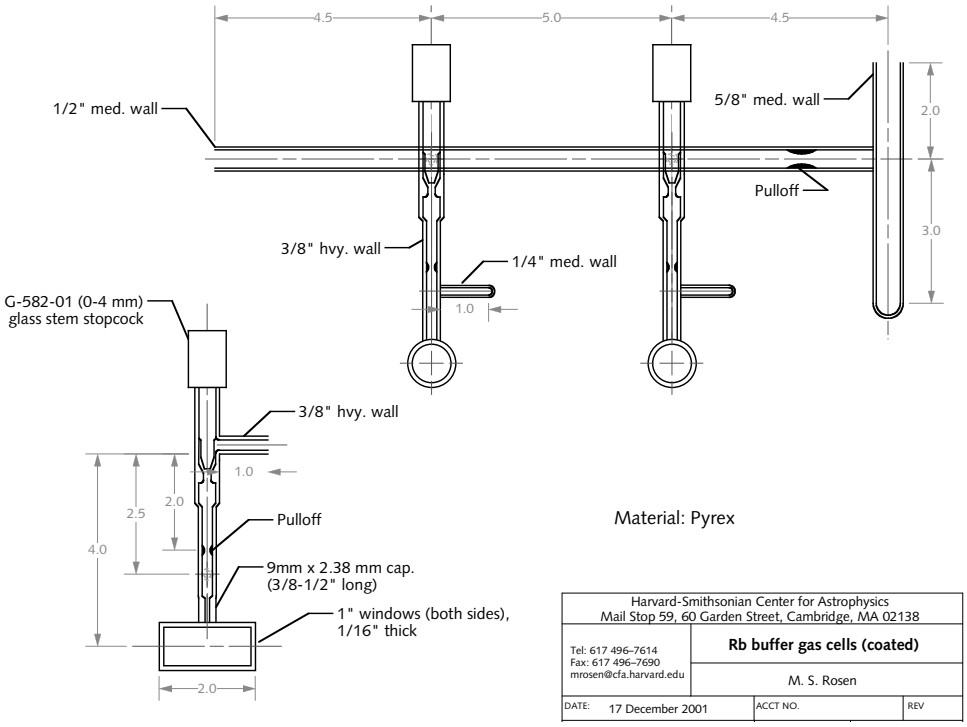

Figure A.1: Design of a typical manifold used for making paraffin-coated Rb vapor cells. All dimensions are in inches. Original design by M. S. Rosen, 2001.

measurements are shown directly for the coated cell used in the Zeeman-EIT-based experiments of Chapters 5, 6, and 7. Section A.3 concludes with a list of cells made from 2004 to 2008, highlighting the successes and suppressing the failures of various cell designs and coating techniques.

A.1 Aspects of coated cell construction

Cells begin attached to a larger manifold designed for the delivery of paraffin coating and Rb metal into the cell. A typical manifold design is shown in Figure A.1, and schematically illustrated in Figure A.2. Both the cell and manifold are made of Pyrex, well suited for glass-blowing. Valves make seals using rubber o-rings against the glass.

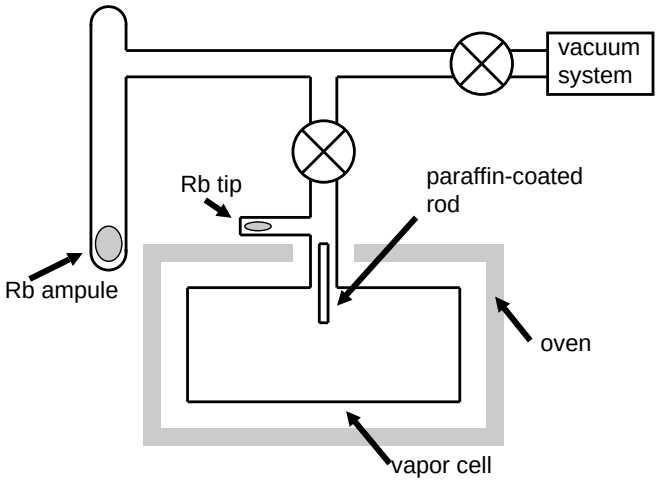

Figure A.2: Schematic of the Pyrex manifold and vacuum system used to apply paraffin coating to the inside of the cell *See text.*

Checking the cell and manifold for leaks is an important first step, as even commercially purchased cells can be insufficiently sealed (such as the miniature cells from Opthos Instruments, see below). The background gas pressure in the final cells should be below 10^{-6} torr. Leak checking for the cells described in this appendix was done with a helium mass spectrometer device. The manifold is connected to the leak checker and the gas inside is actively pumped away. Helium is then sprayed lightly around the outside of the manifold, while the mass-spectrometer's response is monitored; cell windows and joints in the manifold are likely candidates for leak locations. To further isolate the leak location, the suspected area can be sealed with a plastic bag with a small hole for the helium; the leak is confirmed by stronger and more rapid mass spectrometer response. Leaks can sometimes be repaired by adding melted glass, but this is often insufficient, especially if changes must be made to the cell walls, and melting glass near or on the cell windows can lead to optical distortion in experiments.

Cleaning the cells and manifold is done with "piranha" solution, a mixture of sulfuric

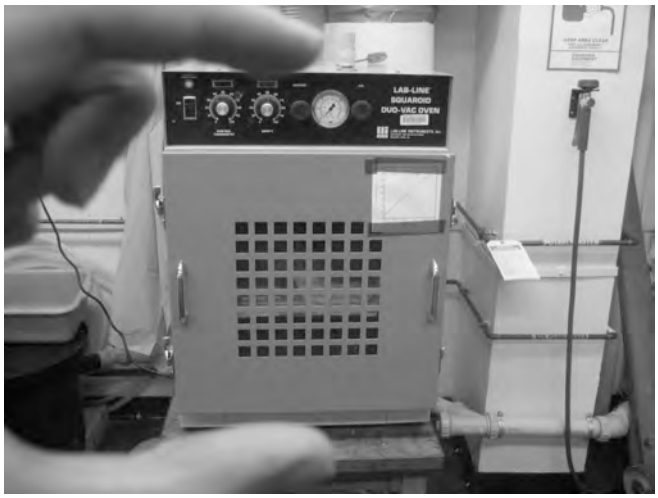

Figure A.3: Squaroid vacuum oven used to bake out cell manifolds after cleaning and before adding Rb. The oven is ~ 70 cm tall.

acid (H_2SO_4) and hydrogen peroxide (H_2O_2), typically a $3:1$ volume ratio of sulfuric acid to 30% hydrogen peroxide solution. The peroxide should be added to the acid. The reaction is exothermic and the solution temperature can rise to over 100 °C. The piranha solution is poured into the manifold and cells; the viscous liquid usually must be assisted in entering the cell by a pipette (and in the miniature cells will not enter at all). After ~ 1 hour, the solution should be emptied, and the manifold and cells rinsed with high purity water (several times), followed by methanol (also several times). After cleaning and rinsing, the cell manifold is baked out in a vacuum oven (Figure A.3) for several hours to remove moisture from the glass; temperatures above 130 °C are sufficient.

The prepared cell manifold is at this stage ready for the Rb ampule (or Rb salt powder mixtures, described below), a sealed glass chamber with Rb metal inside. The manifold has a sidearm for holding the ampoule (on the left in Figure A.2), which is initially open at the top. If the Rb is a natural abundance (and therefore less expensive) mixture, the ampule is broken open in air and dropped into the sidearm, which is then sealed by

Figure A.4: "AtmosBag" used to provide a nitrogen environment for opening a ^{87}Rb metal container and transferring the ampule to the cell manifold. Shown here for a manifold with three miniature cells.

heating the glass with a torch and pulling off the end. The top layer of Rb reacts with air and oxidizes during this step, but this is unimportant if enough Rb ($\sim$ 1 g) is used. If the Rb is isotopically enriched, the ampule can be opened, placed in the manifold, and the manifold closed off with an endcap, all in a nitrogen environment using the AtmosBag (Figure A.4, essentially a low quality glove box). This minimizes oxidation and permits a smaller quantity of Rb to be used in the ampule. It should be noted that sealing off entrances, pulling off cells, and making other adjustments requires a basic knowledge of scientific glassblowing techniques, for which chapter 2 of [116] is a good reference.

The cell manifold with Rb in the sidearm is next attached to a vacuum system. After waiting for the base pressure to reach 10^{-5} torr or lower, the manifold is again baked out while being pumped on, at $\gtrsim$ 175 °C; no longer in an enclosed oven, the manifold is wrapped in aluminum foil and heated with heating tape. This reduces the base pressure

of the system, and removes water that may have accumulated when the system was open to air while placing the Rb ampule in the sidearm. The bottom part of the Rb sidearm where the ampule sits should not be heated, as doing so would pump the Rb away also. The o-rings on the valves must be able to withstand high temperature (they will reach ~ 230 °C during the wall coating stage), and the vacuum grease lubricating them should not outgas at that temperature. (The o-rings were Kalrez AS-568A, and the grease was Dow Corning high vacuum grease, which is rated to 204 °C).

The coating procedure begins by cooling the manifold to room temperature and filling it with N_2 gas to above atmospheric pressure. The central valve on the manifold (see Figure A.2) is removed and the tetracontane can be placed in or near the cell. This can be done in two ways: (1) tetracontane flakes can be melted onto the end of a thin glass rod, which is dropped directly into the cell; (2) flakes can be placed on the end of a pipette, then deposited directly into the manifold, between the central valve and the cell. For miniature cells the second method is required, as a rod will not fit into the 1-mm opening into the cell. After the tetracontane is deposited, the valve is resealed and the manifold evacuated.

To apply tetracontane to the cell walls, we enclose the cell in an oven composed of a thin aluminum box with attached resistive heater plates. The box often covers the cell past the Rb tip, unlike that shown in Figure A.2. The neck of the cell manifold is wrapped in resistive heating tape to provide additional heating of this region. The valve is then closed, isolating the cell from the rest of the vacuum system so that tetracontane does not escape the coating region during the coating process. The cell and neck are then heated to $\sim 200\,^{\circ}$C to melt and vaporize the tetracontane, with the neck region $\gtrsim 10\,^{\circ}$C warmer than the cell to keep tetracontane from accumulating in the neck. Finally, the cell is cooled slowly to room temperature and the valve opened to the vacuum system so that any gas created during the coating process is pumped away. Visible tetracontane on the cell walls indicates cold spots

during the coating process and thus the lack of a uniform coating layer over the surface. In this case, the process is repeated to improve the coating uniformity.

Maintaining a uniform temperature across the cell while cooling down is typically the most difficult step in the procedure. Spots inside the cell that are significantly hotter than the rest will not have paraffin deposited, while cold spots either inside or outside the cell will accumulate most of the paraffin. The tip of the valve stem is especially susceptible to this, as care must be taken to not overheat the valve lest the o-ring grease evaporate. Wrapping the cell tightly in a layer of aluminum foil helps distribute the heat from the surrounding air. Also, running several temperature sensors (near the valve tip, on the neck near the entrance to the aluminum box, and on the cell body) is necessary to monitor the process. Cooling should be performed very slowly, with the neck and valve always remaining hotter than the cell body.

After the coating is successfully applied, metallic Rb is distilled from its ampule to the tip using a blown air heat gun. Bulk Rb is kept out of the main volume of the cell, as it can interact with the coating and damage it. Lastly, the coating rod is moved out of the cell and the cell is "pulled-off" from the manifold by melting the glass just above the Rb tip while also keeping the Rb tip cool. Once the vapor cell has been completed, the temperature of the Rb tip should be kept below that of the cell body so that bulk Rb remains in the tip rather than in the body. Additionally, the cell body should be kept below 81 °C, the melting point of tetracontane.

This final step of Rb distillation is somewhat different if the method of ^{87}Rb extraction from Rb salt is used. Instead of an ampule, a crushed powder mixture of isotopically enriched rubidium chloride (^{87}RbCl) and calcium hydride (CaH) in a $\sim 3:1$ mass ratio is placed in the Rb arm of the manifold. The combined powders are crushed and mixed using a glass mortar and pestle (typically cleaned and baked out in the vacuum oven along

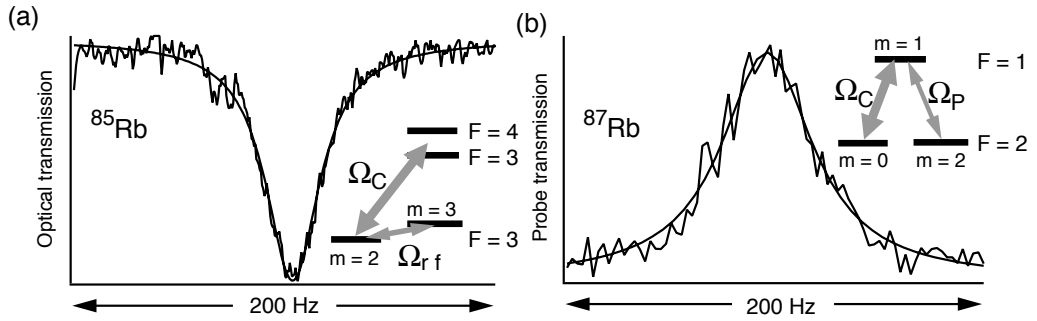

Figure A.5: Ground-state Zeeman coherence measurements using (a) optical pumping double resonance (FWHM $\approx$ 22 Hz) with $\approx$ 0.8 mm beam diameter, and (b) EIT resonance (FWHM $\approx$ 50 Hz) with $\approx$ 2 mm beam diameter. Smooth curves are Lorentzian fits to the data. Intensity $\lesssim$ 0.1 mW/cm^2 to avoid power broadening. *Insets*: interaction schemes for each measurement. Note that for the double resonance measurement we used ^{85}Rb, which has a larger natural abundance (72%) than ^{87}Rb, providing higher Rb density at the same cell temperature.

with the manifold). To ensure sufficient Rb output, at least 150 mg of mixture should be used. Also, any powder mixture that is saved and used later should be re-crushed before placing in the manifold (this is likely necessary because the outer layer of the crushed particles is affected by oxidation and moisture from the air). The distillation process involves the reaction $2RbCl + CaH_2 \rightarrow 2Rb + CaCl_2 + H_2$. The Rb can be distilled into the cell as normal, while the H_2 is pumped away and the inert $CaCl_2$ remains behind. Distillation requires heating the powder section of the manifold to $\sim$ 500 °C, well above the temperature required for the reaction, but necessary to melt rubidium oxides that form a layer over the powder mixture when Rb reacts with air that has not been evacuated from the manifold (some is likely trapped between particles in the powder mixture). The oxides Rb_2O_3 and Rb_4O_6 melt at 489 °C, which likely explains the threshold.

A.2 Coated cell testing

We evaluate wall coating quality by employing two complementary techniques to measure the atomic spin decoherence rate. In optical pumping double resonance [117], we illuminate the cell with circularly polarized light, optically pumping the atomic population to the state with maximum angular momentum $m_F = F$, so that the atomic vapor becomes transparent to the applied optical field. In the presence of a static longitudinal magnetic field which splits the Zeeman ground state sublevels, we apply a transverse rf magnetic field. If the rf field is resonant with the splitting of the ground state Zeeman sublevels, it mixes the population into other levels and thus increases the optical absorption. Sweeping the rf frequency through the Zeeman resonance produces a dip in the transmission spectrum allowing a determination of both the Zeeman frequency and its decoherence rate.

For the example result shown in Figure A.5(a), we detected the change in transmission of a circularly polarized laser field tuned to a transition between the $F = 3$ ground state and unresolved excited states of ^{85}Rb in a static, longitudinal magnetic field of ≈ 38 mG while sweeping the rf field frequency. The observed transmission dip in Fig. A.5(a) had a full width of 22 Hz, corresponding to a Zeeman coherence lifetime ≈ 15 ms.

Alternatively, we measure the EIT linewidth by applying continuous control and probe optical fields with equal frequency and opposite circular polarizations, which optically pump the atoms into a coherent superposition of the ground-state Zeeman sublevels (*i.e.,* the "dark state") [36]. Ideally, atoms in this state are completely decoupled from both optical fields and do not absorb any light. An applied magnetic field lifts the degeneracy of Zeeman sublevels and destroys the dark state, leading to greater optical absorption. For the example results shown in Figure A.5(b) [same Rb cell as in Figure A.5(a)], the control and probe fields were resonant with the $F = 2 \rightarrow F' = 1$ transition of ^{87}Rb, forming a Λ-system on the

$m_F = 0$ and $m_F = +2$ ground-state Zeeman sublevels. The two-photon detuning was varied by slowly sweeping the longitudinal magnetic field near zero. The observed EIT resonance in Figure A.5(b) had a full width ≈ 50 Hz (coherence lifetime ≈ 6.6 ms).

In both double-resonance and EIT measurements, the width of the narrow resonance is limited by the decoherence rate of the Zeeman sublevels. To set a limit on the contribution of wall collisions, we work at low laser and rf field power to avoid power broadening. We also avoid broadening from Rb-Rb spin-exchange collisions by keeping the cell at a low temperature (36 °C, corresponding to a Rb number density of 3×10^{10} cm^{-3}). We believe that uncompensated magnetic field gradients are the leading remaining decoherence source in both DR and EIT linewidth measurements, which is consistent with the approximately factor of two difference in the measured DR and EIT linewidths: for a fixed field gradient, the $\Delta m_F = 2$ EIT transition should have twice the frequency width of the $\Delta m = 1$ double resonance measurement. These results imply that the contribution of wall collisions to the Rb Zeeman decoherence rate is $\ll 10$ Hz.

A.3 List of coated vapor cells

This section lists the paraffin-coated cells designed, constructed, and tested in this laboratory over the past five years. For each, we will describe reasons for design choices, report on the cell's performance, and highlight deviations from the typical coated cell procedure described in Section A.1.

"Standard" coated cell. Coated cell with natural abundance Rb, manufactured in the Summer of 2004. It has length $L = 5.0$ cm and diameter $D = 2.5$ cm. This is the cell used in the preceding section to illustrate coherence lifetime measurements, and is the cell used for most coated cell experiments described in Chapters 5, 6, and 7. Its photograph

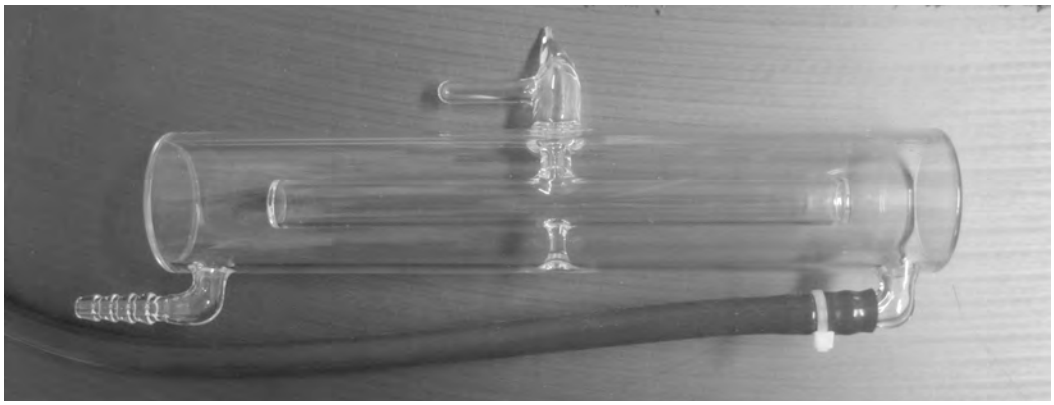

Figure A.6: Double-jacketed, long, narrow coated Rb vapor cell. The surrounding chamber served as an oven for applying the paraffin wall coating, and for operating optics experiments.

appears in Figure 2.8. Techniques did not deviate from the design steps given in Section A.1, and the method of melting paraffin on the end of a thin glass rod was used. A second cell was made during the same run, but its coating quality was not as high, yielding double-resonance linewidths (Section A.2) of ~ 300 Hz as opposed to the 22 Hz of the better cell.

Double-jacketed coated cell. Natural abundance coated cell with a higher aspect ratio: $L = 15$ cm and $D = 1.2$ cm. It was built in the Summer of 2005. This size was chosen to give higher optical depth for a given temperature, and to combat radiation trapping effects. The cell is enclosed inside a larger cylindrical chamber ($L = 21$ cm, $D = 3.8$ cm), as shown in Figure A.6. The chamber itself served as the oven for both the paraffin coating application procedure, and for optics experiments, so the thin aluminum box oven was not used. Heating tape was still used for the rest of the manifold above the cylinder. Blown hot air enters on one side and leaves on the other, and temperature sensors are placed at the input port and near the exhaust port inside the chamber.

The wall coating in this cell "worked" insofar as dual-structured EIT could be seen (see Chapter 5), but it's performance was poor. A T_1 measurement (determined from the

amount of time Rb maintains its optically pumped states) yielded only $100 - 200$ μs, in contrast to the $\sim$ 4.5 ms lifetime measured in the standard coated cell described above. Poor coating uniformity is likely a result of temperature gradients across the length of the cell during the paraffin application process. Other disadvantages of this cell design include the deposition of moisture and other materials on the outside of the cell during normal operation, and the loss of optical signal due to the system having eight surfaces without anti-reflection coating.

Long, narrow coated cell. Natural abundance coated cell built in the Fall of 2005. $L = 10$ cm and $D = 1.2$ cm, and the cell was not built into larger cylindrical chambers. Due to the non-standard length, a different aluminum box (with thicker walls) was built for the coating application procedure. Achieving a uniform temperature across the cell proved difficult, and the coated process was repeated many times. The first attempted cell had its rubidium reacted away due to interaction with vacuum grease that contained fluorine. The cell was broken open at the entrance to the main body of the cell, and attached to a new manifold, followed by multiple cleanings with piranha solution. The second attempt resulted in a coated cell with a $\sim$ 1 kHz double-resonance linewidth, roughly equivalent to 500 Hz in a cell with the more standard 2.5 cm diameter. A high concentration of paraffin on the cell windows led to poor optical transmission; attempts to re-melt the paraffin by submerging the cell in hot water proved unsuccessful.

Short coated cells. Natural abundance coated cells (2) with reduced length ($L =$ 1.0 cm, $D = 1.2$ cm) built in the Fall of 2005. The length reduction prevents the atoms' longitudinal motion from exceeded the ground state hyperfine wavelength of 4.4 cm, potentially allowing hyperfine EIT experiments to be performed in such cells. The cells are shown in Figure A.7. Double-resonance measurements yielded linewidths of 600 Hz (cell on the left) and 1.5 kHz (cell on the right), comparable to that achieved in the long, narrow cell,

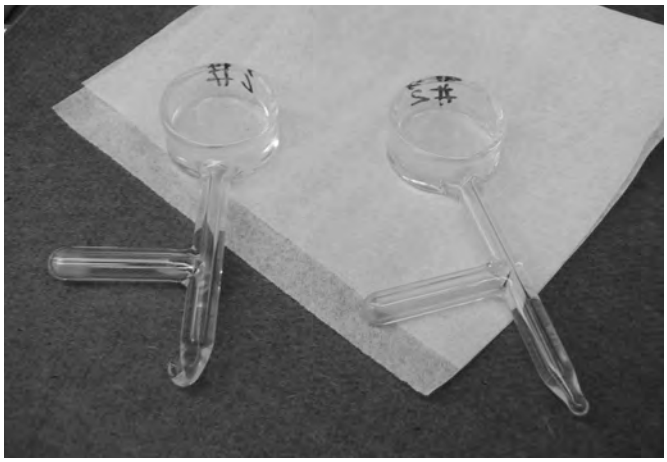

Figure A.7: Short coated Rb vapor cells, used for hyperfine EIT measurements.

but without paraffin on the windows causing transmission loss. The actual ground state decoherence rate due to the coating is probably less, as the laser and rf signals were both power broadened during the measurement (a short, natural abundance cell has very low optical depth, leading to poor SNR). The better of the two cells was used for hyperfine EIT measurements, where the dual-structured shape was clearly observed, but with low contrast of the narrow structure due to low optical depth and two-photon Doppler dephasing. The miniature cells described below proved more successful for hyperfine EIT.

More standard coated cells. Additional natural abundance coated cells (2) of the same size as the "standard" cells listed above were constructed, with a new coating application method (Figure A.8). $L = 5.0$ cm and $D = 2.5$ cm. The cells were submerged in a glass container filled with canola oil, chosen because its "smoke point" is above the vaporization temperature of paraffin (~ 200 °C) and it is easily obtainable. The region of the manifold above the oil's surface and up to the central valve was heated with resistive heating tape. The method was unsuccessful, but using heated liquid to achieve a more uniform paraffin distribution on the cell walls holds promise. In this case, the oil did release some vapor

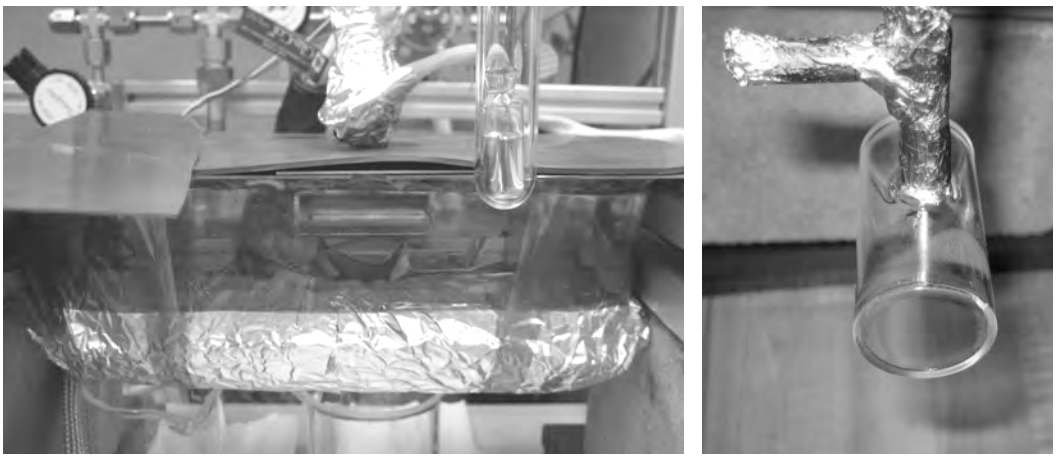

Figure A.8: Setup and results of a new paraffin coating method employing a heated canola oil bath. (Left) The cell is submerged in a container of canola oil, heated from below by resistive heating tape. The manifold above the cell is heated with a resistive heating cord. (Right) Results of a failed coating attempt, where the paraffin deposit can be seen on the top of the cell in the front. This part of the cell was not submerged after the oil expanded, spilled, then contracted when cooled.

(likely due to impurities), and also expanded, when heated. The heating tape soaked up the top portion of the oil, resulting in a loss of oil volume, so when the system was cooled down the cell was no longer submerged, and paraffin was deposited in a cold spot at the top of the cell (Figure A.8). Simple improvements to this method include using a liquid with a smaller expansion coefficient, a heating tape that will not absorb liquid, and an opening for stirring the liquid as it cools.

The now orange-tinged cells were coated in the standard fashion after the canola oil attempt, resulting in long coherence times, with EIT linewidths as narrow as 75 Hz measured.

OTS-coated cells. Two natural abundance cells coated with octadecyltrichlorosilane (OTS) were constructed. The dimensions are the same as the short coated cells described above ($L = 1.0$ cm, $D = 2.5$ cm). The cell coating procedure (described in [118]) is simpler and more consistent than paraffin coating, and the success of the coating process can be

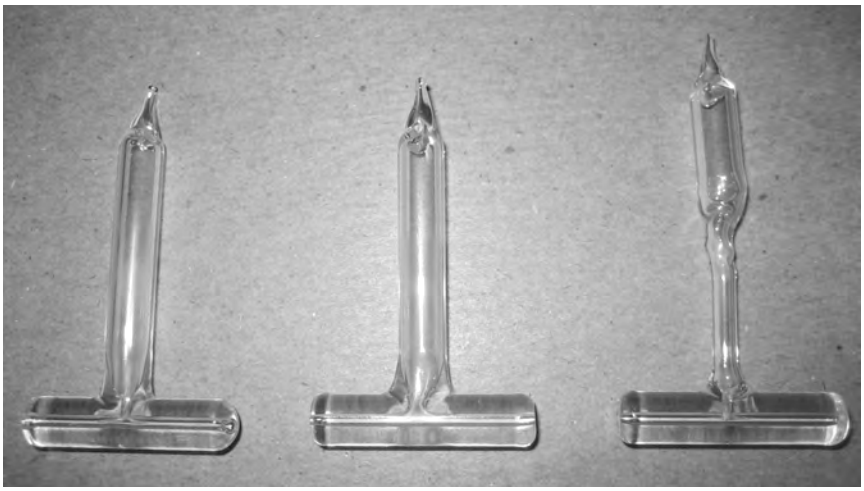

Figure A.9: Miniature paraffin-coated vapor cells with isotopically enriched ^{87}Rb. The same types of cells were used for the EIT, slow, and stored light experiments detailed in Chapter 6.

determined before pulling off the cell. Inspired by the success in [119] of using OTS cells to achieve long lifetimes in potassium cells, we attempted the same with Rb. A reliable OTS coating method, even if it results in a reduced number of coherence-preserving wall collisions compared to paraffin cells, could be very useful for coating high-aspect-ratio cells and other difficult geometries. Coating was successfully applied to both cells, and Rb was distilled into the tips before the cells were pulled off the manifold. Dual-structured EIT was observed, confirming that Rb atoms can collide with the OTS monolayer and maintain spin coherence. However, the contrast was low, and the narrowest linewidths were only ~ 2 kHz in both cells. This indicates only ~ 5 or 6 wall collisions on average before coherence loss, compared to several hundred in our best paraffin-coated cells.

Miniature coated cells. A number of very small coated cells were constructed, with the aim of performing hyperfine-EIT-based experiments and potentially for quantum information applications. They all used isotopically enriched ^{87}Rb (either from metal or from the RbCl with CaH_2 reaction described in Section A.1), and had dimensions $L = 2.5$ cm,

$D = 0.1$ cm. Three such cells are shown together in Figure A.9. The small diameter allowed for the cell to be longer than the $L = 1$ cm short coated cells, since the longitudinal atomic Rb motion will not be a significant fraction of the hyperfine wavelength (4.4 cm) on the time scale of EIT experiments. This, combined with the factor of ~ 3 increase in density for a given temperature gained by using enriched Rb, can lead to a high-contrast narrow EIT structure. Measurements of EIT, slow, and stored light in these cells are described in Chapter 6, where the linewidths and wall coating quality estimates are also given.

Appendix B

Density segregation in vertically-vibrated granular media

This appendix recounts an experiment in soft condensed matter physics, unrelated to the atomic vapor cell experiments performed in the rest of this work. Here we study how granular particles separate by density when vibrated vertically by an external source, and in particular how particle separation and pattern formation depends on the surrounding interstitial gas. This chapter combines work from both the final published version [120] and an earlier version [121].

We report experimental studies of the effect of interstitial gas on mass-density-segregation in a vertically-vibrated mixture of equal-sized bronze and glass spheres. Sufficiently strong vibration in the presence of interstitial gas induces vertical segregation into sharply separated bronze and glass layers. We find that the segregated steady state (*i.e.*, bronze or glass layer on top) is a sensitive function of gas pressure and viscosity, as well as vibration frequency and amplitude. In particular, we identify distinct regimes of behavior that characterize the change from bronze-on-top to glass-on-top steady-state.

Vibrated granular media exhibit characteristics both similar to and distinct from solids, liquids, or gases, with important open questions about the applicability of hydrodynamic theories and the emergence of patterns and order [122, 123, 124, 125, 126, 127]. Past experiments investigated the striking effects of interstitial gas on vibrated granular media [128, 129, 130, 131, 132, 133, 134, 135]. In particular, it was demonstrated [136, 137, 138] that interstitial gas (in contrast to vacuum) is necessary for spatial segregation (vertical layering) by particle *mass density* in a binary granular medium of equal-sized particles that is vertically vibrated in a sealed cell. This result begs the question of mechanism: how is the interstitial gas so profoundly affecting the density-ordering of a vibrated binary granular system; and in particular, what happens when the interstitial gas pressure, viscosity, and pressure gradients are varied? In this chapter we report an experimental study of such density-segregation as a function of interstitial gas pressure and viscosity, as well as vibration frequency and amplitude, which informs a qualitative physical picture of density segregation.

Our experimental setup was similar to that of [136, 137]. The granular mixture consisted of equal-sized solid spheres of bronze (ACU Powder International) and soda lime glass (MO-SCI Corp.) with diameter $d = 98 \pm 8$ μm, where 90% of both types of particles fell within this range. The respective mass densities of the bronze and glass are 8.9 g/cm^3 and 2.5 g/cm^3. We used a volume mixing ratio of glass:bronze = 3:1, except where specifically noted below. To reduce moisture, we heated each mixed granular sample for 3–5 minutes and used an electrically grounded brass pan to reduce static charge buildup. We used such freshly-prepared samples for each data-taking run, which we performed over times $\lesssim 3$ hours.

We placed each sample inside a sealed, rectangular borosilicate glass cell (Spectrocell, Inc.) of width 46 mm, height 50 mm, and depth 10 mm, mounted on a vibration platform (Figure B.1). The height of the granular mixture at rest in the sample cell was approximately 20 mm for all data runs. We used an electromechanical shaker (Labworks,

Inc. ET-126) driven by a sinusoidal waveform to vibrate the cell vertically, with vertical (z) position $z(t) = A\sin(2\pi ft)$ and peak velocity $v = 2\pi Af = A\omega$. We characterized this vibration by the frequency f and dimensionless acceleration $\Gamma \equiv A\omega^2/g$, where g is the acceleration of gravity. We vibrated the cell over the range f = 0–200 Hz and Γ = 0–20. Over this range the particles did not interact with the top of the sample cell. A pair of accelerometers continuously monitored the vibration in three dimensions. We ensured that the dimensionless horizontal accelerations (Γ_x and Γ_y) were small (< 0.2, except as noted below), and limited variation in the dimensionless vertical acceleration (Γ_z) to no more than 0.1 across the width of the platform. A gas-delivery system controlled the interstitial gas type and pressure inside the sample cell (P = 1–1000 torr $\pm$ 3 torr), without affecting the mechanical properties of the cell. We performed experiments with either N_2 or Ne gas, which have respective viscosities η = 17.9 and 32.1 μPa·s at room temperature (here η is independent of gas pressure for $P \gtrsim 25$ torr).

For our range of experimental conditions, the vibrated grains moved relative to the interstitial gas with Reynolds number $Re \approx (\rho dv/\eta) \approx 0.01$–1, where ρ is the gas mass density. Hence viscous drag was usually larger than inertial drag. Importantly, there was no gas flow in and out of the sealed sample cell. Thus vertical gradients in the gas pressure were created across the vibrated particle bed inducing bulk gas flow through the granular medium (with gas flow velocity $v_g \sim \nabla P/\eta \sim P/\eta$ as given by application of Darcy's Law) [128]. To avoid hysteretic effects, we operated with the initial condition of a fully mixed, flat-topped sample, obtained by shaking under vacuum [128, 136, 137]. We then admitted the desired gas; observed visually and with video recording and digital photography (20 μm resolution) the steady-state reached for long-term vibration with constant Γ and f, as well as the behavior exhibited on the approach to the steady-state; removed the gas; and returned the sample to its initial mixed configuration before another run of the experiment.

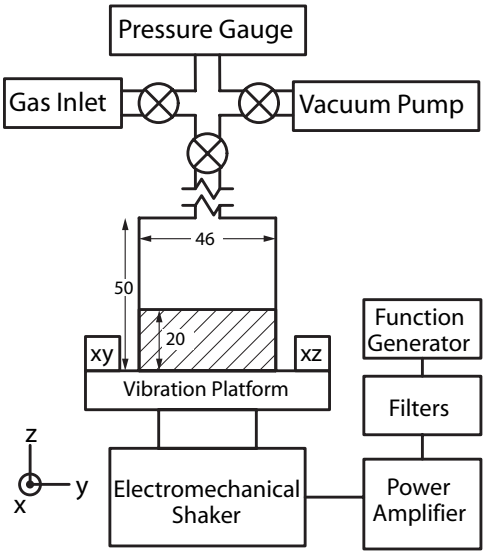

Figure B.1: Schematic of the apparatus, not to scale. Accelerometers are labeled by their sensitive axes (xy and xz). Dimensions are given in mm. The cell depth along the x-axis is 10 mm (not shown).

Using this apparatus, we observed steady-state patterns of vibration-induced density-segregation (see Figure B.2) consistent with the schematic results of Burtally *et al.* [136]. We then studied the dependence of density-segregation on gas properties, and developed a qualitative physical picture in which density-segregation arises from a single underlying mechanism: the relative motion of grains and gas tend to induce a spatial separation of heavy and light grains because gas-drag acceleration is mass-dependent, scaling as $a_{drag} \sim v_g^n/m$ (where v_g is the relative gas/grain velocity, $n = 1$ for viscous drag and $n = 2$ for inertial drag, and m is the grain mass). This mass-dependent acceleration leads to two competing effects: (i) the heavier bronze particles are more mobile than the glass spheres when vertically vibrated in the presence of interstitial gas; and (ii) the lighter glass particles are preferentially dragged in the direction of bulk gas flow relative to the particle bed.

Thus, the "bronze-on-top" steady state is favored by conditions in which the upward grain velocity during the upward stroke of each cycle (the same for both bronze and

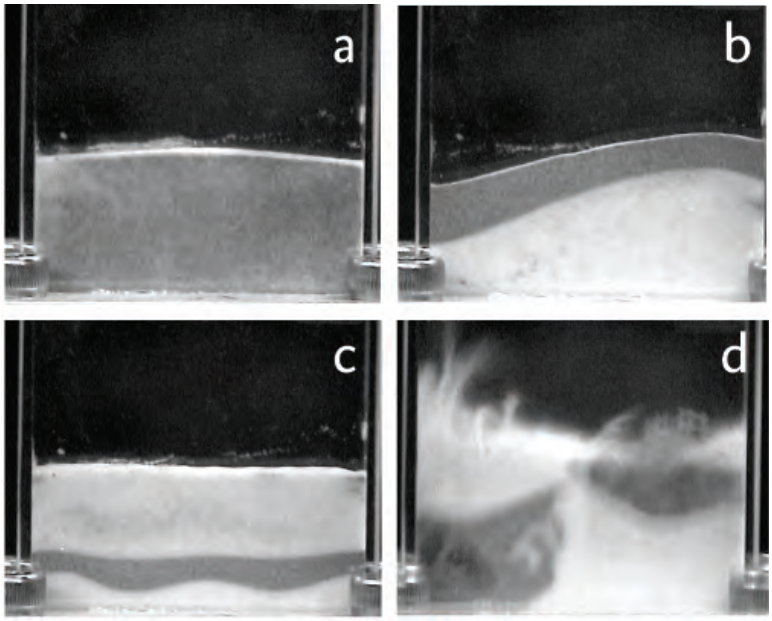

Figure B.2: Examples of steady-state behavior induced by vertical vibration. (a) The mixed state, which occurs under vacuum and was used as the initial condition for most experiments. (b) Bronze-on-top; N_2 interstitial gas at $P = 500$ torr, $\Gamma = 8.7$, $f = 90$ Hz. Digital images show the boundary between the bronze and glass layers to be only one or two grain diameters thick. (c) Glass-on-top; same parameters as (b), except $\Gamma = 10.8$. Often a glass layer also forms below the bronze layer. (d) Unstable pattern formation characteristic of very large Γ; N_2 interstitial gas at $P = 800$ torr, $\Gamma = 14$, $f = 50$ Hz.

glass grains in the dense-bed regime we are studying) is greater than any upward velocity of bulk gas flow within the sample cell (driven by vibration-induced pressure gradients). Alternatively, the "glass-on-top" steady-state is favored when there is a net upward gas flow during the upward stroke of the shaker, with gas flow velocity > upward grain velocity. Notably, we found that the glass-on-top state *never occurred* when upward gas flow due to gas pressure gradients was inhibited by placing the sample in a cell with a gas-permeable bottom (the cell was made of Lexan with a bottom of steel mesh – sealing the bottom restored all segregation phenomena observed with the sealed cell). In contrast, other interactions in the vibrated cell do not distinguish between grain masses in a manner that can induce density-

segregation: g is independent of mass; the shaker gives all grains the same initial upward velocity during each cycle of the vibration; collisions randomize grain motion isotropically (far from the container walls); and the sample size is large enough that force chains across multiple grains are insignificant [139].

In support of this qualitative picture, we determined from visual and video observations that the heavier bronze particles are more mobile than the glass particles in the presence of interstitial gas. For example, we determined that the local expansion (dilation) of the granular bed under vibration is greater for regions with a larger bronze concentration. These dilated, lower-particle-density regions then effectively attract particles, preferentially the more mobile bronze. The cycle continues until full segregation of the bronze and glass particles occurs [136]. From our observations we determined the following scenario for a typical vibration cycle: initially the bed of particles is released upwards as the base reaches its largest velocity $= A\omega = \Gamma g/\omega$; the base then decelerates, reaches its highest z-value, and moves down, leaving a gap with few if any particles (since the base moves faster than the particles fall); gas from above and inside the bed moves to fill the void, creating a downward gas flow, which contributes to dilation of the bed and thus to relatively greater mobility of the bronze particles, and also tends to carry the lighter glass particles down; the base then reaches its lowest z and moves upwards, compressing the gas in the gap; the resulting pressure gradient causes upward gas flow, which also helps dilate the bed and carries glass particles upwards; the base then hits the particles, compressing and releasing the bed, and the cycle continues. As shown in a previous experiment [130], a key asymmetry in the vibration cycle is that the largest gas pressure gradient is generated as the granular bed is compressed against the cell bottom: thus the peak upward gas flow velocity and drag typically exceed that of the downward flow. In experiments using the cell with a gas-permeable bottom (*i.e.*, with minimal gas pressure gradients and upward gas flow), we observed greatly decreased

particle mobility and bed expansion. In particular we found that Γ had to be increased by about a factor of 2 (by increasing the amplitude A) to induce bronze-on-top segregation; and, as noted above, glass-on-top segregation never occurred. Further, as described in [137] all forms of density segregation — including both bronze-on-top and glass-on-top — were suppressed for a cell with a gas-permeable bottom *and* top. These results are consistent with bed expansion and particle mobility being enhanced by bulk gas flow through the sample.

To characterize the competing effects of gas drag — *i.e.*, greater mobility of the heavier bronze particles and preferential dragging of the lighter glass particles with bulk gas flow — we used the sealed sample cell and performed experiments focusing on the typically sharp boundary in vibration-amplitude parameter space between the stable bronze- and glass-on-top states. In particular, we determined the critical value of the dimensionless acceleration (Γ_c) that delineates the change from bronze-on-top to glass-on-top steady states, as a function of gas pressure (P), vibration frequency (up to 200 Hz), and gas viscosity. Figure B.3 shows examples of the measured dependence of Γ_c on P for typical high and low vibration frequencies (90 and 50 Hz) and gases of differing viscosity (Ne and N_2). As discussed below, we observed a dramatic difference in the dependence of segregation behavior on gas viscosity at $f = 50$ Hz, but little difference at $f = 90$ Hz. Specifically, the glass-on-top state does not occur at $f = 50$ Hz for Ne gas at any pressure.

Each value of Γ_c, plotted in Figure B.3, is an average between the highest Γ to yield bronze on top (Γ_{b-hi}) and the lowest Γ to yield glass-on-top (Γ_{g-lo}), as determined by repeated sets of experimental runs. Uncertainty in the determination of Γ_c comes from several sources: irreproducibility of Γ_{b-hi} and Γ_{g-lo}, which contributed an uncertainty $\delta\Gamma_1 \approx 0.1$; spatial variation of Γ_{b-hi} and Γ_{g-lo} across the width of the platform, with associated uncertainty $\delta\Gamma_2 \approx 0.1$; and the systematic offset $\delta\Gamma_3 = \Gamma_{b-hi} - \Gamma_{g-lo}$, which varied from $\approx$ 0–0.5 for differing experimental conditions. The total uncertainty for each plotted value of

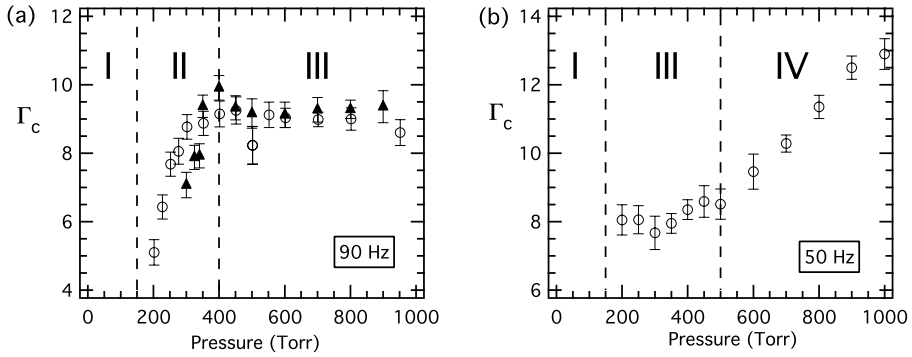

Figure B.3: Measured gas pressure dependence of the critical value of the dimensionless acceleration (Γ_c) delineating the change from the bronze-on-top to glass-on-top steady states. (a) $f = 90$ Hz vibration frequency, comparing N_2 and Ne interstitial gas. (b) $f = 50$ Hz, N_2 gas only; the glass-on-top state does not occur at this frequency for Ne. Four approximate pressure regimes of characteristic Γ_c behavior are indicated: (*I*) glass-on-top segregation does not occur at low gas pressure; (*II*) glass-on-top segregation occurs with the sample approximately flat on top; (*III*) glass-on-top segregation occurs via a pressure-independent spill-over mechanism; (*IV*) glass-on-top segregation occurs via pressure-dependent spill-over with inertial drag nominally comparable to viscous drag.

Γ_c is $\Delta\Gamma_c = (\delta\Gamma_1 + \delta\Gamma_2)^{1/2} + \delta\Gamma_3$.

From the measurements of Γ_c vs. P and associated observations of bed dynamics we identify four characteristic regimes of steady-state behavior, as indicated in Figure B.3 and summarized in the following.

Regime I (no glass-on-top steady state at low gas pressure) — The glass-on-top steady state does not occur at low gas pressure (below about 200 torr for N_2 and 300 torr for Ne), so Γ_c is undefined. In this low pressure regime we observed minimal bed dilation and low mobility of the glass particles, which is consistent with relatively small drag from bulk gas flow driven through the particle bed by vibration-induced pressure gradients (since the gas flow velocity scales as $v_g \sim \nabla P \sim P$). Note that at very low gas pressure ($\lesssim 50$ torr) we found that the bronze-on-top steady-state also does not occur.

Regime II (glass-on-top occurs with minimal sample heaping) — At moderate gas

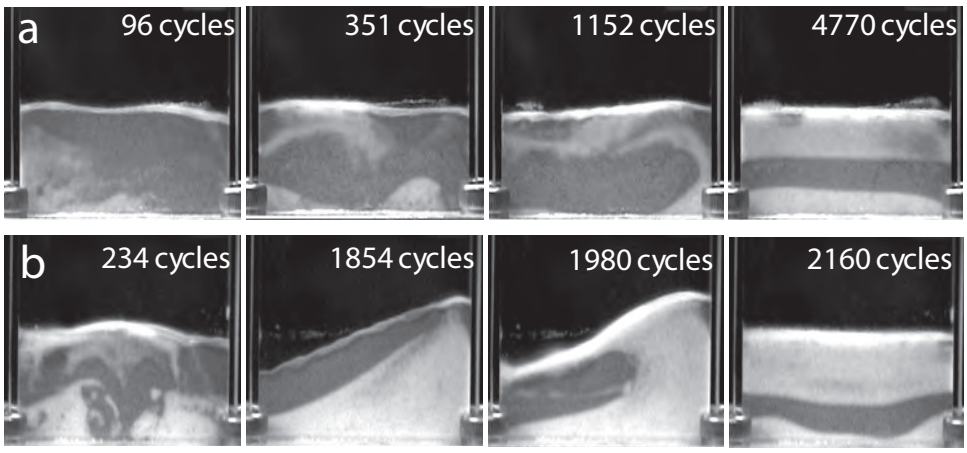

Figure B.4: Time-resolved images illustrating evolution from an initial mixed state [like Figure B.2(a)] toward a glass-on-top steady-state. (a) Regime II: N_2 gas, $P = 250$ torr, $\Gamma = 8.9$, $f = 90$ Hz. (b) Regime III: N_2 gas, $P = 500$ torr, $\Gamma = 10.8$, $f = 90$ Hz.

pressures and high vibration frequencies such as $f = 90$ Hz, both bronze-on-top and glass-on-top steady-states occur with the top of the vibrated particle bed remaining approximately flat; *i.e.*, with minimal heaping, see Figure B.4(a). As P is increased, the observed bed dilation and particle mobility increase, the bronze-on-top steady-state is reached more quickly (for $\Gamma < \Gamma_c$), and Γ_c becomes larger. Similar dynamics, steady states, and values for Γ_c are found for N_2 and Ne interstitial gases. See Figure B.3(a). This observed pressure-dependence and approximate viscosity-independence for Γ_c is consistent with viscous drag due to bulk gas flow through the particle bed playing a dominant role [138], which implies that the drag force on the particles scales as $F_v \sim \eta v_g \sim P$ since application of Darcy's Law gives $v_g \sim \nabla P/\eta \sim P/\eta$ in a sealed sample cell [128]. At lower vibration frequencies such as $f = 50$ Hz, Regime II behavior does not occur, since for the relatively larger vibration and gas flow velocities ($\approx \Gamma g/\omega$) sample heaping already ensues in Regime I, *i.e.*, at gas pressures below that required for glass-on-top segregation.

Regime III (glass-on-top occurs via pressure-independent sample spill-over) — Above

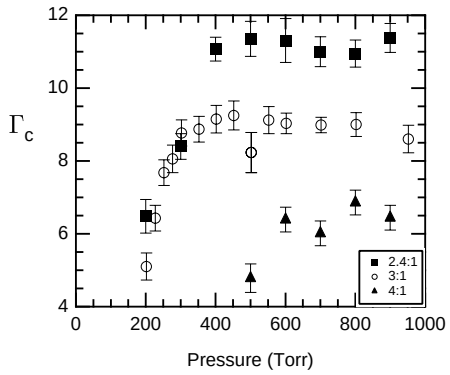

Figure B.5: Measured Γ_c variation with N_2 gas pressure at $f = 90$ Hz, for three glass:bronze mixing ratios, 2.4:1 (squares), 3:1 (circles), and 4:1 (triangles). As the bronze fraction grows, the thickness of the bronze-on-top layer increases, which suppresses the mobility of the underlying glass particles and increases Γ_c.

a gas pressure threshold, the glass-on-top state is reached via a "spill-over" mechanism in the presence of sample heaping, as illustrated in Figure B.4(b). For $\Gamma \geq \Gamma_c$ the sample quickly forms a transient bronze-on-top layer, as heaping occurs across the width of the bed. The heaping builds until the bronze layer surpasses the angle of marginal stability [124]. Particles slide down the heap, with partial replenishment via convective upflow in the bronze layer. Glass particles then break through at the top of the heap and spill over, forming the glass-on-top steady-state. Particle-bed heaping is known to arise from vibration-induced pressure gradients and bulk gas flow, with a steepness that is largely pressure- and viscosity-independent [128]. Correspondingly, our measurements of Γ_c show little dependence on P and η in Regime III at higher vibration frequencies such as $f = 90$ Hz. For lower vibration frequencies, however, we observed that the spill-over mechanism is inhibited relative to the convective replenishment of the bronze layer. In particular, the glass-on-top state cannot be achieved for Ne gas and $f \lesssim 75$ Hz, nor for N_2 gas and $f \lesssim 40$ Hz, which is consistent with the opposite scaling of the viscous drag force with η and f: $F_v \sim \eta v_g \sim \Gamma_c \eta / f$, with Γ_c near the typical value for Regime III.

Regime IV (glass-on-top occurs with pressure-dependent sample spill-over) — At low vibration frequency and high gas pressure the observed difference in bronze and glass mobility grows with pressure, which inhibits the spill-over mechanism to the glass-on-top steady-state and yields an approximately linear dependence of Γ_c on P. See Figure B.3(b). This pressure dependence may result from inertial gas drag on the particles, which according to a simple estimate ($Re \sim P/\eta f \sim 1$) becomes significant in this regime.

Further study will be needed to establish a full, quantitative understanding of the effect of interstitial gas on density-segregation in vertically-vibrated granular media. For example, density-segregation can depend in detail on system parameters such as the particle mixing ratio. In our experiments we found that a bronze-on-top layer greatly suppresses the mobility of the underlying glass particles; and the thicker the bronze layer the greater the suppression of glass mobility. One consequence of this bronze-on-top suppression is demonstrated in Figure B.5: introducing more (less) bronze into the system requires a larger (smaller) Γ_c to bring glass to the top, as the glass-on-top steady-state is generally preceded by a transient bronze-on-top condition. Future work could employ NMR/MRI techniques to map grain motion as well as gas pressure and flow dynamics, by using NMR-detectable grains [140] and hyperpolarized noble gas [99], respectively. NMR investigations of fluidized beds [141] may be extended to studies of segregation phenomena as well [142, 143].

Bibliography

[1] R. W. Boyd and D. J. Gauthier, Prog. Optics **43**, 497 (2002).

[2] L. M. Duan, M. D. Lukin, J. I. Cirac, and P. Zoller, Nature **414**, 413 (2001).

[3] M. D. Lukin, Rev. Mod. Phys. **75**, 457 (2003).

[4] C. H. van der Wal, M. D. Eisaman, A. Andre, R. L. Walsworth, D. F. Phillips, A. S. Zibrov, and M. D. Lukin, Science **301**, 196 (2003).

[5] T. Chaneliere, D. N. Matsukevich, S. D. Jenkins, S. Y. Lan, T. A. B. Kennedy, and A. Kuzmich, Nature **438**, 833 (2005).

[6] K. S. Choi, H. Deng, J. Laurat, and H. J. Kimble, Nature **452**, 67 (2008).

[7] M. D. Eisaman, A. Andre, F. Massou, M. Fleischhauer, A. S. Zibrov, and M. D. Lukin, Nature **438**, 837 (2005).

[8] D. N. Matsukevich, T. Chaneliere, S. D. Jenkins, S. Y. Lan, T. A. B. Kennedy, and A. Kuzmich, Phys. Rev. Lett. **97**, 013601 (2006).

[9] C. W. Chen, J. Laurat, H. Deng, K. S. Choi, H. de Riedmatten, D. Felinto, and H. J. Kimble, Science **316**, 1316 (2007).

[10] Z. S. Yuan, Y. A. Chen, B. Zhao, S. Chen, J. Schmiedmayer, and J. W. Pan, Nature **454**, 1098 (2008).

[11] S. E. Harris, Phys. Today **50**, 36 (1997).

[12] S. E. Harris, J. E. Field, and A. Kasapi, Phys. Rev. A **46**, R29 (1992).

[13] E. Arimondo, Prog. Optics **35**, 257 (1996).

[14] S. E. Harris and L. V. Hau, Phys. Rev. Lett. **82**, 4611 (1999).

[15] M. Fleischhauer, A. Imamoglu, and J. P. Marangos, Rev. Mod. Phys. **77**, 633 (2005).

[16] L. V. Hau, S. E. Harris, Z. Dutton, and C. H. Behroozi, Nature **397**, 594 (1999).

[17] M. M. Kash, V. A. Sautenkov, A. S. Zibrov, L. Hollberg, G. R. Welch, M. D. Lukin, Y. Rostovtsev, E. S. Fry, and M. O. Scully, Phys. Rev. Lett. **82**, 5229 (1999).

[18] D. Budker, D. F. Kimball, S. M. Rochester, and V. V. Yashchuk, Phys. Rev. Lett. **83**, 1767 (1999).

[19] M. Fleischhauer and M. D. Lukin, Phys. Rev. Lett. **84**, 5094 (2000).

[20] M. Fleischhauer and M. D. Lukin, Phys. Rev. A **65**, 022314 (2002).

[21] C. Liu, Z. Dutton, C. H. Behroozi, and L. V. Hau, Nature **409**, 490 (2001).

[22] D. F. Phillips, A. Fleischhauer, A. Mair, R. L. Walsworth, and M. D. Lukin, Phys. Rev. Lett. **86**, 783 (2001).

[23] A. Mair, J. Hager, D. F. Phillips, R. L. Walsworth, and M. D. Lukin, Phys. Rev. A **65**, 031802 (2002).

[24] J. J. Longdell, E. Fraval, M. J. Sellars, and N. B. Manson, Phys. Rev. Lett. **95**, 063601 (2005).

[25] J. Vanier and C. Audoin, *The Quantum Physics of Atomic Frequency Standards* (American Institue of Physics, New York, 1989).

[26] H. G. Robinson and C. E. Johnson, Appl. Phys. Lett. **40**, 771 (1982).

[27] E. B. Alexandrov and V. A. Bonch-Bruevich, Opt. Eng. **31**, 711 (1992).

[28] M. V. Balabas, D. Budker, J. Kitching, P. D. D. Schwindt, and J. E. Stalknaker, J. Opt. Soc. Am. B **23**, 1001 (2006).

[29] R. W. Boyd, D. J. Gauthier, A. L. Gaeta, and A. E. Willner, Phys. Rev. A **71**, 023801 (2005).

[30] A. B. Matsko, D. V. Strekalov, and L. Maleki, Optics Expr. **13**, 2210 (2005).

[31] M. A. Bouchiat and J. Brossel, Phys. Rev. **147**, 41 (1966).

[32] H. G. Robinson, E. S. Ensberg, and H. G. Dehmelt, Bull. Amer. Phys. Soc. **3**, 9 (1958).

[33] H. M. Goldenberg, D. Kleppner, and N. F. Ramsey, Phys. Rev. **123**, 530 (1961).

[34] D. Budker, V. V. Yashchuk, and M. Zoloterev, Phys. Rev. Lett. **81**, 5788 (1998).

[35] M. T. Graf, D. F. Kimball, S. M. Rochester, K. Kerner, C. Wong, D. Budker, E. B. Alexandrov, M. V. Balabas, and V. V. Yashchuk, Phys. Rev. A **72**, 023401 (2005).

[36] M. O. Scully and M. S. Zubairy, *Quantum Optics* (Cambridge University Press, UK, 1997).

[37] A. F. Molisch, B. P. Oehry, W. Schupita, and G. Magerl, J. Phys. B **30**, 1879 (1997).

[38] A. F. Molisch and B. P. Oehry, *Radiation Trapping in Atomic Vapours* (Oxford University Press, USA, 1999).

[39] A. B. Matsko, I. Novikova, M. O. Scully, and G. R. Welch, Phys. Rev. Lett. **87**, 133601 (2001).

[40] A. B. Matsko, I. Novikova, and G. R. Welch, J. Mod. Opt. **49**, 367 (2002).

[41] J. Vanier, M. W. Levine, D. Janssen, and M. Delaney, Phys. Rev. A **67**, 065801 (2003).

[42] A. V. Taichenachev, A. M. Tumaikin, V. I. Yudin, M. Stahler, R. Wynands, J. Kitching, and L. Hollberg, Phys. Rev. A **69**, 024501 (2004).

[43] A. V. Taichenachev, V. I. Yudin, V. L. Velichansky, A. S. Zibrov, and S. A. Zibrov, Phys. Rev. A **73**, 013812 (2006).

[44] C. Mewes and M. Fleischhauer, Phys. Rev. A **66**, 033820 (2002).

[45] M. D. Lukin, M. Fleischhauer, A. S. Zibrov, H. G. Robinson, and V. L. Velichansky, Phys. Rev. Lett. **79**, 2959 (1997).

[46] R. S. Tucker, P. C. Ku, and C. J. Chang-Hasnain, J. Lightwave Tech. **23**, 4046 (2005).

[47] F. Zimmer and M. Fleischhauer, Phys. Rev. Lett. **92**, 253201 (2004).

[48] M. S. Shahriar, G. S. Pati, R. Tripathi, V. Gopal, M. Messall, and K. Salit, Phys. Rev. A **75**, 053807 (2007).

[49] A. Kasapi, G. Y. Yin, M. Jain, and S. E. Harris, Phys. Rev. A **53**, 4547 (1996).

[50] R. M. Camacho, M. V. Pack, and J. C. Howell, Phys. Rev. A **74**, 033801 (2006).

[51] Y. Okawachi, M. A. Foster, J. E. Sharping, and A. L. Gaeta, Optics Expr. **14**, 2317 (2006).

[52] P. C. Ku, C. J. Chang-Hasnain, and S. L. Chuang, J. Phys. D **40**, R93 (2007).

[53] K. Totsuka, N. Kobayashi, and M. Tomita, Phys. Rev. Lett. **98**, 213904 (2007).

[54] Q. Lin and G. P. Agrawal, J. Opt. Soc. Am. B **21**, 1216 (2004).

[55] J. T. Mok, C. M. De Sterke, I. C. M. Littler, and B. J. Eggleton, Nature Phys. **2**, 775 (2006).

[56] V. P. Kalosha, L. Chen, and X. Bao, Phys. Rev. A **75**, 021802 (2007).

[57] P. C. Ku, F. Sedgwick, C. J. Chang-Hasnain, P. Palinginis, T. Li, H. Wang, S. W. Chang, and S. L. Chuang, Opt. Lett. **29**, 2291 (2004).

[58] F. W. King, J. Opt. Soc. Am. B **19**, 2427 (2002).

[59] Y. Xiao, I. Novikova, D. F. Phillips, and R. L. Walsworth, Phys. Rev. Lett. **96**, 043601 (2006).

[60] Y. Xiao, I. Novikova, D. F. Phillips, and R. L. Walsworth, Optics Expr. **16**, 14128 (2008).

[61] M. Hohensee, Ph.D. thesis, 2009.

[62] J. Simon, J. Tanji, J. K. Thompson, and V. Vuletic, Phys. Rev. Lett. **98**, 183601 (2007).

[63] M. Hohensee, *et al.*, to be published.

[64] I. Novikova, M. Klein, D. F. Phillips, and R. L. Walsworth, Proc. SPIE **5735**, 87 (2005).

[65] D. Felinto, C. W. Chou, H. de Riedmatten, S. V. Polyakov, and H. J. Kimble, Phys. Rev. A **72**, 053809 (2005).

[66] J. Laurat, H. de Riedmatten, D. Felinto, C. W. Chou, E. W. Schomburg, and H. J. Kimble, Optics Expr. **14**, 6912 (2006).

[67] J. K. Thompson, J. Simon, H. Loh, and V. Vuletic, Science **313**, 74 (2006).

[68] A. V. Gorshkov, A. Andre, M. Fleischhauer, A. S. Sorenson, and M. D. Lukin, Phys. Rev. Lett. **98**, 123601 (2007).

[69] A. V. Gorshkov, A. Andre, M. D. Lukin, and A. S. Sorenson, Phys. Rev. A **76**, 033805 (2007).

[70] I. Novikova, A. V. Gorshkov, D. F. Phillips, A. S. Sorenson, M. D. Lukin, and R. L. Walsworth, Phys. Rev. Lett. **98**, 243602 (2007).

[71] I. Novikova, A. V. Gorshkov, D. F. Phillips, Y. Xiao, M. Klein, and R. L. Walsworth, Proc. SPIE **6482**, 64820M1 (2007).

[72] G. Nikoghosyan and G. Grigoryan, Phys. Rev. A **72**, 043814 (2005).

[73] M. Vengalattore, R. S. Conroy, and M. G. Prentiss, Phys. Rev. Lett. **92**, 183001 (2004).

[74] M. Klein, Y. Xiao, A. V. Gorshkov, M. Hohensee, C. D. Leung, M. R. Browning, D. F. Phillips, I. Novikova, and R. L. Walsworth, Proc. SPIE **6904**, 69040C (2008).

[75] M. A. Rosenberry, J. P. Reyes, D. Tupa, and T. J. Gay, Phys. Rev. A **75**, (2007).

[76] M. Schiffer, E. Cruse, and W. Lange, Phys. Rev. A **49**, R3178 (1994).

[77] M. Klein, M. Hohensee, Y. Xiao, R. Kalra, D. F. Phillips, and R. L. Walsworth, Phys. Rev. A **79**, 053833 (2009).

[78] H. M. Goldenberg, D. Kleppner, and N. F. Ramsey, Phys. Rev. Lett. **5**, 361 (1960).

[79] R. H. Dicke, Phys. Rev. **93**, 99 (1954).

[80] D. Budker, W. Gawlik, D. F. Kimball, S. M. Rochester, V. V. Yashchuk, and A. Weis, Rev. Mod. Phys. **74**, 1153 (2002).

[81] A. Kuzmich, L. Mandel, and N. P. Bigelow, Phys. Rev. Lett. **85**, 1594 (2000).

[82] B. Julsgaard, A. Kozhekin, and E. S. Polzik, Nature **413**, 400 (2001).

[83] N. F. Ramsey, Phys. Rev. **78**, 695 (1950).

[84] N. F. Ramsey, *Molecular Beams* (Clarendon, Oxford, UK, 1956).

[85] M. Klein, M. Hohensee, A. Nemiroski, Y. Xiao, D. F. Phillips, and R. L. Walsworth (unpublished).

[86] S. I. Kanorsky, A. Weis, and J. Skalla, Appl. Phys. B **60**, S165 (1995).

[87] A. I. Okunevich, Optics and Spectroscopy **97**, 890 (2004).

[88] A. I. Okunevich, J. Opt. Soc. Am. B **22**, 29 (2005).

[89] M. Klein, I. Novikova, D. F. Phillips, and R. L. Walsworth, J. Mod. Opt. **53**, 2583 (2006).

[90] Y. Xiao, M. Klein, M. Hohensee, L. Jiang, D. F. Phillips, M. D. Lukin, and R. L. Walsworth, Phys. Rev. Lett. **101**, 043601 (2008).

[91] W. E. Bell, A. L. Bloom, and J. Lynch, Rev. Sci. Instrum. **32**, 688 (1961).

[92] D. Budker, L. Hollberg, D. F. Kimball, J. Kitching, S. Pustelny, and V. V. Yashchuk, Phys. Rev. A **71**, 012903 (2005).

[93] M. Crescimanno and M. A. Hohensee, J. Opt. Soc. Am. B (2008).

[94] M. Jain, H. Xia, G. Y. Yin, A. J. Merriam, and S. E. Harris, Phys. Rev. Lett. **77**, 4326 (1996).

[95] L. A. Liew, S. Knappe, J. Moreland, H. Robinson, L. Hollberg, and J. Kitching, Appl. Phys. Lett. **84**, 2694 (2004).

[96] S. Knappe, V. Shah, P. D. D. Schwindt, L. Hollberg, J. Kitching, L. A. Liew, and J. Moreland, Appl. Phys. Lett. **85**, 1460 (2004).

[97] A. B. Matsko, O. Kocharovskaya, Y. Rostovtsev, G. R. Welch, A. S. Zibrov, and M. O. Scully, Adv. At. Mol. Opt. Phys. **46**, 191 (2001).

[98] N. S. Ginsberg, S. R. Garner, and L. V. Hau, Nature **445**, 623 (2007).

[99] R. Wang, M. S. Rosen, D. Candela, R. W. Mair, and R. L. Walsworth, Magn. Reson. Imaging **23**, 203 (2005).

[100] A. S. Zibrov, A. B. Matsko, O. Kocharovskaya, Y. V. Rostovtsev, G. R. Welch, and M. O. Scully, Phys. Rev. Lett. **88**, 103601 (2002).

[101] C. Schnurr, K. D. Stokes, G. R. Welch, and J. E. Thomas, Opt. Lett. **15**, 1097 (1990).

[102] T. Wang, M. Kostrun, and S. F. Yelin, Phys. Rev. A **70**, 053822 (2004).

[103] A. Raczynski, J. Zaremba, and S. Zielinska-Kaniasty, Phys. Rev. A **75**, 013810 (2007).

[104] H. G. Robinson and C. E. Johnson, IEEE Trans. Instr. Meas. **32**, 198 (1983).

[105] R. P. Frueholz, C. H. Volk, and J. C. Camparo, J. Appl. Phys. **54**, 5613 (1983).

[106] C. Schori, B. Julsgaard, J. L. Sorenson, and E. S. Polzik, Phys. Rev. Lett. **89**, 057903 (2002).

[107] B. Julsgaard, J. Sherson, J. I. Cirac, J. Flurasek, and E. S. Polzik, Nature **432**, 482 (2004).

[108] R. P. Frueholz and C. H. Volk, J. Phys. B **18**, 4055 (1985).

[109] O. A. Collins, S. D. Jenkins, A. Kuzmich, and T. A. B. Kennedy, Phys. Rev. Lett. **98**, 060502 (2007).

[110] G. J. Pryde and A. G. White, Phys. Rev. A **68**, 052315 (2003).

[111] E. Knill, R. Laflamme, and G. J. Millburn, Nature **409**, 46 (2001).

[112] I. Novikova, D. F. Phillips, and R. L. Walsworth, Phys. Rev. Lett. **99**, 173604 (2007).

[113] S. Ghosh, J. E. Sharping, D. G. Ouzounov, and A. L. Gaeta, Phys. Rev. Lett. **94**, 093902 (2005).

[114] G. Singh, P. Dilavore, and C. O. Alley, Rev. Sci. Instrum. **43**, 1388 (1972).

[115] D. F. Phillips, A. Boca, and R. L. Walsworth, Evaporative coating of Rb maser cells, 1999, (unpublished).

[116] J. H. Moore, C. C. Davis, and M. A. Coplan, *Building Scientific Apparatus* (Westview Press, Boulder, CO, 2003).

[117] W. Demtroder, *Laser Spectroscopy* (Springer, Berlin, 1996).

[118] M. S. Rosen, T. E. Chupp, K. P. Coulter, R. C. Welsh, and S. D. Swanson, Rev. Sci. Instrum. **70**, 1546 (1999).

[119] S. J. Seltzer, P. J. Meares, and M. V. Romalis, Phys. Rev. A **75**, 051407(R) (2007).

[120] M. Klein, L. L. Tsai, M. S. Rosen, T. Pavlin, D. Candela, and R. L. Walsworth, Phys. Rev. E **74**, 010301(R) (2006).

[121] M. Klein, L. L. Tsai, M. S. Rosen, T. Pavlin, D. Candela, and R. L. Walsworth, 2005, arXiv:cond-mat/0506085v1.

[122] H. M. Jaeger, S. R. Nagel, and R. P. Behringer, Rev. Mod. Phys. **68**, (1996).

[123] J. Duran, *Sands, Powders, and Grains* (Springer-Verlag, New York, 2000).

[124] G. H. Ristow, *Pattern Formation in Granular Materials* (Springer-Verlag, New York, 2000).

[125] S. G. K. Tennakoon and R. P. Behringer, Phys. Rev. Lett. **81**, 794 (1998).

[126] D. Brone and F. J. Muzzio, Phys. Rev. E **56**, 1059 (1997).

[127] P. M. Reis and T. Mullin, Phys. Rev. Lett. **89**, 244301 (2002).

[128] H. K. Pak, E. Van Doorn, and R. P. Behringer, Phys. Rev. Lett. **74**, 4643 (1995).

[129] M. E. Mobius, B. E. Lauderdale, S. R. Nagel, and H. M. Jaeger, Nature **414**, 270 (2001).

[130] X. Yan, Q. Shi, M. Hou, K. Lu, and C. K. Chan, Phys. Rev. Lett. **91**, 014302 (2003).

[131] M. A. Naylor, M. R. Swift, and P. J. King, Phys. Rev. E **68**, (2003).

[132] M. E. Mobius, S. R. Nagel, and H. M. Jaeger, Mater. Res. Soc. Symp. Proc. **759**, 115 (2003).

[133] M. Rhodes, S. Takeuchi, K. Liffman, and K. Muniandy, Granul. Matter **5**, 107 (2003).

[134] M. E. Mobius, X. Cheng, G. S. Karczmar, S. R. Nagel, and H. M. Jaeger, Phys. Rev. Lett. **93**, 198001 (2004).

[135] M. E. Mobius, X. Cheng, P. Eshuis, G. S. Karczmar, S. R. Nagel, and H. M. Jaeger, Phys. Rev. E **72**, 011304 (2005).

[136] N. Burtally, P. J. King, and M. R. Swift, Science **295**, (2002).

[137] N. Burtally, P. J. King, M. R. Swift, and M. Leaper, Granul. Matter **5**, 57 (2003).

[138] P. Biswas, P. Sanchez, M. R. Swift, and P. J. King, Phys. Rev. E **68**, 050301(R) (2003).

[139] Y. Nahmad-Molinari, G. Canul-Chay, and J. C. Ruiz-Suarez, Phys. Rev. E **68**, (2003).

[140] X. Yang, C. Huan, D. Candela, R. W. Mair, and R. L. Walsworth, Phys. Rev. Lett. **88**, 044301 (2002).

[141] T. Pavlin, R. Wang, R. McGorty, M. S. Rosen, D. G. Cory, D. Candela, R. W. Mair, and R. L. Walsworth, Appl. Magn. Reson. **32**, 93 (2007).

[142] M. A. Howley and B. J. Glasser, Chem. Eng. Sci. **57**, 4209 (2002).

[143] M. C. Leaper, A. J. Smith, M. R. Swift, P. J. King, H. E. Webster, N. J. Miles, and S. W. Kingman, Granul. Matter **7**, 57 (2005).